NANOSCALE SURFACE ENGINEERING FOR BIOIMAGING AND DRUG DELIVERY APPLICATIONS

By

Ashwath Jayagopal

Dissertation

Submitted to the Faculty of the

Graduate School of Vanderbilt University

in partial fulfillment of the requirements

for the degree of

DOCTOR OF PHILOSOPHY

in

Biomedical Engineering

May, 2008

Nashville, Tennessee

Approved:

Professor Frederick R. Haselton

Professor V. Prasad Shastri

Professor Susan Kasper

Professor David W. Piston

Professor John S. Penn

Professor Mark D. Does

To K. Appurao and N. Mahalingam

ACKNOWLEDGEMENTS

This dissertation would not have been completed were it not for the support of many people. My dissertation committee was instrumental in helping me formulate solid hypotheses and experimental designs, as well as providing sound advice on personal and professional life. To Professors Haselton, Shastri, Kasper, Piston, Penn, and Does, I thank you for the countless helpful discussions and support throughout my graduate career. Dr. Haselton, thanks for giving me the opportunity to work in your lab, and pester the living heck out of you from time to time, and sifting through all the projects in hope of somehow having a far-reaching impact on the human quality of life. We did a good job!

The biomedical engineering department at Vanderbilt is full of great people. The Haselton and Giorgio labs in particular made my graduate experience as enjoyable as humanly possible. I am grateful to have had such great friends and colleagues throughout the department.

My friends in Nashville played a great role in helping me stay afloat over all these years. Thanks for being there for me. My family is the main reason I have achieved anything in my life. It is their encouragement and caring spirit that sustained me and continue to sustain me as I pursue my goals. I hope I will be as great a source of inspiration to my children as my parents have been to me.

Funding is critical to scientific achievement. I thank Professor Jeff Schall for supporting me on the Vanderbilt Vision Research Center training grant, the Vanderbilt University Discovery Grant program, and the National Institutes of Health.

TABLE OF CONTENTS

Page

Chapter

LIST OF TABLES

Table Page

CHAPTER III

CHAPTER V

CHAPTER VI

LIST OF FIGURES

Figure Page

CHAPTER II

CHAPTER III

CHAPTER IV

CHAPTER V

CHAPTER VI

CHAPTER I

INTRODUCTION

The utilization of nanoscale tools in the development of clinically-relevant diagnostic assays and therapies, and the elucidation of complex biological mechanisms and mediators, will be facilitated by the development of surface engineering strategies which modulate cell and/or biomolecule-specific device targeting. Nanoengineering of device interfaces permits the presentation of information at biologically-relevant length scales, and thus affords unprecedented control over various biomolecular interactions, such as ligand-receptor binding, opsonization, and cell-device contact. Surface engineering strategies may also be applied to create nanodevices of enhanced functionality, via the construction of vehicles which permit the simultaneous packaging of multiple synthetic and biological materials with diverse physicochemical properties.

This dissertation describes three diverse surface engineering strategies which are designed to expand the scope of application of nanotechnology in the imaging of cells and biomolecules *in vitro* and *in vivo*. Targeting and multimodality are the two challenges in nanoscale surface engineering addressed. Nanoscale surface modification technology was utilized to confer cell surface and intracellular substructure targeting capabilities upon nanostructures, and to facilitate multimodal nanotherapeutic and nanodiagnostic approaches. These approaches were systematically evaluated in well-characterized *in vitro* and *in vivo* models.

The first Aim of this proposal was focused on the surface functionalization of quantum dot nanocrystals to enable multiplexed cellular and biomolecular detection *in vivo* with enhanced specificity. In addition, cell subsets were internally-loaded with nanoparticulate imaging agents *via* a cell-penetrating peptide for the long-term tracking of cells in a mouse model of atherosclerosis *ex vivo* and *in vivo*. In Aim 2, nanoscale various imaging agents and/or therapeutics were packaged together within a lipid matrix (solid lipid nanoparticles) to demonstrate the application of a novel multimodal nanocarrier for bioimaging and drug delivery applications. Additionally, paracellular and subcellular translocation mechanisms of these solid lipid nanoparticles were investigated.

Specific Aim 1: Develop surface engineering strategies for cell surface marker detection *in vivo*

In this Aim, nanoparticle surfaces were engineered for the simultaneous color-coded detection of multiple cell surface biomarkers within the same imaging specimen *in vivo* using fluorescence imaging. Previous approaches to detect pathologically-significant biomarkers *in vivo* have been impeded by rapid probe clearance, low signal to noise ratios, and an inability to simultaneously analyze multiple cell types and/or biomarkers within the same imaging session. In this Aim, quantum dots (QD) were coated with engineered monoclonal Mab (Mab) and cell-penetrating peptide (CPP) coatings for the long-term multispectral imaging of cells and biomolecules *ex vivo* and *in vivo* with high targeting efficiency. Mab conjugation was achieved by the use of a high molecular weight polyethylene glycol (PEG) bridge to evade physiological nanoparticulate clearance mechanisms. Furthermore, through biological and chemical modifications of the targeting Mab, specifically Fc-masking and PEGylation, Fc-mediated probe clearance was reduced while maintaining high target specificity. As a test bed for this application, cells and biomolecules involved in inflammation were targeted, and QD were used for spectrally-coding cell adhesion molecules (CAMs) and circulating neutrophils. Imaging of inflammation is a technically-demanding task since nanoparticulate clearance mechanisms are pervasive and high-specificity imaging with low background is critical. The specificity of QD-Mab was evaluated on isolated rat neutrophils and rat retinal endothelial cell cultures *in vitro* using fluorescence microscopy and flow cytometry. The efficacy of this approach was evaluated in rat models of diabetes and ocular inflammation, using an *in vivo* fluorescence imaging system to detect multiple cell types and biomarkers with spectrally-distinct quantum dot fluorescence signatures, followed by *ex vivo* immunofluorescence correlation of *in vivo* observations.

Following this application, quantum dot surfaces were then functionalized with a cell-penetrating peptide coating to enable its loading into cells *ex vivo*. Loading cells with QD as opposed to labeling cell surface proteins may be preferable, as it potentially may enable long-term imaging of cells *in vivo* without membrane shedding of bioconjugates or perturbation of cell surface interactions. This approach was utilized to investigate leukocyte subtype recruitment within lesions of the ApoE -/- atherosclerotic mouse model.

Specific Aim 2: Develop entrapment-based surface engineering strategy to facilitate multimodal nanoparticulate applications

Aim 2 was focused on the collective packaging of multiple synthetic and biological materials for the purpose of conferring multimodal functionality upon nanoscale carriers while concurrently conferring cell targeting capabilities. Multifunctional nanostructures have been sought after for designing combinative therapies, drugs with signal-emitting reporters, as well as cellular and biomolecular detection assays which exploit multiple imaging modalities. In this Aim, a unique nanostructure referred to as functionalized multimodal solid lipid nanoparticles (SLN) was investigated for cell transport capabilities and efficacy as a multimodal carrier for bioimaging and drug delivery applications. SLN consist of a biocompatible solid lipid matrix which during the nanoparticle synthesis process entraps materials of varying physicochemical properties, while bearing a variety of surface information on the SLN periphery. This Aim was centered upon on the synthesis and characterization of SLN containing dyes, proteins, drugs, and the nanoparticulates iron oxide, gold, and QD. Cell transport studies were conducted to determine if SLN have cell membrane translocation properties.

CHAPTER II

BACKGROUND AND SIGNIFICANCE

Potentials and Challenges of Nanoparticles for Medicine and Biology

The overall utility of nanotechnology in the detailed evaluation of biological mechanisms, as well the development of diagnostic and therapeutic tools in medicine, has yielded much enthusiasm. In particular, the emergence of a variety of nanoparticles, often defined as objects with feature sizes below 100 nm, as well as techniques to modulate their surface properties, have enabled a number of applications in these fields. Successful applications of nanoscale surface engineering of nanoparticles in therapeutic development include liposomal and poly-lactide-co-glycolide (PLGA) formulations for targeted drug delivery and sustained drug release strategies (1-4), and the nanoscale surface modification of proteins for prolonged activity *in vivo* (5). Superparamagnetic nanoparticles with biological coatings, such as dextrans, are already in clinical use as magnetic resonance contrast agents for the detection of a number of pathologies (6), and quantum dot nanocrystals have been utilized for a variety of studies in elucidating disease processes *in vivo* and *in vitro*, including cancer biology and cell signaling (7-10). Nanoparticle surfaces have been conjugated to receptor-specific ligands for the targeting of disease-specific cells, and with antibodies to detect proteins of interest, with the physicochemical properties of the nanoparticle permitting the monitoring of biology or disease using a number of analysis tools in medical imaging and molecular characterization. Collectively these applications are very promising and are primarily a consequence of decades of nanoscale surface engineering research and development. Further applications which extend the scope of such technologies are highly-desired and would yield valuable data concerning the pathogenesis, diagnosis, and/or treatment of disease, but will require additional nanoscale engineering advances over current techniques in order to be realized.

Nanoscale Surface Modifications for Enhanced Cellular and Biomolecular Targeting: Proposed Work and Significance

Three high-impact design challenges were addressed in this dissertation: high-efficiency *in vivo* cell surface nanoparticulate targeting, intracellular delivery of nanoparticles, and strategies for the packaging of multifunctional nanoparticles. In order to enhance the targeting specificity of nanoparticles to cell surface proteins, polymer and Mab biochemical modification techniques were employed to mask the nanoparticle from the immune system for long-term imaging, and to retain the antigen-binding affinity of the probe following ligand bioconjugation steps. The objective of these strategies was to minimize nonspecific binding of the nanoparticle during the *in vivo* detection of molecular targets, so as to permit the real-time, simultaneous imaging of multiple biomarkers within the same imaging specimen, with low background or false-positive results. The second challenge involved the translocation of nanoparticles across cell membranes. By surface conjugation of the nanoparticle to cell penetrating peptides, the capability of loading nanoparticles within the cytoplasm was the objective. This enabled tracking of cells *in vivo* or *ex vivo* without perturbing cell surface protein interactions required for cell function, and also enhanced long-term imaging applications, since QD-mAb conjugates could get dislodged from the cell surface due to routine cell surface protein shedding. To address the third challenge, a general process was designed employing biocompatible functionalized solid lipids for constructing multifunctional nanoparticles containing diagnostic and therapeutic reagents for the delivery of drugs and bioimaging using diverse modalities (e.g. electron microscopy, fluorescence imaging, x-ray). The general aim of this strategy was to provide a targeted nanoparticle for usage in medicine and biology which permits extensive use of instrumentation while simultaneously permitting registration of the same biological target between each modality, while also potentially functioning as a biocompatible drug delivery device.

Three diverse schemes were proposed to address each nanoparticle surface engineering design problem, with the understanding that they could potentially be utilized not as individual approaches but in combination, and not explicitly using the prototype nanoparticles used for testing, but rather various classes and combinations of nanoparticles.

Background and Significance: Aim 1- Develop surface engineering strategies for cell surface marker detection *in vivo*: Quantum Dot-Based, Multiplexed *In Vivo* Studies of Vascular Biomarker Expression and Leukocyte Trafficking in Inflammation

Rationale

It has become increasingly important in biology and medicine to consider the relative contribution of multiple cellular and molecular mediators to critical processes, such as angiogenesis and cancer progression, as opposed to traditional studies which focused primarily on analyzing such mediators in singlet, or in a vacuum. In order to simultaneously-monitor multiple participants in disease and other biological processes, molecular probes with near-absolute specificity, high signal to background ratios, and highly-distinct emission spectra (i.e. between molecular probes) must be developed. Quantum dot nanocrystals (QD) offer these potential features; their high fluorescence emission intensities, size-tunable emission spectra, and amenability to surface bioconjugation of ligands provide a means for simultaneously monitoring the expression of multiple biomarkers and/or cell subtypes via optical imaging. However, in order to harness these superior optical properties, QD, as with other nanoparticles, must be carefully nanoengineered for maximum targeting efficiency. The study of mediators of inflammation is an appropriate application for optimizing QD surface engineering strategies, as the cell types being targeted (e.g. macrophages, endothelial cells) are often problematic sites for nonspecific probe uptake. In Aim 1 nanoparticulate masking strategies will be utilized which maximize target binding efficiency while reducing nonspecific clearance of the probe.

Rationale for Multiplexed Imaging of Cellular and Biomolecular Mediators of Inflammation

Undesirable provocation of the inflammatory response is a detrimental feature of numerous diseases such as diabetes, multiple sclerosis, atherosclerosis, and asthma (11-13) and thus impacts a significant population. Inflammation is a complex process involving numerous cell types and surface proteins characterized by leukocyte rolling and tethering along endothelial cells followed by transmigration into tissue. Treatment of inflammation-associated diseases can be challenging due to the fact that the extent and type of inflammation in each case can vary considerably. For example, the leukocyte subsets present, the molecular mediators participating in adhesion and emigration, and the resulting effects on tissue all vary with the type of inflammation. Conventional therapies administered as anti-inflammatory measures such as non-steroidal anti-inflammatory drugs (NSAIDs) and corticosteroids have mixed results in the clinic and are often characterized by significant side-effects. In light of the limitations of these generalized approaches, specifically-targeted therapeutic measures in development intend to inhibit key molecules to prevent transendothelial migration of leukocytes. While not all specifically-targeted therapies have had equal success, those directed towards well-studied molecules, such as Remicade (infliximab) which targets tissue necrosis factor (TNF) in Crohn's disease and rheumatoid arthritis, have shown promising clinical efficacy in patients responding poorly to conventional regimens (10, 14). It can be inferred that the success of clinical diagnostic procedures and therapeutic strategies which employ this molecular level approach is contingent upon a detailed understanding of the mechanisms and mediators involved in specific inflammatory processes.

Current in vitro and ex vivo cellular and molecular profiling tools

Decades of research in the pathogenesis of inflammatory disease have identified leukocyte subsets and their general functions, cell adhesion molecules (CAMs), and other protein families critical in the inflammatory cascade. Biological assays used to elucidate cellular and molecular function in inflammation include blotting techniques, which detect proteins, RNA, or DNA presence within a biological sample, and flow cytometry, a quantitative technique utilized to probe molecular expression, cell cycle phase and viability of cells. Immunohistochemistry can be utilized to visualize a protein of interest in tissue sections. Valuable information about the expression profiles and roles of proteins in inflammation have been extracted from experiments which use these assays. However, for many of these observations, *in vivo* corroboration has not been obtained.

A second limitation of these approaches is that they provide endpoint data only. It is often necessary to culture cells, fix them and analyze each cell sample at a number of different time points. However, real-time spatial and temporal information concerning these proteins is very difficult to obtain. This data could be potentially valuable in determining if the co-expression of one protein next to another enhances its activity, or how the pattern of molecular expression cycles through the progression of a disease or in response to drug interventions. In addition, such assays often involve complex isolation procedures. Some cell cultures are sensitive or very difficult to maintain *in vitro*, which adds difficulty in analyzing a biomarker over a time course of days or weeks. Standard flow cytometry is a powerful quantitative tool, and while it can be used to provide valuable information, such as an estimate of the number of particular receptors on a single cell, this analysis is performed using cells separated from the circulatory environment. Thus, *in vitro* techniques may provide a means of generating hypotheses for *in vivo* function, but it is necessary that some *in vivo* technique be performed to validate the *in vitro* findings.

Current in vivo cellular and molecular imaging tools

The current understanding of the principal molecular and cellular players involved in inflammation is summarized in **Figure 1.** Given the above limitations with *in vitro* assays, several attempts to probe *in vivo* cellular and molecular activities in inflammation have been reported. Radiolabeled monoclonal antibodies to ICAM-1 and VCAM-1 were administered *in vivo* (16, 17). While this represents an important step in multiplexed analysis of inflammatory markers, in order to assess Mab binding at the different timepoints, corrections due to background signal needed to be performed to estimate specific antigenic signal. In addition to the signal to noise issues, these studies required compensations in signal calculations in order to distinguish each signal and minimize contributions from unbound Mab. The spatial and temporal resolution of these radiolabeled Mab techniques are too limited for detailed studies of leukocyte-endothelial dynamics in inflammation.

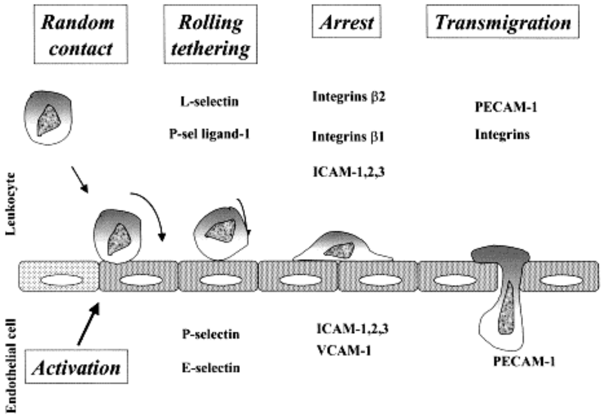

Figure 1. Major inflammatory biomarkers and their functions (15).

A technique with the spatial and temporal resolution to capture leukocyte motility through the circulation was established by Nishiwaki and colleagues using the fluorescent DNA-intercalating dye acridine orange (AO) in conjunction with scanning laser ophthalmoscopy (SLO) (18). While spatial and temporal resolution is adequate, AO is internalized by all nucleated cells in the circulation. Thus, endothelial cells and all leukocyte subsets fluoresce with AO signal, presenting a challenge in determining cell adhesions, and making it impossible to probe molecular expression. Furthermore, AO is phototoxic to lysosomes and a suspected carcinogen (19), has a low quantum efficiency, and is prone to fading and cell washout. Thus, this technique is not appropriate for *in vivo* imaging applications where multiple species are to be detected or for long periods of time. Nevertheless, it is the most common method of observing labeled leukocytes in the circulation for determination of extravasation and velocity.

A third method has been used to characterize VCAM-1 expression *in vivo* using multimodal fluorescent Cy5.5-conjugated Mab and peptide conjugates by Weissleder and colleagues (20, 21). Both conjugates, most notably the peptide conjugates, exhibited a high affinity for VCAM-1 in both intravital confocal microscopy and magnetic resonance studies on atherosclerotic lesions and in TNF-α induced inflamed murine ear. While this method is a significant achievement in the development of *in vivo* molecular profiling techniques, its utility in multispecies real-time imaging applications may be limited. First, one of the applications was hampered by nonspecific IgG control Mab uptake at certain time periods in inflamed murine ear, thus calling into question the specificity of the Mab-based technique. While the peptide-Cy5.5 conjugate was specifically taken up by the cells, performing the same technique for detection of other biomarkers would require time-consuming phage display rounds which may not yield suitable, specific candidates. In addition, while the use of a magnetic resonance contrast-enhancing probe in detecting VCAM-1 may be a useful tool for whole-body detection applications, its potential in applications requiring the detection of multiple proteins is limited to available contrast agents. Also, the use of cross-linked iron oxide nanoparticles (CLIO) has been associated with aggregation problems (22), which could limit their *in vivo* utility, as nonspecific signal may be detected by aggregation of nearby conjugates. The dye Cy5.5 was used to detect VCAM-1 using fluorescence imaging which opens the possibility of this technique for monitoring multiple proteins. However, as in the radiolabeled Mab technique, different conjugates would be required to detect other proteins, which would necessitate an additional excitation laser for each fluorophore. In addition, organic dyes can often have spectrally-overlapping characteristics making specific detection without noise a challenge.

A QD-based in vivo imaging technique for the simultaneous detection of cellular and molecular inflammatory mediators

The proposed design differs from previous *in vivo* approaches to study inflammation primarily by the harnessing of unique QD optical properties, as well as novel surface engineering strategies which are aimed toward enhancing QD targeting efficiency. QD-Mab conjugates are used to specifically label molecular targets *in vivo*. QDs, or semiconducting nanocrystals, with their nanoscale size providing a quantum confinement effect, are the only tracers which can make a multi-spectral imaging system achievable. These properties include higher quantum efficiency relative to conventional dyes, resistance to fading, narrow and size-tunable emission spectra excitable by only one wavelength, and amenability to surface engineering of proteins and polymers for optimum stability and targeting (23). No conventional fluorescent probes currently implemented in *in vivo* imaging techniques are capable of exhibiting all of these features.

Current techniques used to observe detailed cellular and molecular interactions in inflammation are not suitable for imaging multiple cell types, concurrently with multiple proteins, continuously in real-time with sufficient spatial and temporal resolution. A QD-based *in vivo* retinal fluorescence imaging technique has been designed which will enable noninvasive studies of dynamic leukocyte-endothelial interactions and molecular expression at high sensitivities and signal to noise ratios. This multispectral approach will allow the *in vivo* distinction of up to four different cell types or proteins in the same imaging specimen at sub-micron resolutions. Continuous imaging at millisecond intervals will be performed to capture high-velocity cell motility through major vessels as well as the microcirculation.

Size-tunable QD nanocrystals will be used to specifically-label multiple proteins expressed on leukocytes or endothelial cells. It is possible to detect each protein simultaneously in the retinal circulation due to the distinct spectral signatures encoded by the QD bioconjugates. QD emission peaks are narrow and intense, minimizing spectral overlap while exhibiting high signal to background ratios. QDs are amenable to conjugation of antibodies or peptides to their surface, as well as surface engineering of polymers designed to stabilize them or improve bioconjugation efficiency(24). Only one excitation source is necessary to visualize all nanocrystals, in contrast to methods using fluorophores which require a separate excitation wavelength for each fluorophore.

The proposed retinal imaging approach is based on an inverted fluorescence microscope equipped with xenon flashlamp and metal halide excitation lamps. This apparatus was originally developed as part of an optical technique to track vascular permeability changes in the retina (25). This technique has been used to track acridine orange labeled leukocytes in a rat retina. An example of a video frame from one of these sequences is shown in **Figure 2**. In this frame the moving AO labeled cells are captured as well-defined white dots (arrows) by the 4 ms flashlamp illumination. These results suggested that this platform in combination with brighter, specific probes would enable us to noninvasively monitor cells and proteins in inflammatory disease in the retina.

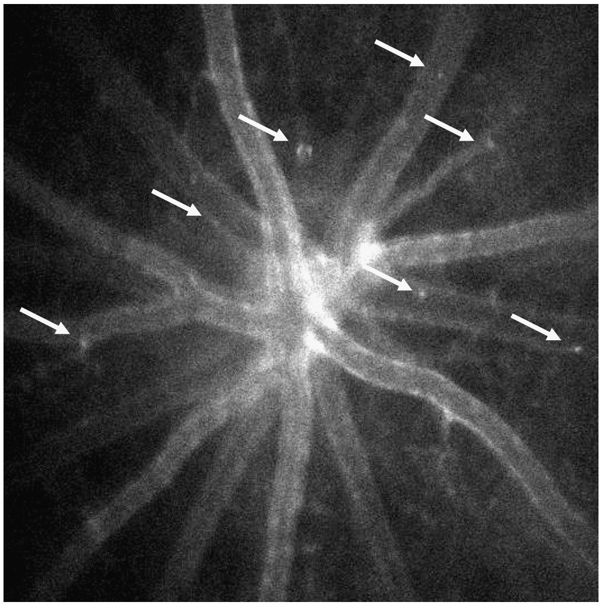

Figure 2. *In vivo* tracking of acridine orange labeled cells (arrows) in a rat retina illuminated with a flashlamp.

Nanoparticulate surface engineering strategies for enhanced in vivo half-life and targeting specificity: PEGylation, site-specific bioconjugation of proteins, and Mab fragmentation

The success of this quantum dot-based multispectral imaging approach is highly-dependent on the probe's affinity and specificity for the target of interest. In utilizing quantum dots or other nanoparticles for the *in vivo* detection of cells and biomolecules in disease, several physiological factors must be addressed in surface engineering processes. First, the body has several tissues, primarily the liver and spleen, which actively retain nanoparticles as part of their role in the reticuloendothelial system (RES) (22, 26). The major nanoparticulate modification employed to evade RES uptake for as long as possible has been PEGylation. Polyethylene glycol (PEG) is well-known for its ability to diminish nanocarrier clearance by the reticuloendothelial system and inhibiting protein surface adsorption. This is a consequence of the hydrophilic exclusion volume exerted by the freely mobile polymer chain of the carrier surface. This is analogous to having a surface whereby a hydrophilic tail whips several angstroms from side to side, essentially whipping away hydrophobic molecules which might normally bind to the surface, an occurrence which might induce immune clearance via opsonization. This strategy has been recently utilized for the protection of therapeutic proteins, as reinforced by the increasing number of PEGylated drugs in the clinic, such as PEGASYS (interferon alfa-2b, Roche) and Exubera (inhaled insulin, Pfizer). In addition, PEGylation has been reported to reduce nonspecific binding of quantum dot nanocrystals to cell surfaces *in vitro* (27), and more importantly, to reduce RES uptake *in vivo* (26, 28).

The next challenge to be considered when designing a nanoparticulate targeting system *in vivo* involves the development of a surface modification strategy which retains the full functionality of the targeting moiety. In many targeting paradigms, the surface ligand may be a biomolecule which is not recognized as foreign by the body, such as folate and transferrin. However, in a large fraction of nanoparticulate targeting methods, antibodies, primarily immunoglobulin G (IgG) proteins are employed. Whole IgG contain two F(ab) regions, which contain the antigen-binding site, as well as a Fc fragment, a species-conserved sequence which is responsible for immune recognition of the Mab. Fc-mediated opsonization and clearance through phagocytes with Fc receptors, such as macrophages, are potential sources of nanoparticulate clearance as well, unless the Fc fragment can be shielded from such recognition. Two general methods have been reported which aim to combat this clearance mechanism; however, it must be noted that these studies have only examined Mab clearance itself, rather than nanoparticle-Mab complex clearance. The first method is to enzymatically-digest the IgG molecule at a specific site, so as to separate the active F(ab) or $F(ab)_2$ fragment from the Fc fragment, as can be accomplished with pepsin or papain/ficin, respectively (5, 29, 30). By utilizing digestion schemes that yield a divalent ($F(ab)_2$) Mab fragment, a higher affinity Mab is derived relative to the monovalent (F(ab)) form. However, if the Mab is to be covalently cross-linked to nanoparticle surfaces, a significant problem further compromising Mab affinity would result by conjugating the $F(ab)_2$ form. Nanoparticles are cross-linked to antibodies (whether in their fragmented or whole form) using amine residues, which are usually critical for antigen-binding activity. When the Mab to be conjugated to a nanoparticle is in its whole ($Fc + F(ab)_2$) form, antibodies which are cross-linked via the

Fc region (which contains many lysine amino acids bearing amine groups) maintain their antigen-binding affinity (i.e. antigen-binding region amines are not modified). However, if the Fc fragment is absent, then there is no alternative but to cross-link amines used for antigen-binding to the nanoparticle. Nonspecific amine-cross-linking has thus been implicated in the loss of function of antibodies, especially in the case of Mab $F(ab)_2$ conjugation (5, 31). In contrast, the F(ab) fragmentation reaction (using pepsin) is capable of yielding an Mab fragment without an Fc region which bears a *single*, *site-specific* unpaired cysteine residue (normally used to link F(ab) fragments by disulfide bridges) (29). This residue is often the only cysteine in the entire IgG, and is located in the hinge region of the Mab which is not involved in antigen-binding. Using specific sulfhydryl-reactive chemistries, nanoparticles can be site-specifically conjugated to F(ab), such that Fc-mediated nanoparticulate clearance is eliminated, and antigen-binding affinity of the F(ab) is not obliterated by nonspecific amine chemistries as in the divalent case. However, as a result of this tradeoff for site-specific conjugation (to avoid nanoparticle cross-linking induced deactivation of the Mab), only the inherently lower affinity, monovalent form of Mab is attached on the nanoparticle surface. A final concern with this first method of Mab engineering is that enzymatic digestion of antibodies is a complex process, with the procedure being significantly sensitive to the host species of the Mab. For example, Mouse IgG subclass 2 antibodies can be digested by papain, whereas IgG subclass 1 antibodies do not cleave sufficiently in response to the enzyme, requiring a completely different enzyme, ficin (Pierce, Rockland, IL), to accomplish the task. Empirical testing of optimal procedures for each Mab can be very costly and time-consuming, and there is no guarantee of successful, high-efficiency digestion.

To circumvent the various problems brought by Mab fragmentation techniques, recombinant protein engineering strategies have emerged recently, whereby vectors are engineered to generate Mab fragments with site-specific linker sites (31, 32). Furthermore, by utilization of PEG linkers with divalent cysteine-reactive arms, Mab fragments (specifically scFv, or single-chain Mab fragments) can be "glued" together to create an Mab construct with similar affinity to a $F(ab)_2$. While this may be an optimal method for the site-specific PEGylation of antibodies for prolonged circulation time with preserved target affinity, it has not been applied to nanoparticulate surface engineering, nor is it clear that such a strategy could be applied without extensive optimization. Furthermore, Mab production using this strategy would be potentially very time-consuming and costly, especially in the case where multiple such antibodies were to be produced.

In Aim 1 a strategy for masking the Fc region of the Mab will be tested, by adsorbing Fc-specific $F(ab)_2$ fragments to the QD-Mab surfaces. We hypothesize that the steric hindrance imposed by the Fc-blocking Mab would inhibit Fc-mediated clearance mechanisms in the body, such as complement fixation and Fc receptor binding. Should this strategy prove successful in reducing nanoparticulate clearance, it would constitute a time-saving, inexpensive Mab engineering method that could be applied to nanoparticle-Mab constructs and antibodies alike to reduce immune reactions for improved *in vivo* targeting.

Advantages and potential applications of QD-based retinal imaging platform

The unique features of this technique are high signal intensity, the ability to noninvasively detect both cells and cell surface markers simultaneously *in vivo* with high spatial and temporal resolution, the need for only one excitation source in the visible spectrum, and the optical accessibility to perform continuous imaging for the collection of real-time data. Currently, no other system currently available has combined all of these features for *in vivo* imaging applications. In addition, the surface engineering strategies proposed in Aim 1 are likely to enhance the specificity of the circulating bioconjugates, thus minimizing noise, and due to the engineering of site-specific cross-linking sites on the Mab, the QD probes should have very high affinity for their epitopes.

The capability to image multiple proteins and cells simultaneously on any time scale with striking clarity would be a major advancement in the field of *in vivo* molecular imaging. Specifically, the utility of this approach will become increasingly important in the design of diagnostic assays and therapeutic strategies, in which the monitoring and/or targeting of multiple suspected mediators of inflammation is critical to an improved prognosis. In addition to elucidating the key cells and proteins in inflammation, this strategy certainly can be extended, for example, to the tracking of homing precursor cells and proteins in angiogenesis, for which the corneal pocket is a widely-accepted model (33), as well as molecular profiling in a number of ocular diseases ranging from glaucoma, macular degeneration, and diabetic retinopathy, devastating diseases which impact a large population and necessitate *in vivo* therapeutic targets and early diagnostic indicators. Flow cytometric analysis of any circulating cell type via microscopic analysis of the retinal circulation is feasible with this technology, which might facilitate the development of imaging applications which seek out circulating metastatic cells to monitor tumor progression.

From a surface engineering standpoint, it is likely that Mab engineering would be equally effective with other classes of Mab-conjugated nanoparticles, such as gold nanoparticles for ablative targeting of diseased tissue, iron oxide nanoparticles for cancer imaging, or Mab-conjugated liposomes. The PEGylation chemistry is also readily applied to most nanoparticles which are to be employed for *in vivo* targeting; in addition, even non-targeted nanoparticles used for vascular imaging, or for passive tumor accumulation in drug delivery applications employing passive retention in the leaky vasculature which supplies it, would most likely benefit from increased circulation time for prolonged velocity calculations or maximal drug retention, for example.

Background and Significance: Aim 2 - Develop entrapment-based surface engineering strategy to facilitate multimodal nanoparticulate applications: Solid Lipid Nanoparticles for Bioimaging and Drug Delivery

Rationale

Given the novel properties conferred upon nanoscale devices of unimodal functionality, it has quickly become relevant that composite structures consisting of nanoparticulates of various functionalities can be delivered within the same package, given the proper surface engineering strategy. Multimodal nanoscale devices would permit the usage of multiple imaging modalities in biology and medicine to extensively characterize disease processes with the feature of co-registration, for example, by using *in* *vivo* MRI in conjunction with fluorescence microscopy in histological analysis to correlate with *in vivo* findings. By packaging diagnostic and therapeutic reagents within the same vehicle, detailed pharmacokinetic and pharmacodynamic studies would also be enabled, for example, by conducting biodistribution studies of candidate drugs as assessed by optical or magnetic resonance reporter nanoparticles.

The suitable multimodal nanoparticle platform would consist of a biocompatible, well-tolerated biomaterial, either natural or synthetic, which is amenable to the encapsulation or entrapment of nanoscale compounds of varying physical and chemical properties. Specifically, the carrier, whether having a hollow core and membranous bilayer, as liposomes, or having a glassy, porous interior, such as some polymeric structures, should ideally be capable of bearing hydrophobic and hydrophilic, charged or neutral, or high (MDa) and low molecular weight (>500 Da) compounds. While the internal modularity must be accommodating, equally important is the nanoparticle surface. By surface-tuning the nanoparticle surface with bioactive ligands such as targeting antibodies or CPPs, the ultrafunctional construct would behave as one nanoparticle in a biological environment. Should the carrier be capable of holding multiple encapsulated probes, high signal to noise ratio imaging and the delivery of therapies with maximum treatment efficiency can be carried out relative to single nanoparticles.

Current Techniques for the Design of Multimodal Nanoparticles

The first multimodal applications utilizing nanoparticles generally consisted of single probes bearing dual functionalities, an example being gold nanoshells, the thickness and core radius of which can be tuned to scatter and absorb photons at distinct NIR-range wavelengths for deep tissue penetration. This feature, combined with the engineering of bioactive functionalities on the nanoshell surface, together form a HER2-targeted, photothermosensitive optical contrast agent(*34*-*36*). A number of multimodal strategies are in development by specialized drug delivery companies, utilizing pumps, microchips, and various biosensors (ALZA, Epic Therapeutics, Emisphere Technology, Alkermes). Recent device innovations for bioimaging and drug delivery reported in the literature attest to the high efficacy of multimodal approaches. Liposomes were engineered to bear both quantum dots and the T1 magnetic resonance contrast agent Gadolinium for dual-modality imaging at levels sufficient to detect tumor angiogenesis (*37, 38*). In a magnetooptical nanoparticulate application, Cy5 dye conjugated with dextran cross-linked iron oxide nanoparticles were utilized to detect atherosclerotic plaques via inflammatory biomarkers, using both MRI and *in vivo* optical imaging(20, 21). In an innovative combinative therapeutic approach for combating tumors, an anti-angiogenic agent was layered above a sustained release chemotherapeutic agent to achieve a temporally-controlled "nanocell (*39*)." Thus, both lipid-based and polymeric-based approaches have been demonstrated to be promising platforms for multimodal systems, in addition to biologically (e.g. dextran)- engineered approaches.

Solid Lipid Nanoparticle-Based Multimodal Nanoparticles: Potential Advantages

The aforementioned works are only a few examples demonstrating the diversity of multimodal approaches that are possible for detailed studies of biological processes and disease in living systems. However, as this field is in its infancy, there are as expected some drawbacks which require consideration should this area progress further in potential. First, many multimodal approaches seek to complex only a few nanoparticles together, to create bimodal point sources, such as Cy5-iron oxide nanoparticle constructs (21). While initial studies demonstrate that signal output is sufficient for the detection of disease in animal models, an approach adapted for hi-fidelity imaging of disease in humans might benefit from a multimodal carrier engineered to bear multiple cargoes, perhaps 10-100 nanoparticles within one carrier. Indeed, in the case of T2 relaxing agents, a high density of the reagent at the target site would provide excellent signal over background, a welcome advantage for the detection of hepatocellular carcinomas for which the nanoparticle is currently utilized (*40*). In addition, it is important to consider a major common denominator of the aforementioned nanoparticulate systems which hinder their transition from laboratory testing to clinical implementation: regulatory issues and potential for scaling-up of production. For example, PLGA nanoparticles, recalling their ability to be internalized nonspecifically into endosomes followed by triggered escape, have the potential to degrade within cell bodies, a process which due to the carrier alone has been associated with cytotoxicity. Furthermore, it has been a highly-difficult task to scale up PLGA nanoparticle production lines, thus limiting this polymer application to biomedical implants, such as Zoladex, as well as large microparticulate forms which are too large for intracellular transport. In addition to regulatory concerns and production difficulties is the issue of cost. Liposomes, for example, are very expensive to make, a fact which hinders the majority of candidate liposomal formulations in the pharmaceutical industry. As individual liposomal formulations are costly, it is unlikely that production of liposomes bearing multiple cargoes would be economically feasible, unless it posed a very high-impact detection and/or treatment reagent. A major contributor to the cost of nanoparticulates like these involve the time-consuming steps and multiple resources required for synthesis. Evaporation, cooling, centrifugation, emulsion, and mixing steps to generate pure nanoparticles with acceptable loading efficiencies can be tedious and are not only costly but add to the challenge of scaling-up production. Next, while each nanoparticulate system has its own advantages supporting their potential candidacy for multimodal systems, there are still a host of disadvantages when evaluating the physicochemical properties of the carriers themselves. PLGA, for instance, has been associated with intraparticle cargo degradation, due to the internal acidic environment created by ester hydrolysis of the polymer surface, as demonstrated with a drop in fluorescence of FITC-Albumin with PLGA microspheres (*41*). Liposomes are associated with a variety of physical stability issues, making long-term storage and regular drug administration a challenge. While there are countless potential applications of liposomal formulations in the literature, the expectations have clearly not matched its potential, having been first invented in 1913 and the main focus of hundreds of R&D funding initiatives.

In light of these observations, a nanoparticulate system for the development of multimodal systems for bioimaging and drug delivery for the purpose of enhanced cellular/biomolecular detection should ideally have the following characteristics: potential for scale-up of production, a capacity to accommodate compounds of varying physicochemical properties (size, charge, solubility, e.g.), amenability to presentation of multiple surface functionalities (polymers, ligands, etc.), should be a solid candidate for regulatory agency approval by using GRAS (generally recognized as safe) standards among others, and lastly, should be as stable as possible under varying storage conditions and administration regimens (intravenous, intraocular, etc.).

The hypothesis of Aim 2 is that an approach not described for multimodal nanomedical or nanobiological systems, dubbed functionalized solid lipid nanoparticles (fSLN), is a solid starting material strategy which could address some or all of the expectations for a successful multifunctional system. A class of solid lipids were identified which could be formulated into nanoparticles ranging in average size from 35-800nm depending on process parameters. Nanoparticulate formation is accomplished by the solvent-assisted formation of a microemulsion. The solid lipid, a dry pellet, is dissolved with a solvent composition of tunable polarity, such that the affinity of this organic solution for water is adjusted. Upon the addition of an aqueous phase to the solvent mixture, the hydrophobic packing of the lipid upon exposure to water provides for instantaneous formation of a nanoscale particle, the size of which is determined by solvent polarity. Higher solvent polarity permits rapid phase inversion as water miscibility is higher, whereas lower solvent polarity likely extends the nanoparticle packing time, allowing for larger-sized nanoparticles to form. The instantaneous lipid packing which occurs upon organic-aqueous phase inversion is thought to readily entrap any species dissolved in either phase.

Summary

The three surface engineering strategies proposed here represent an investigation into the improvement of nanoparticulate probe functionality, to facilitate the development of diverse and powerful applications in biology and medicine. The dissertation focused specifically on two challenging problems, the enhancement of nanoscale device *in vivo* targeting, and the development of multifunctional devices. The result of this research was a framework enabling nanodevice targeting to specific destinations within tissues or cells, for the purpose of high-resolution bioimaging using multiple imaging modalities.

The first manuscript describes efforts to perform multiplexed *in vivo* retinal vascular imaging using quantum dots functionalized with modified, Fc-blocked antibodies, in rat models of diabetes and ocular inflammation. This work was published in *Bioconjugate Chemistry* in Fall 2007 (*42*). The second manuscript extends the strategy of using quantum dots to image multiple cell types in pathology by incorporating cell-penetrating peptide-coated quantum dot nanocrystals to image monocytes and T lymphocyte recruitment to atherosclerotic lesions. This work was submitted to the *Journal of Lipid Research* in April 2008. Chapters V and VI describe the synthesis and characterization of solid lipid nanoparticles (SLN), unique endothelial barrier translocation properties conferred upon SLN *via* surface engineering, and cell membrane translocation properties of multimodal SLN constructs. Chapter V was published in *IEEE Transactions on NanoBioscience* in March 2008 (*43*).

References

(1) Chen, Q., Tong, S., Dewhirst, M. W., and Yuan, F. (2004) Targeting tumor microvessels using doxorubicin encapsulated in a novel thermosensitive liposome. *Mol Cancer Ther 3*, 1311-7.

(2) Cook, R. O., Pannu, R. K., and Kellaway, I. W. (2005) Novel sustained release microspheres for pulmonary drug delivery. *J Control Release 104*, 79-90.

(3) Costantino, L., Gandolfi, F., Tosi, G., Rivasi, F., Vandelli, M. A., and Forni, F. (2005) Peptide-derivatized biodegradable nanoparticles able to cross the blood-brain barrier. *J Control Release 108*, 84-96.

(4) Kirpotin, D., Park, J. W., Hong, K., Zalipsky, S., Li, W. L., Carter, P., Benz, C. C., and Papahadjopoulos, D. (1997) Sterically stabilized anti-HER2 immunoliposomes: design and targeting to human breast cancer cells in vitro. *Biochemistry 36*, 66-75.

(5) Chapman, A. P., Antoniw, P., Spitali, M., West, S., Stephens, S., and King, D. J. (1999) Therapeutic Mab fragments with prolonged in vivo half-lives. *Nat Biotechnol 17*, 780-3.

(6) Wang, Y. X., Hussain, S. M., and Krestin, G. P. (2001) Superparamagnetic iron oxide contrast agents: physicochemical characteristics and applications in MR imaging. *Eur Radiol 11*, 2319-31.

(7) Gao, X. H., Cui, Y. Y., Levenson, R. M., Chung, L. W. K., and Nie, S. M. (2004) In vivo cancer targeting and imaging with semiconductor quantum dots. *Nature Biotechnology 22*, 969-976.

(8) Kim, S., Lim, Y. T., Soltesz, E. G., De Grand, A. M., Lee, J., Nakayama, A., Parker, J. A., Mihaljevic, T., Laurence, R. G., Dor, D. M., Cohn, L. H., Bawendi, M. G., and Frangioni, J. V. (2004) Near-infrared fluorescent type II quantum dots for sentinel lymph node mapping. *Nature Biotechnology 22*, 93-97.

(9) Lidke, D. S., Nagy, P., Heintzmann, R., Arndt-Jovin, D. J., Post, J. N., Grecco, H. E., Jares-Erijman, E. A., and Jovin, T. M. (2004) Quantum dot ligands provide new insights into erbB/HER receptor-mediated signal transduction. *Nature Biotechnology 22*, 198-203.

(10) Stroh, M., Zimmer, J. P., Duda, D. G., Levchenko, T. S., Cohen, K. S., Brown, E. B., Scadden, D. T., Torchilin, V. P., Bawendi, M. G., Fukumura, D., and Jain, R. K. (2005) Quantum dots spectrally distinguish multiple species within the tumor milieu in vivo. *Nat Med 11*, 678-82.

(11) Frieri, M. (2005) Asthma concepts in the new millennium: update in asthma pathophysiology. *Allergy Asthma Proc 26*, 83-8.

(12) Ulbrich, H., Eriksson, E. E., and Lindbom, L. (2003) Leukocyte and endothelial cell adhesion molecules as targets for therapeutic interventions in inflammatory disease. *Trends Pharmacol Sci 24*, 640-7.

(13) Wellen, K. E., and Hotamisligil, G. S. (2005) Inflammation, stress, and diabetes. *J Clin Invest 115*, 1111-9.

(14) Anderson, D. W. (2001) Cytokines as drug targets. *IDrugs 4*, 375-7.

(15) Blankenberg, S., Barbaux, S., and Tiret, L. (2003) Adhesion molecules and atherosclerosis. *Atherosclerosis 170*, 191-203.

(16) McHale, J. F., Harari, O. A., Marshall, D., and Haskard, D. O. (1999) Vascular endothelial cell expression of ICAM-1 and VCAM-1 at the onset of eliciting contact hypersensitivity in mice: evidence for a dominant role of TNF-alpha. *J Immunol 162*, 1648-55.

(17) Sans, M., Panes, J., Ardite, E., Elizalde, J. I., Arce, Y., Elena, M., Palacin, A., Fernandez-Checa, J. C., Anderson, D. C., Lobb, R., and Pique, J. M. (1999) VCAM-1 and ICAM-1 mediate leukocyte-endothelial cell adhesion in rat experimental colitis. *Gastroenterology 116*, 874-83.

(18) Kimura, H., Kiryu, J., Nishiwaki, H., and Ogura, Y. (1995) A new fluorescent imaging procedure in vivo for evaluation of the retinal microcirculation in rats. *Curr Eye Res 14*, 223-8.

(19) Hossain, P. (1999) Scanning laser ophthalmoscopy and fundus fluorescent leucocyte angiography. *Br J Ophthalmol 83*, 1250-3.

(20) Tsourkas, A., Shinde-Patil, V. R., Kelly, K. A., Patel, P., Wolley, A., Allport, J. R., and Weissleder, R. (2005) In vivo imaging of activated endothelium using an anti-VCAM-1 magnetooptical probe. *Bioconjug Chem 16*, 576-81.

(21) Kelly, K. A., Allport, J. R., Tsourkas, A., Shinde-Patil, V. R., Josephson, L., and Weissleder, R. (2005) Detection of vascular adhesion molecule-1 expression using a novel multimodal nanoparticle. *Circ Res 96*, 327-36.

(22) Berry, C., and Curtis, A. (2003) Functionalisation of magnetic nanoparticles for applications in biomedicine. *JOURNAL OF PHYSICS D-APPLIED PHYSICS 36*, R198-R206.

(23) Watson, A., Wu, X. Y., and Bruchez, M. (2003) Lighting up cells with quantum dots. *Biotechniques 34*, 296-+.

(24) Rosenthal, S. J., Tomlinson, A., Adkins, E. M., Schroeter, S., Adams, S., Swafford, L., McBride, J., Wang, Y. Q., DeFelice, L. J., and Blakely, R. D. (2002) Targeting cell surface receptors with ligand-conjugated nanocrystals. *Journal of the American Chemical Society 124*, 4586-4594.

(25) Russ, P. K., Gaylord, G. M., and Haselton, F. R. (2001) Retinal vascular permeability determined by dual-tracer fluorescence angiography. *Ann Biomed Eng 29*, 638-47.

(26) Ballou, B., Lagerholm, B. C., Ernst, L. A., Bruchez, M. P., and Waggoner, A. S. (2004) Noninvasive imaging of quantum dots in mice. *Bioconjug Chem 15*, 79-86.

(27) Bentzen, E. L., Tomlinson, I. D., Mason, J., Gresch, P., Warnement, M. R., Wright, D., Sanders-Bush, E., Blakely, R., and Rosenthal, S. J. (2005) Surface modification to reduce nonspecific binding of quantum dots in live cell assays. *Bioconjug Chem 16*, 1488-94.

(28) Akerman, M. E., Chan, W. C. W., Laakkonen, P., Bhatia, S. N., and Ruoslahti, E. (2002) Nanocrystal targeting in vivo. *Proceedings of the National Academy of Sciences of the United States of America 99*, 12617-12621.

(29) Hermanson, G. T. (1996) *Bioconjugate techniques*, Academic Press, San Diego.

(30) Lamoyi, E., and Nisonoff, A. (1983) Preparation of F(ab')2 fragments from mouse IgG of various subclasses. *J Immunol Methods 56*, 235-43.

(31) Albrecht, H., Burke, P. A., Natarajan, A., Xiong, C. Y., Kalicinsky, M., DeNardo, G. L., and DeNardo, S. J. (2004) Production of soluble ScFvs with C-terminal-free thiol for site-specific conjugation or stable dimeric ScFvs on demand. *Bioconjug Chem 15*, 16-26.

(32) Natarajan, A., Xiong, C. Y., Albrecht, H., DeNardo, G. L., and DeNardo, S. J. (2005) Characterization of site-specific ScFv PEGylation for tumor-targeting pharmaceuticals. *Bioconjug Chem 16*, 113-21.

(33) Gross, J., Azizkhan, R. G., Biswas, C., Bruns, R. R., Hsieh, D. S., and Folkman, J. (1981) Inhibition of tumor growth, vascularization, and collagenolysis in the rabbit cornea by medroxyprogesterone. *Proc Natl Acad Sci U S A 78*, 1176-80.

(34) Loo, C., Hirsch, L., Lee, M. H., Chang, E., West, J., Halas, N., and Drezek, R. (2005) Gold nanoshell bioconjugates for molecular imaging in living cells. *Opt Lett 30*, 1012-4.

(35) Loo, C., Lowery, A., Halas, N., West, J., and Drezek, R. (2005) Immunotargeted nanoshells for integrated cancer imaging and therapy. *Nano Lett 5*, 709-11.

(36) Loo, C., Lin, A., Hirsch, L., Lee, M. H., Barton, J., Halas, N., West, J., and Drezek, R. (2004) Nanoshell-enabled photonics-based imaging and therapy of cancer. *Technol Cancer Res Treat 3*, 33-40.

(37) Mulder, W. J., Koole, R., Brandwijk, R. J., Storm, G., Chin, P. T., Strijkers, G. J., de Mello Donega, C., Nicolay, K., and Griffioen, A. W. (2006) Quantum dots with a paramagnetic coating as a bimodal molecular imaging probe. *Nano Lett 6*, 1-6.

(38) van Tilborg, G. A., Mulder, W. J., Chin, P. T., Storm, G., Reutelingsperger, C. P., Nicolay, K., and Strijkers, G. J. (2006) Annexin A5-conjugated quantum dots with a paramagnetic lipidic coating for the multimodal detection of apoptotic cells. *Bioconjug Chem 17*, 865-8.

(39) Sengupta, S., Eavarone, D., Capila, I., Zhao, G., Watson, N., Kiziltepe, T., and Sasisekharan, R. (2005) Temporal targeting of tumour cells and neovasculature with a nanoscale delivery system. *Nature 436*, 568-72.

(40) Bulte, J. W., and Kraitchman, D. L. (2004) Iron oxide MR contrast agents for molecular and cellular imaging. *NMR Biomed 17*, 484-99.

(41) Zhu, G., Mallery, S. R., and Schwendeman, S. P. (2000) Stabilization of proteins encapsulated in injectable poly (lactide- co-glycolide). *Nat Biotechnol 18*, 52-7.

(42) Jayagopal, A., Russ, P. K., and Haselton, F. R. (2007) Surface engineering of quantum dots for in vivo vascular imaging. *Bioconjug Chem 18*, 1424-33.

(43) Jayagopal, A., Sussman, E. M., and Shastri, V. P. (2008) Functionalized Solid Lipid Nanoparticles for Transendothelial Delivery. *IEEE Trans Nanobioscience 7*, 28-34.

CHAPTER III

SURFACE ENGINEERING OF QUANTUM DOTS FOR IN VIVO VASCULAR IMAGING

Ashwath Jayagopal
Patricia K. Russ
Frederick R. Haselton

Department of Biomedical Engineering
Vanderbilt University
Nashville, Tennessee

Bioconjugate Chemistry 18:1424-1433. 2007.

Abstract

Quantum dot-antibody bioconjugates (QD-mAb) were synthesized incorporating PEG crosslinkers and Fc-shielding mAb fragments to increase *in vivo* circulation times and targeting efficiency. Microscopy of endothelial cell cultures incubated with QD-mAb directed against cell adhesion molecules (CAMs), when shielded to reduce Fc-mediated interactions, were more specific for their molecular targets. *In vitro* flow cytometry indicated that surface engineered QD-mAb were capable of labeling leukocyte subsets with minimal Fc-mediated binding. Nontargeted QD-mAb nanoparticles with Fc-blockade featured 64% (endothelial cells) and 53% (leukocytes) lower nonspecific binding than non Fc-blocked nanoparticles. Spectrally-distinct QD-mAb targeted to the cell adhesion molecules (CAMs) PECAM-1, ICAM-1, and VCAM-1 on the retinal endothelium in a rat model of diabetes were imaged *in vivo* using fluorescence angiography. Endogenously-labeled circulating and adherent leukocyte subsets were imaged in rat models of diabetes and uveitis using QD-mAb targeted to RP-1 and CD45. Diabetic rats exhibited increased fluorescence in the retinal vasculature from QD bioconjugates to ICAM-1 and VCAM-1 but not PECAM-1. Both animal models exhibited leukocyte rolling and leukostasis in capillaries. Examination of retinal whole-mounts prepared after *in vivo* imaging confirmed the fluorescence patterns seen *in vivo*. Comparison of the timecourse of retinal fluorescence from Fc-shielded and non-Fc-shielded bioconjugates indicated nonspecific uptake and increased clearance of the non-Fc-shielded QD-mAb. This combination of QD surface design elements offers a promising new *in vivo* approach to specifically label vascular cells and biomolecules of interest.

Introduction

Inflammation is a complex process involving numerous cell types and surface proteins. It is characterized by leukocyte rolling and tethering along endothelial cells followed by transmigration into tissue, where their immunodefensive functions, such as phagocytosis, are elicited (1, 2). Undesirable provocation of the inflammatory response is thought to be a detrimental feature of numerous diseases such as diabetes, atherosclerosis, and asthma (3-6). Treatment of inflammatory disease is challenging due to uncertainties associated with the roles of many of the cellular and biomolecular mediators. However, one developing strategy hinders inflammation by blockade of cell surface receptors either on the endothelium or on circulating leukocytes (7-9).

Detailed information about molecular mediators of inflammation might be acquired through *in vivo* imaging methods, since they can provide real-time data concerning the spatial and temporal dynamics of cellular activities and molecular expression throughout the time course of the disease. However, disadvantages of current imaging techniques include limited optical accessibility to tissue, invasiveness (10, 11), low or unstable signal intensity due to the use of organic fluorophores (12-14), or low spatial and temporal resolution achieved by the use of radiolabeled antibodies (15). No available technique provides a framework for the simultaneous imaging of multiple molecular participants on moving leukocytes and stationary endothelium and leukocytes in real time.

Imaging inflammation is a difficult task, as the cell types of interest have one or more of the Fcγ receptor family (CD16, CD32, and CD64) which bind to Fc fragments of

Immunoglobulin G (IgG) antibodies with variable affinity (*16*). Binding of bioconjugates to these receptors can yield false-positive results when attempting to detect vascular cell surface targets. In addition, it is well-known that nanoparticulate probes are subject to rapid uptake by the tissues of the reticuloendothelial system, such as liver and spleen (*17*). These immunodefensive mechanisms either serve to rapidly clear the probe from the circulation, or to nonspecifically bind the probe. However, the many advantages afforded by nanoparticles as bioconjugates, particularly quantum dots (QD), which feature size-tunable visible-IR emission spectra, the need for only one excitation source, and high quantum efficiency, warrant new methods to facilitate their continued application (*18, 19*). Recent work has indicated that the surface functionalization of PEG chains on the quantum dot surface can substantially reduce nonspecificity and clearance problems (*20, 21*). In addition, many studies have established QD amenability to bioconjugation and ease of encapsulation in water-soluble coatings (*22*), and its incorporation within targeted *in vivo* imaging applications (*20, 23, 24*).

In this study, we selected spectrally-distinct quantum dot (QD) nanocrystals to enable high-resolution, multispecies imaging using a previously developed, non-invasive *in vivo* retinal vascular imaging system (*25*). In this application, which pursues the detection of vascular targets, mitigation of nonspecific uptake and clearance mechanisms are essential. To address this, monoclonal antibodies (mAb) targeting leukocytes, neutrophils (*26*) or the cell adhesion molecules PECAM-1, ICAM-1, and VCAM-1 were site-specifically conjugated to PEG-Maleimide-activated QD surfaces via 2-MEA to preserve mAb orientation and binding affinity (*27*). QD-mAb were then adsorbed with Fc-blocking $F(ab)_2$ fragments to reduce nonspecific immunorecognition. When incubated with endothelial cells or leukocytes *in vitro*, the shielded probes were found to be more specific for their targets relative to controls. *In vivo* retinal imaging of streptozotocin (STZ)-treated diabetic rats using QD-mAb revealed upregulation of ICAM-1 and VCAM-1 but not PECAM-1. Imaging of a rat model of Endotoxin-Induced Uveitis (EIU) showed the expected increase in stagnant leukocytes in the microcirculation. The high photostability of QD permitted post-experimental histological observations which confirmed the *in vivo* results. Real-time imaging of QD-IgG_1 conjugates indicated rapid clearance of conjugates lacking Fc-blocking $F(ab)_2$ fragments from the circulation. The distinct spectral emission characteristics of the QD enabled the simultaneous imaging of up to four biomarkers or cell types within the same animal with high specificity.

Experimental Procedures

Synthesis and Characterization of Shielded Quantum Dot-Antibody Conjugates

QD nanocrystals with approximately 80 NH_2 groups/nanoparticle (ITK-NH_2, Invitrogen Corp.) were surface-functionalized with a heterobifunctional PEG-based cross-linker (NHS-PEG-MAL, Nektar Therapeutics) to couple reduced antibodies to the surface, followed by Fc-shielding $F(ab)_2$ surface adsorption as shown in **Scheme 1**. (**1**) 1 uM of QD-ITK-NH_2 (1.2×10^{14} nanoparticles in 200 uL solution) were maleimide-activated by incubation with a 20-fold molar excess of NHS-PEG-MAL (MW: 5218) for 2 hours in PBS with 10 mM EDTA, pH = 7.4 (PBS-EDTA) at room temperature. Excess NHS-PEG-MAL was removed using two exchanges of PBS-EDTA on a 100K MWCO

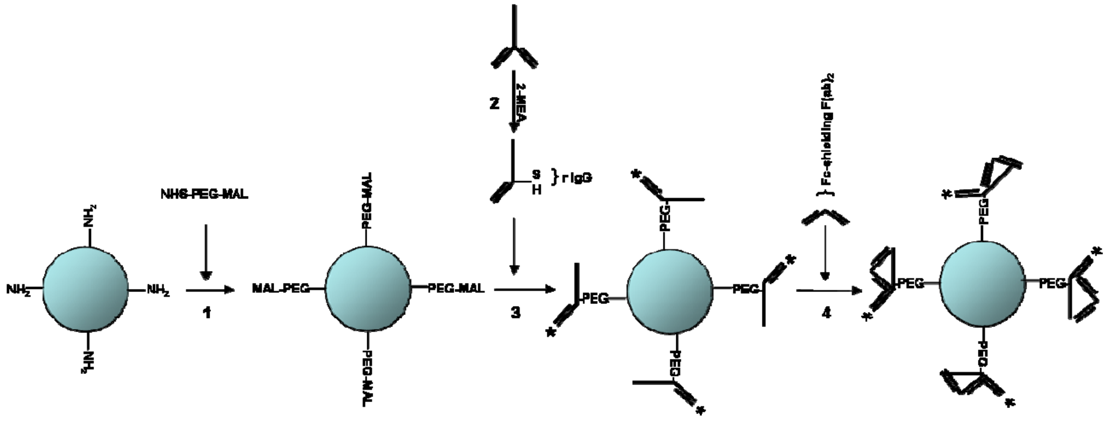

Scheme 1. Schematic of Fc-shielded QD-mAb design. (1) Maleimide activation of QD-NH_2 surface using NHS-PEG(5000)-MAL (N-hydroxysuccinimide-polyethylene glycol-maleimide) crosslinker. (2) Selective hinge region reduction of whole IgG into two functional half IgG (r IgG) with hinge region MAL-reactive sites using 2-mercaptoethylamine (2-MEA). (3) Reaction of r IgG with MAL-activated QD. Reaction is site-specific, preserving activity at antigen-binding sites (*). (4) Adsorption of Fc-specific $F(ab)_2$ against purified QD-r IgG bioconjugates.

Amicon Ultra-4 column. The solution was analyzed qualitatively for the presence of large aggregates (> 200 nm) using fluorescence microscopy, and was filtered through a 100 nm syringe filter if aggregates were observed. (**2**) mAb (**Table 1**) were buffer-exchanged in 500 μg amounts into PBS-EDTA, with two exchanges on a 100K MWCO spin column device (Amicon Ultra-4, Millipore) according to manufacturer-supplied instructions. The retentate was resuspended to 10 mg/mL concentration in PBS-EDTA. The antibodies were then reduced specifically in the hinge region to create two monovalent IgG (r IgG) bearing 1-2 free sulfhydryl groups using 2-mercaptoethylamine (2-MEA, Pierce) (*28*) according to manufacturer's instructions. Briefly, 6 mg of 2-MEA was dissolved in 100 μL of PBS-EDTA, and 1 μL of this solution was added to each 10 μL of mAb solution. The mixture was reacted for 120 min. at 37°C on a slow rocking platform. Excess 2-MEA was removed from mAb using a NAP-5 desalting column (GE Healthcare) pre-equilibrated with degassed PBS-EDTA buffer according to manufacturer's instructions. The presence of free sulfhydryl groups generated from 2-MEA reduction was confirmed using Ellman's reagent (Pierce) on a Nanodrop ND-1000 spectrophotometer according to manufacturer's instructions. (**3**) The QD retentate from (**1**) was then added to the 2-MEA reduced and purified r IgG mixtures and incubated overnight at 4°C. The following day, the reaction was terminated with 1 mg/mL L-cysteine (Sigma) to quench remaining maleimide groups. The QD-r IgG conjugates were purified by gel filtration chromatography according to manufacturer's instructions (Superdex 200, GE Healthcare). Fractions were eluted with PBS into 96-well microplates and evaluated by a UV-Vis and fluorescence spectrophotometry (Nanodrop ND-1000 and ND-3300) or a fluorescence microplate spectrophotometer (Biotek Synergy

HT) in order to identify appropriate QD-mAb fractions and to evaluate conjugation efficiency. In 6 separate conjugations of r IgG_{2a} to QD655, the average conjugation efficiency measured by UV-Vis absorbance spectrophotometry on pooled QD-bound and unbound r IgG fractions was 59.33 ± 11.34%. This corresponds to 18 r IgG/QD. (**4**) The bioconjugate fraction was incubated with goat anti-mouse IgG (Fc-specific) blocking $F(ab)_2$ (Sigma) at molar concentrations equal to primary antibody concentrations for 1 hour at room temperature, and the resulting mixture was filtered through a 0.22 μm syringe filter and stored at 4ºC until use. On the day of animal imaging, bioconjugates were briefly spun in an Eppendorf 5415R microcentrifuge for 10 min. at 10,000g to remove QD-mAb aggregates, reserving the supernatant for use. The supernatant was examined by fluorescence microscopy to ensure the absence of QD aggregates (> 200 nm).

Table 1. Quantum Dot-mAb conjugates.

Study Target (function)	Targeting Monoclonal Antibody	QD Excitation	QD Emission
PECAM-1, endothelial cell (transmigration)	Ms anti-rat CD31 IgG1 (BD)	Excitation Filter E460SPUV v2 peak emission 405nm	525 nm, detection filter 525WB20
ICAM-1, endothelial cell (arrest)	Ms anti-rat CD54 IgG1 (BD)		605 nm, detection filter 605WB20
VCAM-1, endothelial cell (arrest)	Ms anti-rat CD106 IgG1 (BD)		655 nm, detection filter 655WB20
RP-1, neutrophil (unknown)	Ms anti-rat RP-1 IgG2a (BD)		585 nm, detection filter 585WB40 or 620WB90
CD45, leukocytes (multiple essential functions)	Ms anti-rat CD45 IgG1 (BD)		655 nm, detection filter 655WB20
Nonspecific	Ms IgG1 or IgG2a isotype control (BD)		565 nm, detection filter 565WB20

Flow Cytometry

Whole blood was collected in 2 x 3mL aliquots from male Long-Evans rats into BD VACUTAINER tubes spray-lined with K_3EDTA. Erythrocytes were lysed by incubation with BD PharMLyse at a 20:1 ratio of lysis buffer to whole blood for 15 min. in the dark at room temperature to obtain a diffuse red suspension of white blood cells. The solution was then centrifuged at 400 x g in an Allegra X-22R unit with swinging bucket rotor (Beckman) at room temperature. The leukocyte pellet was rinsed in 500 μL PBS (pH = 7.2) containing 0.5% BSA, and 0.1% sodium azide (staining buffer) to reduce shedding of membrane antigens. Each pellet was rinsed twice with staining buffer. The cells were resuspended to a $1x10^6$ leukocytes/mL concentration, and were incubated for 45 minutes with one of the following in staining buffer: 50 nM each of QD585-anti-RP-1 conjugate, QD585-anti-CD45 conjugate, Fc-blocked QD585-isotype control IgG_1, maleimide-activated and L-Cysteine quenched QD585, Fc-blocked QD585-isotype control IgG_{2a}, non Fc-blocked QD585-IgG_{2a} isotype control, or 1 ug Phycoerythrin (PE)-anti-RP-1 conjugate (BD Pharmingen). A separate unlabeled fraction was also retained for analysis. All samples were immediately analyzed (n = 20,000 gated events) using a BD LSR II multicolor flow cytometer equipped with a 488 nm Ar laser. Rat leukocyte subtypes could be readily resolved by forward and side scatter profiles as previously described (*29*). Bandpass emission filters were set at 585/42nm to analyze QD or PE-labeled cells. Analysis was conducted using Flowjo 7.0 (Treestar Software).

Cell Culture and Immunofluorescence Microscopy

YPEN-1 (CRL-2222, ATCC) rat prostate endothelial cells were cultured to confluency on Lab-Tek II 8-well chambered coverslips with media containing Minimum essential medium (Eagle) with 2 mM L-glutamine and Earle's BSS adjusted to contain 1.5 g/L sodium bicarbonate, 0.1 mM non-essential amino acids, and 1.0 mM sodium pyruvate, supplemented with 0.03 mg/ml heparin; fetal bovine serum, 5%. YPEN-1 were stimulated with 30 ng/mL TNF-α in media overnight as previously described (*30*) to upregulate cell adhesion molecules, or incubated with media alone as a control. The next day, YPEN-1 were rinsed with 1 wash of media and incubated with 10 nM amounts of QD bioconjugates for 1hr. at 37°C as follows: QD655-anti-PECAM, QD655-anti-ICAM, QD655-anti-VCAM, QD655 (reactive maleimide group quenched with 1 mg/mL L-Cysteine), and QD-isotype control IgG_1 in Fc-blocked forms as described above or as synthesized without the Fc-blocking step. Cells were then rinsed 6 times in Dulbecco's PBS containing Ca and Mg, pH = 7.4, and incubated with 4% paraformaldehyde in PBS for 15 min at 25°C, followed by rinsing three times, 5 minutes each, with PBS with 50 mM glycine. Fixed cells were imaged using a Nikon TE2000U inverted fluorescence microscope with filter settings as shown in Error! Reference source not found.. These experiments were performed in triplicate. Images were acquired using a Hammamatsu C7780 12-bit color CCD in conjunction with Image Pro Plus 5.1 (Media Cybernetics).

Preparation of Animal Subjects

All experimental procedures were approved by the Vanderbilt University Institutional Animal Care and Use Committee. Diabetes was induced in Long-Evans rats by intraperitoneal injection of 65mg/kg streptozotocin (STZ, Sigma) in 0.1 mM sodium citrate, pH = 4.5, with the same number of rats remaining untreated as experimental controls (n = 6 per group). Elevated blood sugar (> 250mg/dl) was confirmed in STZ treated animals. Endotoxin-Induced Uveitis (EIU) was initiated in Long-Evans rats by intraperitoneal injection of 200 µg lipopolysaccharide. Controls were age-matched untreated rats (n = 6 LPS, n = 3 control). Animals were anesthetized with intraperitoneally-administered 15/85% ketazine/xylazine prior to imaging. Tail vein catheterization was performed for injection of QD-mAb. Both eyes were dilated with 1 drop each of 2.5% phenylephrine hydrochloride and 1% tropicamide ophthalmic solutions (Alcon). The right eye was placed on the plano-concave lens previously filled with 2% methyl cellulose (Aqua Poly-Mount, Polysciences).

In vivo Retinal Imaging

Our imaging design is based on a previously published technique (*25*), in which an inverted fluorescence microscope (TE2000U Eclipse, Nikon) with 4X and 10X objectives and a plano-concave -6 D lens (Edmund Scientific) on the microscope stage were utilized to image the rat retinal circulation. In this study this technique was modified to include a high sensitivity Andor Bioimaging iXon 885 EMCCD camera (Andor Bioimaging), Hamamatsu C7780 color camera, Exfo X-cite 120 metal halide lamp (Exfo Life Sciences), and a pulsed xenon arc flashlamp excitation source (FX 4400, Perkin Elmer) triggered by a function generator configured for square wave output at 20 Hz (Tektronix). The metal halide lamp and flashlamp were utilized for the imaging of stationary endothelial targets and circulating leukocytes, respectively. Following measurements of pre-injection tissue autofluorescence levels in each QD-specific emission channel, QD-mAb were injected via the tail vein catheter. Injectate consisted of 200 *u*L of a 500 nM solution in PBS-EDTA. Initial digital sequences were acquired using exposures ranging from 20 to 200 ms (depending on the QD and the filter set, **Table 1**) at 110 ms intervals. Subsequent sequences were acquired at approximately 30 min. intervals for 2.5 hrs. In four animals, a QD-IgG_1 isotype control was used as a negative control. Animals were sacrificed with 150mg/kg sodium pentobarbital administered via tail vein catheter.

Immunofluorescence Microscopy of Retinal Tissue

Following euthanization of animals, both eyes were enucleated. Retinal flat mounts were prepared of the right eye, which was the eye imaged by our *in vivo* retinal imaging system. Eyes were fixed in 4% paraformaldehyde in PBS overnight and flat-mounted on a microscope slide mounted with fluorescence mounting media. The left eye was fixed in 4% paraformaldehyde and paraffin embedded for sectioning. Sections and flat mounts were analyzed by fluorescence microscopy (Nikon TE 2000U) using the same filters as those used in *in vivo* imaging (**Table 1**).

Image Analysis

For analysis of QD-mAb binding to YPEN-1, fluorescence micrographs acquired under identical settings and conditions (matched cell densities in field of view) were measured in the Red CCD channel (the chip with which QD655 emission is captured) for fluorescence intensity using Image Pro Plus 5.1. From this data the mean Red channel fluorescence intensity was obtained and standard deviation determined. Background correction was performed on image intensities by subtracting the mean Red CCD channel intensity obtained from the same density of unlabeled YPEN-1. Intensities were analyzed for statistical significance using an unpaired 2-tailed *t*-test (SigmaStat 3.0, SYTAT). Background-corrected data was then plotted using SigmaPlot 9.0 (SYSTAT). Statistical significance was interpreted by $P < 0.05$.

For *in vivo* image quantification of leukostasis, the area of image analysis of rat fundi was a circle of two optic disk diameters from the center, allowing for counts of stagnant leukocytes and observations of leukocyte trafficking and cell adhesion molecule expression within major arteries and veins as well as the microcirculation. A leukocyte was assumed to be stagnant if no displacement larger than 1 cell diameter was observed within 60 s of continuous imaging. The number of stagnant QD-labeled cells was quantified for STZ, EIU, and wild-type retinas post-acquisition from digital video using Andor iQ 1.6, and compared using an unpaired 2-tailed *t*-test in SigmaStat 3.0.

Quantitative analysis of Fc-blocked and non Fc-blocked QD-IgG_1 bioconjugates was performed by analyzing 60 consecutive digital frames of wild-type rat retina before and after systemic injection of 500 nM (200 uL) of each probe. An observation area of 2 optic disc diameters from center was utilized for the analysis. Using Andor iQ 1.6 image analysis software, the mean fluorescence intensity of 60 consecutive frames was plotted as a function of time. Data was plotted using SigmaPlot 9.0.

Results

In Vitro Studies

In cell culture studies, the QD655-mAb Fc-shielded conjugates specifically labeled CAMs on TNF-α-stimulated YPEN-1 rat endothelium (TNF+) (**Figure 1A-D, Figure 2B, 2E**). In order to simulate the *in vivo* environment, no traditional immunofluorescence blocking steps (e.g. serum, Fc receptor blocking mAbs) were utilized. Under TNF+ conditions, a statistically-significant increase in Fc-blocked QD655-anti-VCAM binding to YPEN-1 (**Figure 1B, 1D**) was observed, whereas TNF+ conditions did not significantly affect QD655-anti-PECAM binding (**Figure 1A**). These observations were consistent with previous reports (*31, 32*). QD655-anti-ICAM bioconjugates bound TNF+ YPEN-1 by over 10-fold as compared to untreated cells (**Figure 2E**). A strong reduction in nonspecific binding was observed when comparing binding of Fc-blocked and non Fc-blocked QD655-anti-ICAM bioconjugates (**Figure 2A-B, 2E**). A reduction in nonspecific binding was also observed when comparing measured intensities of YPEN-1 labeled with Fc-blocked or non Fc-blocked QD655-isotype control IgG_1 nanoparticles (**Figure 2C-E**), suggesting that the Fc fragment is responsible for a substantial percentage of QD-mAb nonspecific binding. Immunofluorescence analysis of YPEN-1 indicated that non Fc-blocked QD655-mAb constructs were aggregated in focal locations along cell membranes, shown by arrowheads (**Figure 2A-C**). This observation may be due to two features: the upregulation of Fcγ receptors on endothelial cells following TNF-α stimulation, and the patching and capping effect observed previously for Fc receptor-ligand combinations

(*33*). Specifically, patching and capping refers to the accumulation of surface bound IgG-Fc receptor pairs at distinct, punctate locations at the membrane to form clumps of Fc receptor-IgG pairs. This incidence of cap formation was less evident in TNF+ YPEN-1 cells incubated with Fc-blocked bioconjugates (**Figure 2B**). Maleimide-quenched QD which were not conjugated to Mab (**Figure 1C**) did not bind appreciably to cell surfaces. These data collectively suggest that nonspecific binding of unshielded probe was likely due to the binding of mAb Fc fragment to endothelial Fc receptors.

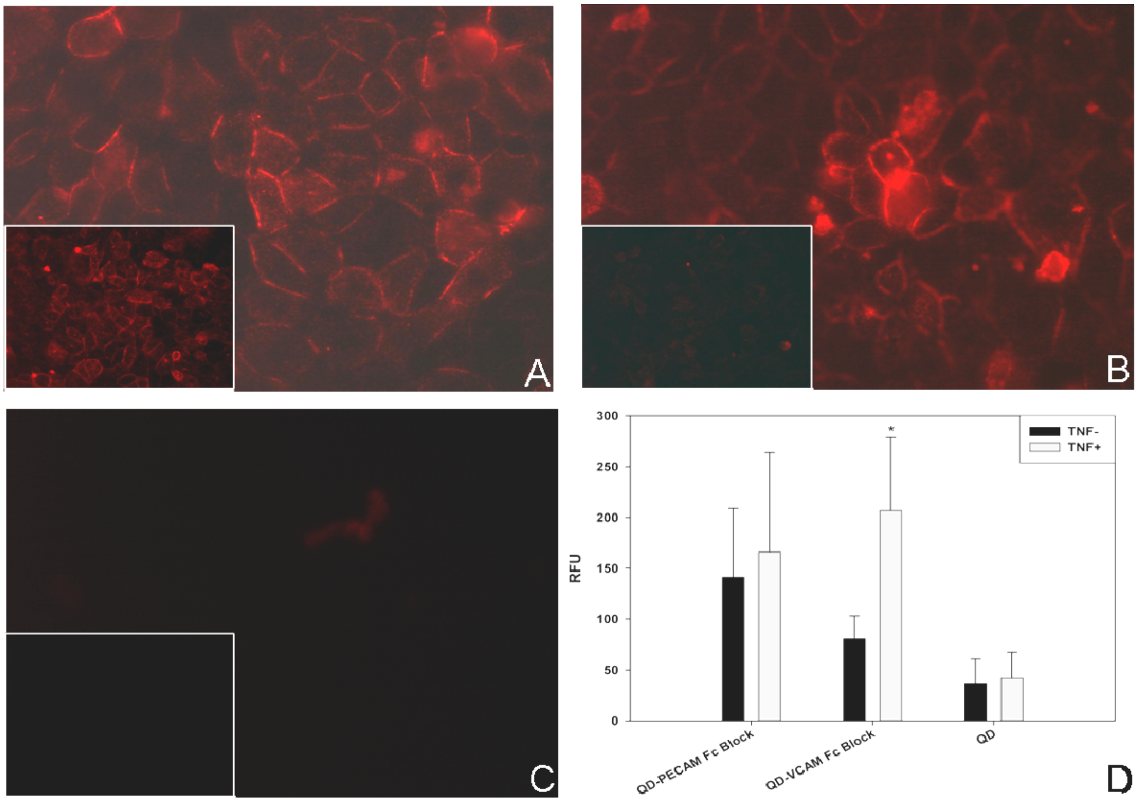

Figure 1. Evaluation of Fc-blocked QD-mAb conjugate specificity toward TNF-α stimulated (TNF+) or untreated (TNF-, image insets) rat endothelial cells (YPEN-1). (A-C) Fluorescence micrographs of QD655-anti-PECAM (A), QD655-anti-VCAM (B), and QD655 (C). Insets show incubation of TNF- YPEN-1 with matched bioconjugates. (D) Mean image intensities from immunofluorescence analysis of TNF+/- YPEN-1 incubated with QD655-mAb bioconjugates (reported as mean + S.D., n=3 images per sample). Intensities for each TNF+ and TNF- pair were compared by t-test for statistical significance ($P < 0.05$ indicated by asterisk).

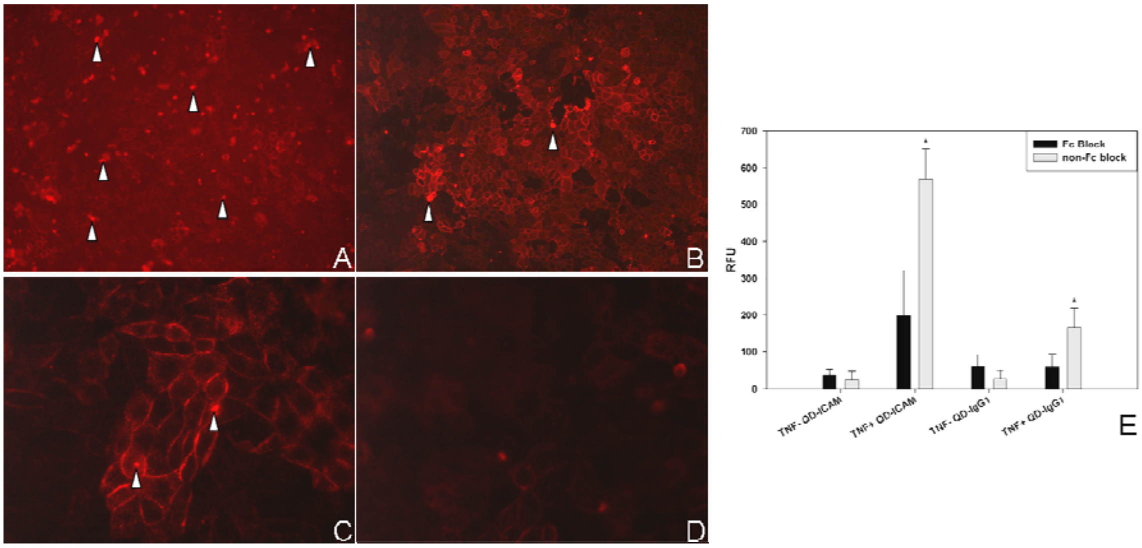

Figure 2. Comparison of Fc-blocked and non Fc-blocked QD655-mAb conjugate specificity toward TNF-α-stimulated YPEN-1 (TNF+). (A-B) TNF+ YPEN-1 incubated with non Fc-blocked (A) and Fc-blocked (B) QD655-anti-ICAM bioconjugates (magnification 100X). Arrowheads indicate possible Fc receptor capping, which was substantially reduced when using Fc-blocked conjugates. (C-D) TNF+ YPEN-1 incubated with non Fc-blocked (C) and Fc-blocked (D) QD655-IgG_1 isotype control bioconjugates, with capping sites labeled with arrowheads (magnification 400X). (E) Mean image intensity analysis reveals lower nonspecific binding of bioconjugates featuring Fc blockade (reported as mean + S.D., n = 3 images per sample). Intensities for each matched Fc-blocked and and non Fc-blocked bioconjugate were compared by t-test for statistical significance ($P < 0.05$ indicated by asterisks).

Fc-blocked QD585-anti-RP-1 (neutrophils) and QD585-anti-CD45 (leukocyte common antigen) were shown to retain bioactivity and specificity *in vitro* (**Figure 3**). QD585-anti-RP-1 conjugates were shown to specifically bind to neutrophils and not other leukocyte subsets (**Figure 3A**), and QD585-anti-CD45 were shown to label the three main subclasses of leukocytes as shown by flow cytometric analysis of erythrocyte-lysed whole blood (**Figure 3B, 3D**). QD-anti-RP-1 was observed to have over 4-fold enhancement in fluorescence over PE-RP-1 (1003 vs. 233), a positive control antibody coupled to phycoerythrin (**Figure 3C**). QD585-IgG2a (matching the isotype of QD585-anti-RP-1), when Fc-blocked with a anti-Fc F(ab)$_2$ fragment, featured 53% lower mean fluorescence levels than that due to the non-Fc-blocked conjugate (**Figure 3C**), indicative of reduced nonspecific binding of Fc-blocked bioconjugates. Fc-blocked QD585-anti-CD45 conjugates used to label leukocytes yielded a mean fluorescence of 1430, over 17-fold greater than cells labeled with Fc-blocked QD-IgG$_1$ isotype control (82) and 22-fold greater than unlabeled cells (65) (**Figure 3D**).

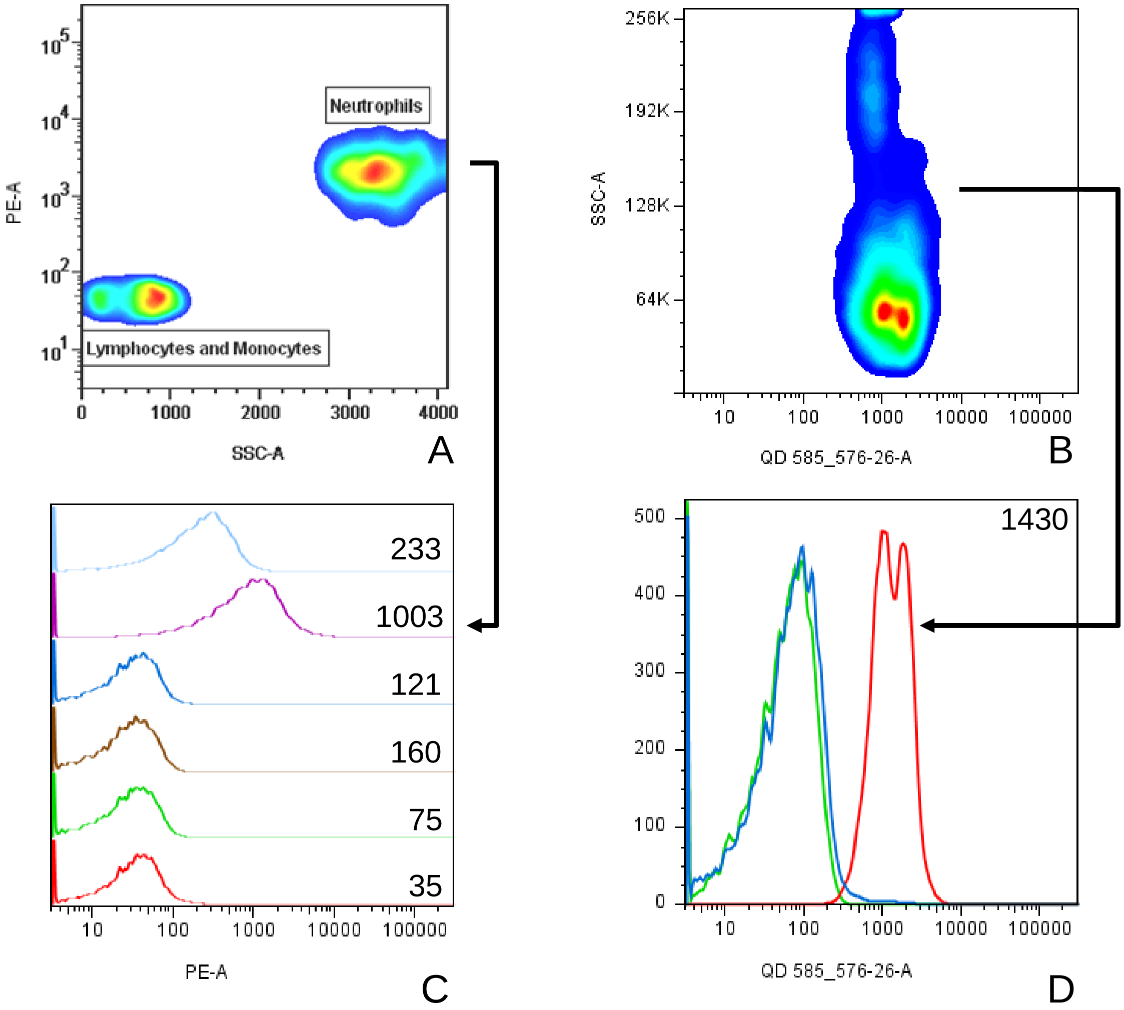

Figure 3. FACS analysis of leukocytes labeled with QD-mAb bioconjugates *in vitro*. (A) QD585-anti-RP-1 (Fc-blocked) specific labeling of neutrophils in peripheral blood. (B) QD585-anti-CD45 (Fc-blocked) labeling of all leukocyte subsets, with arrow B-D indicating fluorescence histogram of gated leukocytes (D). (C) Gated neutrophil populations from rat peripheral blood (arrow A-C shows a gated neutrophil population used for analysis of 1 sample), (488nm Ar laser excitation, Phycoerythrin (PE) emission filter (585/42nm)), with mean fluorescence intensity of each sample indicated in bold. Light Blue: PE-anti-RP-1 dye-labeled positive control mAb, Purple: QD585-anti-RP-1 (Fc-blocked), Blue: QD585 quenched with L-Cysteine, Brown: QD-Ms-IgG2a isotype non-Fc blocked, Green: QD-Ms-IgG2a isotype Fc blocked, Red: Unlabeled rat peripheral blood. (D) Rat leukocytes labeled with QD585-anti-CD45 (Red, gated leukocytes from (B)), QD585-Ms IgG1 Fc blocked isotype control (Blue), or unlabeled (Green).

In vivo Imaging

Intravenous injection of QD bioconjugates targeted to ICAM-1 or VCAM-1 resulted in a maximum increase in vascular fluorescence in streptozotocin (STZ)-treated diabetic rats within 30 and 90 minutes, respectively (**Figure 4**). This increase in fluorescence was observed in major vessels as well as the microcirculation. Control rat retinas did not exhibit the same fluorescence intensity with either the ICAM (**Figure 4A-C**) or VCAM (**Figure 4D-F**) conjugates. Injection of QD anti-PECAM produced increases in fluorescence which were similar in both STZ-treated and untreated animals (**Figure 4G-I**). Injection of QD-IgG1, a nonspecific control, did not result in fluorescence signal accumulation in the retinal vasculature to any appreciable degree throughout the duration of imaging up to 2.5 hrs (**Figure 4J-L**).

Intravenous injection of QD585-anti-RP-1 conjugates enabled the fluorescence detection and long-term tracking of neutrophils in STZ-treated diabetic animals as shown in **Figure 5A-D**. Using a pulsed xenon flashlamp, we visualized individual free flowing leukocytes (**Figure 5A-B**), leukocyte rolling along endothelial walls (**Figure 5C**), and leukostasis (**Figure 5D**) in major vessels as well as capillaries. Individual neutrophils were resolved in all vessels including arteries, and an increase in stagnant neutrophils in the microcirculation was observed in the STZ-treated group (5.83 ± 2.86, n = 6) vs. untreated animals (0.50 ± 0.55, n = 6) ($P < 0.01$). Fluorescence micrographs of stagnant neutrophils in flat-mounted STZ-treated rat retinas confirmed *in vivo* observations (**Figure 5G**).

Injection of the QD655-anti-CD45 bioconjugate in LPS-treated EIU rat models revealed a significant number of stagnant leukocytes in the microcirculation relative to

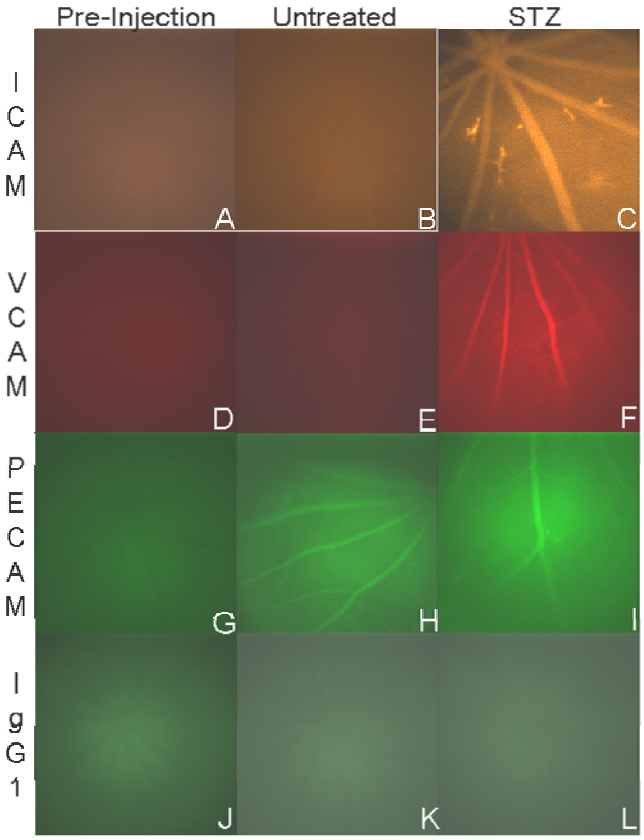

Figure 4. Representative frames from *in vivo* digital videos of STZ treated and untreated rat retinas. Pre-injection digital videos using the appropriate fluorescence filters for the spectrally-distinct biomarkers of interest (left column; A,D,G,J) were acquired prior to bioconjugate injection. QD585-anti-ICAM, QD655-anti-VCAM, QD525-anti-PECAM, and QD565-Ms IgG_1 were systemically injected in STZ-treated rats. Untreated control rat fundi (middle column; B,E,H,K) and STZ-treated rat fundi (right column; C,F,I,L) were imaged either 30 min (ICAM) or 90 min (VCAM, PECAM, IgG_1) post-injection under identical acquisition settings used for background autofluorescence measurements for each biomarker channel. Fluorescence enhancement due to target binding in untreated controls (B,E,H,K) was primarily observed for PECAM (H). The retinal vasculature of STZ-treated rats (C,F,I,L) showed a marked increase in fluorescence due to binding of QD-mAb conjugates to ICAM (C) and VCAM (F), with at least 5-fold increases in fluorescence intensity over background measured for labeled vasculature. Injection of conjugates to PECAM (I) produced similar levels of fluorescence under both conditions (H,I). Fluorescence signal from nonspecific IgG_1 mAb bioconjugates (J-L) was not detected in either control or STZ retinas. Images shown were acquired at imaging intervals resulting in optimal signal to noise ratio.

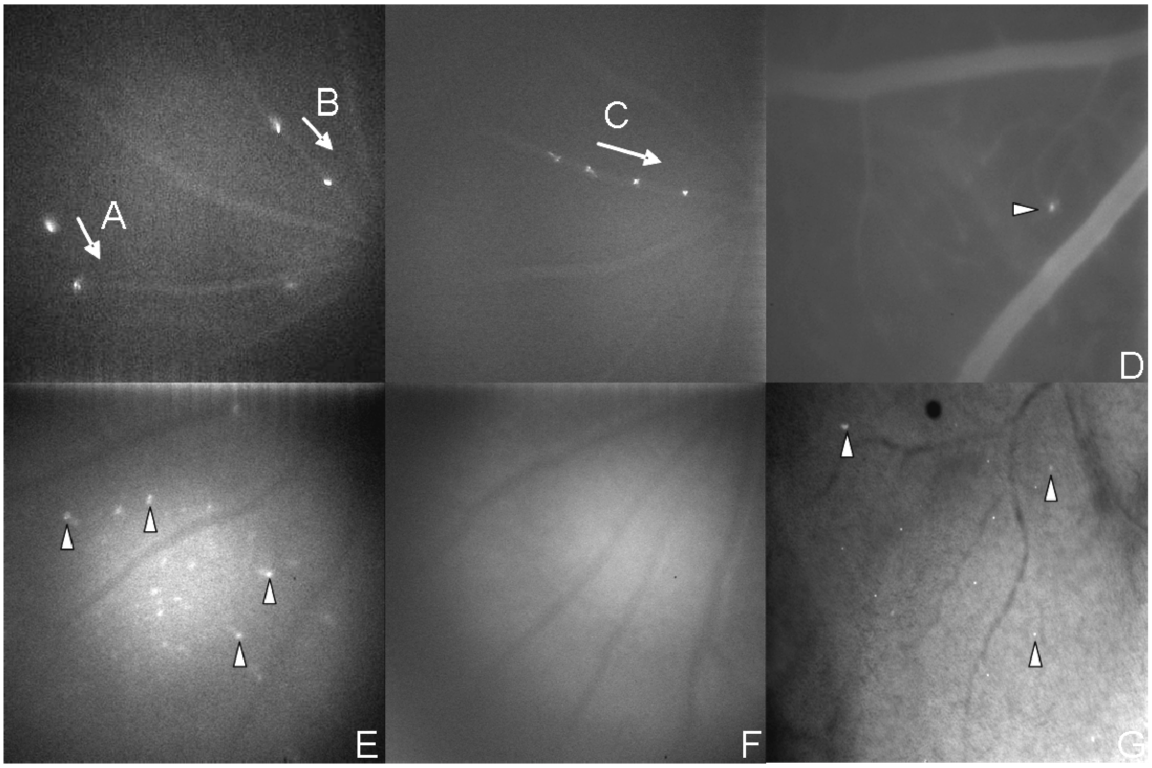

Figure 5. *In vivo* imaging of endogenously QD-mAb-labeled leukocyte trafficking in two rat models of inflammation. The CCD acquired images with exposure times ranging from 50 to 200ms with 110 ms between exposures. Flowing of QD585-RP-1 labeled cells in vessels (A-B) or leukocyte rolling (C) in STZ model as detected by two pulses of a xenon flashlamp at 50 ms intervals within 30 minutes of probe injection. Leukostasis was frequently observed in the STZ-treated rat model (D in right panel). Stagnant neutrophil appears as a hyperfluorescent dot in the microcirculation. Stagnant neutrophils were continuously visible in the retinal vasculature for over one hour of *in vivo* imaging. Stagnant leukocytes labeled *in vivo* with QD655-anti-CD45 were present at high densities in EIU rat models (E) relative to untreated controls (F). Stagnant neutrophils labeled in STZ-streated diabetic animals were visible in post-mortem retinal flat-mounts (G).

untreated animals (**Figure 5E-F**). The number of stagnant leukocytes in LPS-treated rat retinas (20.33 ± 8.73, n = 6) was elevated over control retinas (2.17 ± 1.17, n = 3) *in vivo* ($P < 0.01$).

Ten seconds after tail vein injection, comparison of the retinal fluorescence from Fc-shielded and non-Fc-shielded bioconjugates showed significantly less fluorescence from the non-shielded bioconjugate (**Figure 6**). Tracers injected intravenously into a tail vein travel through the hepatic circulation, heart and lungs before the remainder reaches the eye. Our data indicate that non Fc-blocked nonspecific QD-IgG$_1$ is cleared rapidly within 2 hours of circulation, returning retinal fluorescence levels to pre-injection values (**Figure 6E-H, J**). For Fc-blocked nonspecific QD-IgG$_1$, an apparent bolus is observed within 12 seconds of injection (**Figure 6B**), and fluorescence levels by 2 hours have not returned to background values (**Figure 6A-D, I**). These results suggest that Fc blockade substantially enhances the circulation lifetime of the QD-mAb due to reduced uptake and clearance.

Ex vivo imaging of retinal tissue

Immunofluorescence analysis of flat-mounted retinas showed correlation of *in vivo* features, such as enhanced CAM expression areas within the microcirculation, with *ex vivo* microscopy (**Figure 7A-B**). Analysis of post-mortem retinal tissue also indicated low nonspecific binding of Fc-shielded bioconjugates (**Figure 7C-D**) within blood vessels. The microcirculation in a flat mount from an EIU rat featured leukocyte adhesions and extravasations similar to those observed *in vivo* (not shown), and similar to the result shown for the STZ-treated rat (**Figure 5G**).

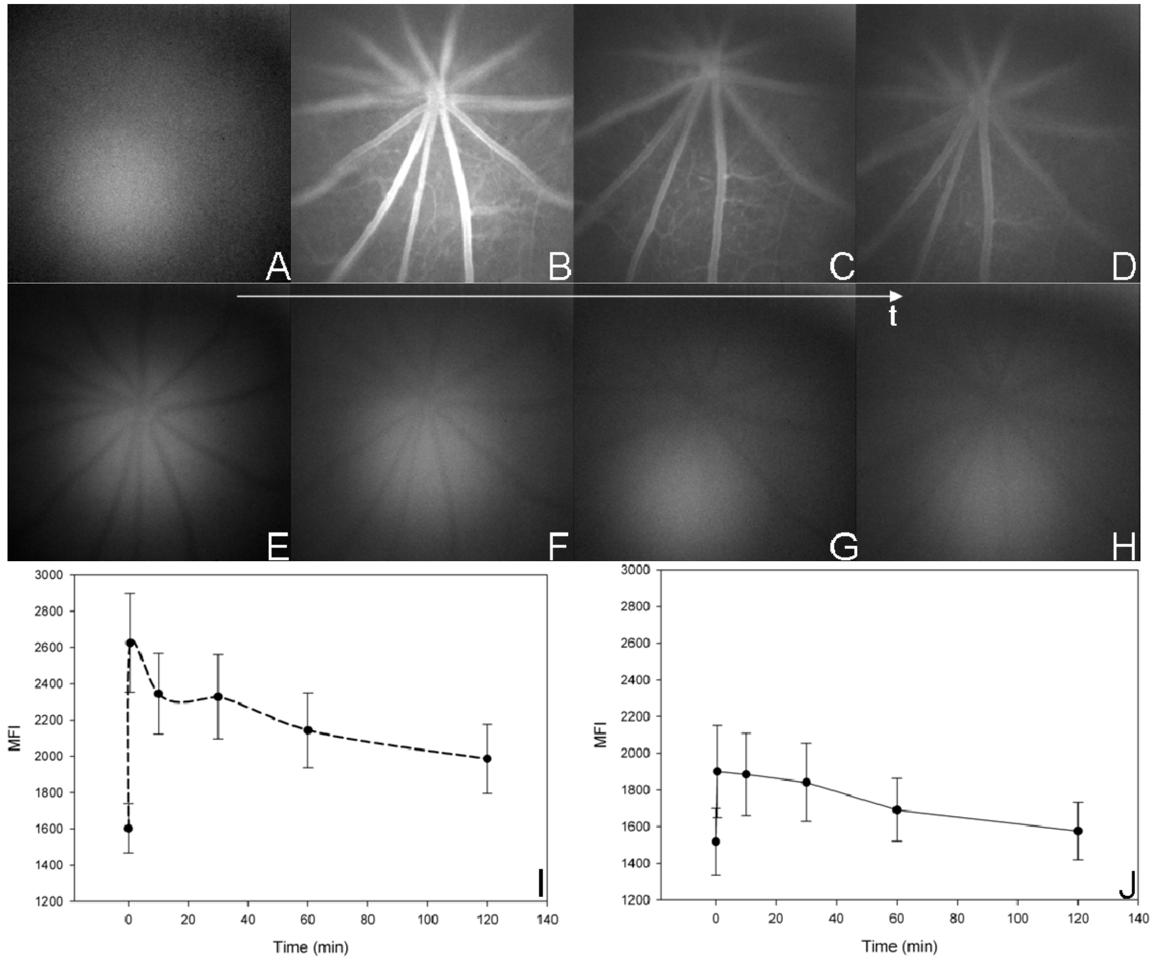

Figure 6. Comparison of Fc-blocked (A-D, I) and non Fc-blocked (E-H, J) QD-IgG$_1$ mAb bioconjugates *in vivo*. (A) Pre-injection autofluorescence in QD655 emission channel. (B-D) Fc-blocked QD655-IgG$_1$ in retina observed 12 s post-injection (B) where the first-pass of bolus through retinal circulation is observed, 1 hr. post-injection (C), and 2 hrs. post-injection, by which time Fc-blocked QD655-induced fluorescence is still above background levels as measured in (I, dashed line). (E) Autofluorescence levels in QD565 channel. (F-H) non Fc-blocked QD565-IgG$_1$ bolus was not qualitatively visible at 12 s post-injection (F), and subsequent image acquisitions at 1 hr (G) and 2 hr (H) revealed eventual return of image intensity to pre-injection levels (J, solid line), suggesting a relatively rapid clearance and/or uptake of non Fc-blocked QD-mAb.

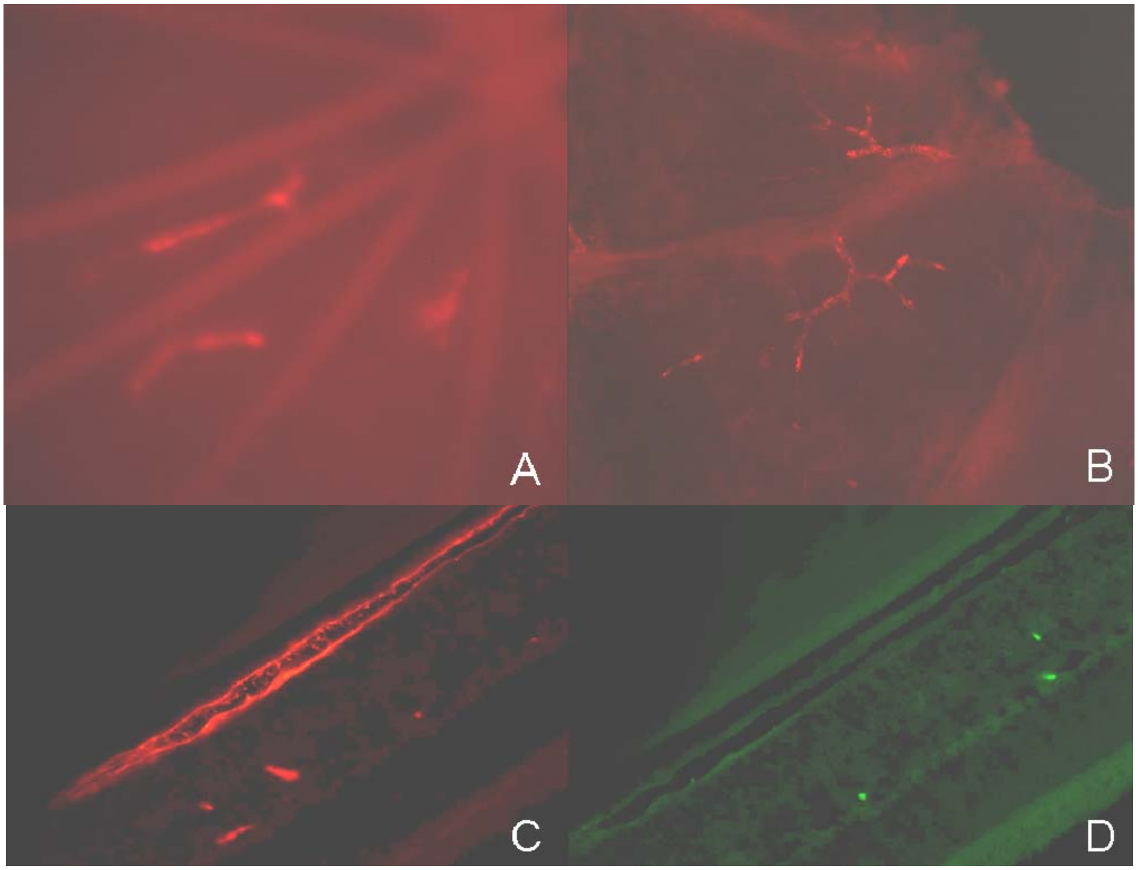

Figure 7. *In vivo* microcirculatory VCAM-1 expression (A), can be confirmed using immunofluorescence analysis post-mortem (B), as shown for QD655-anti-VCAM-1 labeled vasculature. While QD655-VCAM-1 (Fc-blocked) conjugates were shown to specifically stain vasculature in retinal histological sections (C), no background staining due to QD-IgG_1 (Fc-blocked) was observed above background autofluorescence levels (D).

Discussion

Fc-blocked QD-mAb were found to be specific for CAM and leukocyte targets, as shown by immunofluorescence (**Figure 1-2**), flow cytometry (**Figure 3**), and *in vivo* and *ex vivo* retinal imaging (**Figure 4-7**). QD-IgG that were nonspecific in reactivity did not bind to retinal vasculature (**Figure 6**), which suggests that Fc-blocked QD-antibody bioconjugates feature reduced nonspecific binding tendencies while retaining the native binding affinity conferred by the mAb. Our technique, employing PEGylation, 2-MEA reduction and Fc-blockade by Fc-specific $F(ab)_2$ is a rapid, cost-effective method for the site-specific bioconjugation and immune-shielding of mAb on nanoparticle surfaces. The 2-MEA reduction process was found to work equally well on mouse IgG_1 and IgG_{2a} subclasses using the same protocol. As an alternative to removal of the Fc fragment from the antibody, we choose instead to adsorb it with an antibody fragment which itself has no Fc region. Non-targeted QD-IgG conjugates adsorbed with an Fc-blocking $F(ab)_2$ were less susceptible to nonspecific binding to leukocyte and endothelial cell surfaces compared to the same conjugates without Fc-blockade (**Figure 1-3)**. This may be the result of steric inhibition conferred upon the bioconjugate by the $F(ab)_2$ which reduces Fc receptor access to its Fc fragment binding site on the IgG. Fc-blockade of CAM-targeted QD did not affect their binding affinities toward endothelial cell proteins *in vitro* or *in vivo* (**Figure 1-2, 4**). Fc-blockade by itself also may potentially enhance the circulation half-life of QD-mAb when employed in conjunction with PEG. Fc-blocked, non-targeted QD-IgG were present in the retinal circulation in much higher fluorescence levels relative than the same dose of non-Fc-blocked constructs (**Figure 6**), suggesting that Fc-blockade of IgG may substantially reduce first-pass nonspecific clearance of probes due to liver and spleen immunorecognition. Therefore, our probe design features target selectivity with a reduced tendency for nonspecific binding.

Analogues of our strategy exist for reduction of nonspecific binding of bioconjugates for *in vitro* applications, and we have applied these *in vitro* techniques for the first time to *in vivo* imaging. For example, the commercial reagent FcBlock (anti-CD16, anti-CD32, BD Biosciences) has long been utilized to functionally block Fc receptors on hematopoietic and endothelial cells prior to immunofluorescence (*34*) or flow cytometric (*35*) analysis for the reduction of background staining using cell surface protein antibodies. Direct blockade of the Fc *fragment* of antibodies rather than Fc receptors occurs often in biology. Blockade of the antibody Fc domain with streptococcal proteins has been found to reduce Fc-mediated nonspecific binding (*36*). Herpes Simplex Virus type 1 (HSV-1), when bound by an IgG, uses its Fcγ receptors to occupy the Fc fragment of the same IgG, thus preventing Fc-mediated immunodefensive mechanisms (*37*). By adsorption of the QD-IgG conjugate with an Fc-targeted $F(ab)_2$, it is likely that the adsorbed fragment makes the Fc binding site of the targeting antibody sufficiently inaccessible to immune surveillance, thus enhancing specificity and circulation time.

Other strategies to reduce Fc-mediated immune recognition of antibodies or antibody-based bioconjugates are reported in the literature. Specifically, antibody fragmentation techniques using papain, pepsin, or ficin require several reaction steps and much reagent quantity and time optimization for each antibody species and subclass, and generally do not yield a biomolecule with a site-specific crosslinking site suitable for nanoparticle conjugation. Instead, primary amines which reside in the antigen-binding site of the antibody could be crosslinked to the nanoparticle, obliterating its antigen binding affinity following bioconjugation. Protein engineering techniques now provide for a means of producing antibody fragments with engineered hinge region cysteines (Fab') which allow for site-specific nanoparticle conjugation while preserving the antigen-binding region (*38, 39*). However, this process is time-consuming and costly, and may not be suitable in applications where multiple IgGs are to be conjugated to nanoparticles for multiplexed imaging on a small scale, or where IgG targets are quickly examined and replaced for purposes of drug discovery or biology. Our process provides for the site-specific conjugation of antibodies to nanoparticles, without IgG subclass-specific optimization, with similar benefits of immune system evasion afforded by antibody fragmentation techniques.

Our *in vivo* imaging results are consistent with studies of ICAM and VCAM expression in diabetic and non-diabetic tissue, in which their upregulation is implicated in an inflammatory cascade that causes various complications of the disease (*6, 40, 41*). QD fluorescence due to ICAM and VCAM expression is apparent on major vessels as well as the microcirculation in disease models, which appears as an out of focus fluorescent background behind the major vessels (**Figure 4A-F**). QD targeted against PECAM, a panendothelial marker, produced increases in fluorescence which were similar in both STZ-treated and untreated animals (**Figure 4G-I**), thus suggesting its utility as an internal control or vascular counterstain in this imaging application. Our technique was found to be suitable for the long-term imaging of stagnant leukocytes commonly observed in both the STZ-treated rat model of diabetes (*6, 9*) and the LPS-treated rat model of EIU (*42*).

Photobleaching is a problem with current techniques which probe leukocyte dynamics *in vivo*, such as acridine orange fluorography (*43, 44*). Thus, long-term imaging of leukocytes is hindered. Using QD-based fluorography, we were able to continuously observe entrapped leukocytes in the circulation over an hour of continuous illumination without bleaching (**Figure 5**). Therefore, our QD-based imaging technique constitutes a potential alternative to current methods of imaging leukocytes due to the ability to simultaneously image multiple leukocyte subsets and stationary biomarkers with one excitation source with high specificity.

Our imaging technique provides non-invasive optical access to the *in vivo* retinal vasculature and continuous monitoring of vascular events. Spatial resolution on the order of a cell is achieved with this technique. QD have superior optical properties, such as high quantum efficiency and photostability, as well as distinct size-tunable emission wavelengths with the need for only one excitation source. By harnesseing these QD properties while immune-shielding the nanoparticle surface, it was readily possible to image three CAMs and one leukocyte subset within the same animal, without spectral overlap, using one blue excitation source to sufficiently illuminate QD-tagged species within the circulation. This feature enables detailed multiplexed studies of disease and biological processes. We used this approach to simultaneously observe the molecular expression of three different biomarkers, while also observing leukocyte-endothelial interactions. Other applications of this imaging strategy could readily be applied to studies in which multiple cellular and biomolecular vascular functions remain to be elucidated such as cancer, ocular angiogenesis, and atherosclerosis. While qualitative information was primarily presented in this initial application of our technique, we foresee the calculation of additional parameters including rolling velocities for various subtypes, relative fluorescence intensities of specific biomolecules along vascular walls, density of entrapped leukocytes, and important features of the inflammatory process *in vivo*.

Acknowledgements

We thank J.M. Higginbotham for assistance with flow cytometry, E.J. Dworska for assistance with tissue culture, and D.W. Piston for flash trigger equipment. This work was supported, in part, by grants from the National Institutes of Health (F.R. Haselton, PI, EY13451, EY017522), Vanderbilt University Discovery Grant Program, and Vanderbilt Vision Research Training Grant (J.D. Schall, PI, T32-EY07135-13).

References

(1) Kaneider, N. C., Leger, A. J., and Kuliopulos, A. (2006) Therapeutic targeting of molecules involved in leukocyte-endothelial cell interactions. *Febs J 273*, 4416-24.

(2) Cook-Mills, J. M., and Deem, T. L. (2005) Active participation of endothelial cells in inflammation. *J Leukoc Biol 77*, 487-95.

(3) Frieri, M. (2005) Asthma concepts in the new millennium: update in asthma pathophysiology. *Allergy Asthma Proc 26*, 83-8.

(4) Ulbrich, H., Eriksson, E. E., and Lindbom, L. (2003) Leukocyte and endothelial cell adhesion molecules as targets for therapeutic interventions in inflammatory disease. *Trends Pharmacol Sci 24*, 640-7.

(5) Wellen, K. E., and Hotamisligil, G. S. (2005) Inflammation, stress, and diabetes. *J Clin Invest 115*, 1111-9.

(6) Joussen, A. M., Poulaki, V., Le, M. L., Koizumi, K., Esser, C., Janicki, H., Schraermeyer, U., Kociok, N., Fauser, S., Kirchhof, B., Kern, T. S., and Adamis, A. P. (2004) A central role for inflammation in the pathogenesis of diabetic retinopathy. *Faseb Journal 18*, -.

(7) Miyamoto, K., Khosrof, S., Bursell, S. E., Rohan, R., Murata, T., Clermont, A. C., Aiello, L. P., Ogura, Y., and Adamis, A. P. (1999) Prevention of leukostasis and vascular leakage in streptozotocin-induced diabetic retinopathy via intercellular adhesion molecule-1 inhibition. *Proceedings of the National Academy of Sciences of the United States of America 96*, 10836-10841.

(8) Gotoh, R., Suzuki, J., Kosuge, H., Kakuta, T., Sakamoto, S., Yoshida, M., and Isobe, M. (2004) E-selectin blockade decreases adventitial inflammation and attenuates intimal hyperplasia in rat carotid arteries after balloon injury. *Arteriosclerosis Thrombosis and Vascular Biology 24*, 2063-2068.

(9) Barouch, F. C., Miyamoto, K., Allport, J. R., Fujita, K., Bursell, S. E., Aiello, L. P., Luscinskas, F. W., and Adamis, A. P. (2000) Integrin-mediated neutrophil adhesion and retinal leukostasis in diabetes. *Investigative Ophthalmology & Visual Science 41*, 1153-1158.

(10) Baez, S. (1973) An open cremaster muscle preparation for the study of blood vessels by in vivo microscopy. *Microvasc Res 5*, 384-94.

(11) Conway, R. S., Factor, S. M., Sonnenblick, E. H., and Baez, S. (1987) Microvascular reactivity of the myopathic Syrian hamster cremaster muscle. *Cardiovasc Res 21*, 796-803.

(12) Nishiwaki, H., Ogura, Y., Kimura, H., Kiryu, J., and Honda, Y. (1995) Quantitative evaluation of leukocyte dynamics in retinal microcirculation. *Invest Ophthalmol Vis Sci 36*.

(13) Nishiwaki, H., Ogura, Y., Kimura, H., Kiryu, J., Miyamoto, K., and Matsuda, N. (1996) Visualization and quantitative analysis of leukocyte dynamics in retinal microcirculation of rats. *Invest Ophthalmol Vis Sci 37*.

(14) Tsujikawa, A., Kiryu, J., Nonaka, A., Yamashiro, K., Nishiwaki, H., Honda, Y., and Ogura, Y. (2000) Leukocyte-endothelial cell interactions in diabetic retina after transient retinal ischemia. *Am J Physiol Regul Integr Comp Physiol 279*.

(15) McHale, J. F., Harari, O. A., Marshall, D., and Haskard, D. O. (1999) Vascular endothelial cell expression of ICAM-1 and VCAM-1 at the onset of eliciting contact hypersensitivity in mice: evidence for a dominant role of TNF-alpha. *J Immunol 162*, 1648-55.

(16) Ivan, E., and Colovai, A. I. (2006) Human Fc receptors: Critical targets in the treatment of autoimmune diseases and transplant rejections. *Human Immunology 67*, 479-491.

(17) Berry, C., and Curtis, A. (2003) Functionalisation of magnetic nanoparticles for applications in biomedicine. *JOURNAL OF PHYSICS D-APPLIED PHYSICS 36*, R198-R206.

(18) Gao, X., Yang, L., Petros, J. A., Marshall, F. F., Simons, J. W., and Nie, S. (2005) In vivo molecular and cellular imaging with quantum dots. *Curr Opin Biotechnol 16*, 63-72.

(19) Smith, A. M., Gao, X., and Nie, S. (2004) Quantum dot nanocrystals for in vivo molecular and cellular imaging. *Photochem Photobiol 80*, 377-85.

(20) Ballou, B., Lagerholm, B. C., Ernst, L. A., Bruchez, M. P., and Waggoner, A. S. (2004) Noninvasive imaging of quantum dots in mice. *Bioconjug Chem 15*, 79-86.

(21) Bentzen, E. L., Tomlinson, I. D., Mason, J., Gresch, P., Warnement, M. R., Wright, D., Sanders-Bush, E., Blakely, R., and Rosenthal, S. J. (2005) Surface modification to reduce nonspecific binding of quantum dots in live cell assays. *Bioconjug Chem 16*, 1488-94.

(22) Dubertret, B., Skourides, P., Norris, D. J., Noireaux, V., Brivanlou, A. H., and Libchaber, A. (2002) In vivo imaging of quantum dots encapsulated in phospholipid micelles. *Science 298*, 1759-62.

(23) Akerman, M. E., Chan, W. C., Laakkonen, P., Bhatia, S. N., and Ruoslahti, E. (2002) Nanocrystal targeting in vivo. *Proc Natl Acad Sci U S A 99*, 12617-21.

(24) Gao, X. H., Cui, Y. Y., Levenson, R. M., Chung, L. W. K., and Nie, S. M. (2004) In vivo cancer targeting and imaging with semiconductor quantum dots. *Nature Biotechnology 22*, 969-976.

(25) Russ, P. K., Gaylord, G. M., and Haselton, F. R. (2001) Retinal vascular permeability determined by dual-tracer fluorescence angiography. *Ann Biomed Eng 29*, 638-47.

(26) Gotoh, S., Itoh, M., Fujii, Y., Arai, S., and Sendo, F. (1986) Enhancement of the Expression of a Rat Neutrophil-Specific Cell-Surface Antigen by Activation with Phorbol-Myristate Acetate and Concanavalin-A. *Journal of Immunology 137*, 643-650.

(27) Karyakin, A. A., Presnova, G. V., Rubtsova, M. Y., and Egorov, A. M. (2000) Oriented immobilization of antibodies onto the gold surfaces via their native thiol groups. *Anal Chem 72*, 3805-11.

(28) Yoshitake, S., Yamada, Y., Ishikawa, E., and Masseyeff, R. (1979) Conjugation of glucose oxidase from Aspergillus niger and rabbit antibodies using N-hydroxysuccinimide ester of N-(4-carboxycyclohexylmethyl)-maleimide. *Eur J Biochem 101*, 395-9.

(29) Li, W., and Chung, S. C. (2003) Flow cytometric evaluation of leukocyte function in rat whole blood. *In Vitro Cell Dev Biol Anim 39*, 413-9.

(30) Barouch, F. C., Miyamoto, K., Allport, J. R., Fujita, K., Bursell, S. E., Aiello, L. P., Luscinskas, F. W., and Adamis, A. P. (2000) Integrin-mediated neutrophil adhesion and retinal leukostasis in diabetes. *Invest Ophthalmol Vis Sci 41*, 1153-8.

(31) Romer, L. H., McLean, N. V., Yan, H. C., Daise, M., Sun, J., and DeLisser, H. M. (1995) IFN-gamma and TNF-alpha induce redistribution of PECAM-1 (CD31) on human endothelial cells. *J Immunol 154*, 6582-92.

(32) Zou, Y., Yoon, S., Jung, K. J., Kim, C. H., Son, T. G., Kim, M. S., Kim, Y. J., Lee, J., Yu, B. P., and Chung, H. Y. (2006) Upregulation of aortic adhesion molecules during aging. *J Gerontol A Biol Sci Med Sci 61*, 232-44.

(33) Pan, L. F., Kreisle, R. A., and Shi, Y. D. (1998) Detection of Fcgamma receptors on human endothelial cells stimulated with cytokines tumour necrosis factor-

alpha (TNF-alpha) and interferon-gamma (IFN-gamma). *Clin Exp Immunol 112*, 533-8.

(34) Llodra, J., Angeli, V., Liu, J. H., Trogan, E., Fisher, E. A., and Randolph, G. J. (2004) Emigration of monocyte-derived cells from atherosclerotic lesions characterizes regressive, but not progressive, plaques. *Proceedings of the National Academy of Sciences of the United States of America 101*, 11779-11784.

(35) Flano, E., Husain, S. M., Sample, J. T., Woodland, D. L., and Blackman, M. A. (2000) Latent murine gamma-herpesvirus infection is established in activated B cells, dendritic cells, and macrophages. *Journal of Immunology 165*, 1074-1081.

(36) Woof, J. M. (2002) The human IgA-Fc alpha receptor interaction and its blockade by streptococcal IgA-binding proteins. *Biochem Soc Trans 30*, 491-4.

(37) Lin, X. Q., Lubinski, J. A., and Friedman, H. M. (2004) Immunization strategies to block the herpes simplex virus type 1 immunoglobulin G Fc receptor. *Journal of Virology 78*, 2562-2571.

(38) Chapman, A. P. (2002) PEGylated antibodies and antibody fragments for improved therapy: a review. *Adv Drug Deliv Rev 54*, 531-45.

(39) Filpula, D. (2007) Antibody engineering and modification technologies. *Biomol Eng 24*, 201-15.

(40) Meleth, A. D., Agron, E., Chan, C. C., Reed, G. F., Arora, K., Byrnes, G., Csaky, K. G., Ferris, F. L., and Chew, E. Y. (2005) Serum inflammatory markers in diabetic retinopathy. *Investigative Ophthalmology & Visual Science 46*, 4295-4301.

(41) Ludwig, R., Kretschmer, M., Caspar, G., Bojunga, J., Oldenburg, A., Schumm-Draeger, P., Stegmuller, M., Von Minckwitz, G., Usadel, K. H., and Kusterer, K. (1999) In vivo microscopy of murine islets of Langerhans: increased adhesion of transferred lymphocytes to islets depends on macrophage-derived cytokines in a model of organ-specific insulitis. *Immunology 98*, 111-115.

(42) Rosenbaum, J. T., McDevitt, H. O., Guss, R. B., and Egbert, P. R. (1980) Endotoxin-induced uveitis in rats as a model for human disease. *Nature 286*, 611-3.

(43) Hossain, P. (1999) Scanning laser ophthalmoscopy and fundus fluorescent leucocyte angiography. *Br J Ophthalmol 83*, 1250-3.

(44) Kimura, H., Kiryu, J., Nishiwaki, H., and Ogura, Y. (1995) A new fluorescent imaging procedure in vivo for evaluation of the retinal microcirculation in rats. *Curr Eye Res 14*, 223-8.

CHAPTER IV

QUANTUM DOT-MEDIATED IMAGING OF ATHEROSCLEROSIS

Ashwath Jayagopal[1]
Yan Ru Su[2]
John L. Blakemore[2]
MacRae F. Linton[2]
Sergio Fazio[2]
Frederick R. Haselton[1]

[1]Department of Biomedical Engineering, Vanderbilt University
[2]Department of Medicine, Vanderbilt University School of Medicine
Nashville, Tennessee

This manuscript was submitted to the *Journal of Lipid Research* in April 2008.

Abstract

The progression of atherosclerosis has been associated with leukocyte infiltration within lesions. We describe a technique for the *ex vivo* imaging of cellular recruitment in atherogenesis which utilizes quantum dots (QD) to color-code different cell types within lesion areas. Spectrally-distinct QD were coated with the cell-penetrating peptide maurocalcine to cytoplasmically-label immunomagnetically-isolated monocytes and T lymphocytes. QD-maurocalcine bioconjugates labeled both cell types with high efficiencies, preserved cell viability, and did not perturb native monocyte adhesion to inflamed endothelium *in vitro*. QD-labeled cells were reinfused in ApoE -/- mice and age-matched controls for up to 4 weeks to investigate the incorporation of cells within aortic lesion areas, as determined by oil Red O (ORO) and immunofluorescence staining *ex vivo*. QD-labeled cells were visible in atherosclerotic plaques within 2 days of injection. Reinfused monocytes colocalized with CD68 immunofluorescence staining, whereas T lymphocytes were observed in distinct regions. Both cell types colocalized with areas of subsequent ORO staining. Our method for tracking leukocytes in lesions enables high signal to noise ratio imaging of multiple cell types and biomarkers simultaneously within the same specimen. It also has great utility in monitoring the role of circulating leukocytes in plaque development and progression.

Introduction

Atherosclerosis is a complex disease exacerbated by multiple cellular and molecular participants. A key contributor toward atherogenesis is the dysfunction of vascular endothelium, which presents molecular cues promoting leukocyte infiltration into arterial intima (1). Leukocytes which localize within atherosclerotic plaques include monocytes (2, 3), and lymphocytes, primarily of the CD4+ subset (4, 5). Monocytes migrate toward lesions and accumulate lipids in a process that transforms them into macrophage foam cells (6). These lipid-laden macrophages secrete reactive oxygen species and proteinases which induce a positive-feedback monocyte recruitment cascade, eventually leading to plaque instability and rupture (7). Lymphocytes also contribute to the progression of atherosclerosis *via* the secretion of the proinflammatory cytokine interferon gamma (IFN-γ), which has various roles in contributing to leukocyte recruitment to plaques and eventual plaque instability (4, 8-10). Other cell types, such as neutrophils (11) and dendritic cells (12, 13), also play a role in potentiating atherosclerotic complications *via* their activation proximal to inflammatory plaque surfaces. Therefore, techniques to visualize the spatial and temporal dynamics of these cellular mediators are needed to understand their role in the different stages of atherosclerosis.

Advances in the pathobiology of atherosclerosis have identified a number of key cellular and molecular mediators involved in early and late stages of disease (14, 15). Furthermore, innovations in both imaging instrumentation and *in vivo* imaging reagents complement these therapeutic and diagnostic targets for developing strategies to visualize vascular disease *in vivo* (16, 17). Macrophages in lesions have been imaged *in vivo* using magnetic resonance imaging (18, 19), optical imaging (20, 21), and positron emission tomography (22), by either intracellular targeting or cell surface biomarker targeting. Recently, we investigated a strategy for the color-coding of circulating leukocytes and cell surface biomolecules with fluorescing semiconducting nanocrystals, or quantum dots (QD), for multiplexed *in vivo* vascular imaging in rodent models of diabetic and ocular inflammation (23). The size-tunable emission spectra of QD enable the simultaneous *in vivo* and *ex vivo* tracking of multiple cells and biomarkers within the vasculature of the same animal with only one excitation source. Furthermore, QD are amenable to bioconjugation of ligands for cell targeting, and feature high quantum yields and photostability for long-term imaging applications (24, 25).

In this report, we demonstrate the utility of a method for applying the optical properties of QD for *ex vivo* imaging of atherosclerotic cellular components. The technique uses QD coated with the cell penetrating peptide maurocalcine (26) to fluorescently-label cytoplasmic compartments of lymphocytes and monocytes with different emission wavelengths so they can be simultaneously-detected in tissue. This approach was used to visualize leukocyte subtype recruitment to aortic valve leaflet lesions in an ApoE -/- mouse model of atherosclerosis (27), and has important implications for the multiplexed imaging of cells and biomolecules in vascular disease *in vivo*.

Methods

Immunomagnetic isolation of leukocytes

All animal procedures were approved by the Instituional Animal Care and Use Committee at Vanderbilt University. Spleens from wild-type and ApoE -/- mice aged from 7 months to 1 year were collected in RPMI 1640 supplemented with 10% fetal bovine serum (FBS) and 1% streptomycin-Fungizone. Splenocytes were prepared by disrupting the spleen with a syringe plunger on a nylon mesh filter. Collected cells were washed once in RPMI medium. Lymphocytes were isolated using Lympholyte M density gradient medium (Cedarlane Laboratories, Burlington, NC) according to manufacturer's instructions. Monocytes and T lymphocytes were isolated using anti-CD11b-coated paramagnetic microbeads (Miltenyi Biotec, Auburn, CA, # 130-049-601) and biotin-anti-T cell receptor antibody- (TCR β chain, BD Biosciences, San Jose, CA) coated paramagnetic microbeads (Miltenyi Biotec # 130-091-256) for monocytes and T lymphocytes, respectively. Each population was tested for purity by flow cytometry. In all cases (n = 4) the purity was >90%. Data was analyzed using FlowJo 7.2 (Treestar Software, Ashland, OR) and a FACSCalibur flow cytometer (BD Biosciences).

Quantum dot-labeling of leukocytes

QD coated with 6-8 streptavidins/nanoparticle emitting at 585 nm and 655 nm (QD585 and QD655) were purchased from Invitrogen Corporation (Carlsbad, CA). Biotinylated maurocalcine peptide was synthesized by Biomatik Corporation according to previously-published protocols (26). A 35-fold molar excess of peptide was mixed with 1 molar equivalent of QD585 or QD655 in 100 mM PBS, pH = 7.4, for 30 min. at room temperature. QD-maurocalcine was then separated from excess peptide using size-exclusion chromatography over a Superdex 200 column according to manufacturer instructions (GE Healthcare, UK). Elution fractions were measured using a BioTek Synergy HT microplate spectrophotometer (BioTek, Vermont, USA) configured for QD fluorescence at 585 nm or 655 nm, and peptide fluorescence as measured by fluorescamine assay (Sigma Chemical, St. Louis, MO). This process typically yielded QD with 12-17 peptides per nanocrystal.

For each cell labeling experiment, 1 X 10^6 cells/mL were stained with 100 nM QD-maurocalcine in PBS, pH = 7.4, at 37°C for 30 min. Cells were rinsed with PBS *via* centrifugation at 200 X *g* for 10 min. Cell viability and labeling efficiency were determined by the LIVE/DEAD single color fixable green kit according to manufacturer instructions (Invitrogen) on a FACSCalibur flow cytometer. Unlabeled cells subjected to the same rinsing and centrifugation steps served as controls.

Monocyte adhesion assay

bEnd.3 mouse endothelium was a gift from Dr. Jack Virostko. Cells were cultured in DMEM supplemented with 10% fetal bovine serum to confluency on 24-well tissue culture grade microplates. Cells were then treated with 500 ng/mL *Salmonella Typhimurium* lipopolysaccharide (LPS, Sigma) or untreated in complete media overnight. Monocytes (1 X 10^6 cells/mL) were incubated with 1 μM calcein-AM (Invitrogen) for 30 min. 100,000 monocytes of this suspension were either incubated in PBS or PBS containing 100 nM QD-maurocalcine for 30 min at 37°C. After rinsing with PBS, cells were plated onto LPS-stimulated or unreated bEnd.3 monolayers and incubated for 1 hr. at 37°C. At the end of the experiment, monolayers were rinsed three times with PBS to remove non-adherent cells, and the microplate was measured for calcein-AM fluorescence (490 nm excitation/525 nm emission). Results were compared by *t*-test and plotted using Sigmaplot 9 (SYSTAT, San Jose, CA).

Analysis of QD-labeled leukocytes in ApoE -/- mouse aorta

ApoE -/- and wild-type mice ranging from 7 months to 1 year were injected with 1 X 10^6 QD-maurocalcine-labeled monocytes or T lymphocytes *via* the retroorbital route. Animals were euthanized 2, 3, 5, and 28 days post-injection, and proximal aorta and whole aorta were harvested and sectioned as described previously (28). 5 μm frozen sections were stained for immunofluorescence with Alexa Fluor 488-conjugated anti-CD68 and mounted in VECTASHIELD with DAPI (Vector Laboratories, Burlingame, CA). Sections were analyzed by fluorescence microscopy on a Nikon TE2000U Eclipse inverted microscope (Nikon Instruments, Melville, NY) using DAPI, Alexa Fluor 488, QD585, and QD655 cubes in conjunction with a Hamamatsu C7780 cooled CCD camera (Hamamatsu Corp., Bridgewater, NJ). Image analysis was conducted using Image Pro Plus 5.1 (Media Cybernetics, Bethesda, MD).

Ex vivo imaging

En face aortas from ApoE -/- and wild-type mice were imaged for QD fluorescence using an IVIS 200 fluorescence imaging system configured for spectrally-distinct detection of QD585 and QD655 using bandpass emission filters (Caliper Life

Sciences, Hopkinton, MA). Following QD imaging, aortas were stained with Oil Red O and the percentage of atherosclerotic lesions (ORO positive area) was quantified in using a previously described technique (29). The IVIS 200 was then used to image ORO-stained areas via analysis of dye-induced near-infrared fluorescence (30, 31) with QD fluorescence subtracted from the image. ORO-stained lesions were pseudocolored so that areas of QD585-lymphocytes, QD655-monocytes, and ORO could be colocalized within the same tissue.

Results

Loading of leukocytes with QD-maurocalcine bioconjugates

The attachment of maurocalcine cell penetration peptides to QD enabled their highly-efficient loading into T lymphocytes and monocytes *ex vivo*, with no appreciable effects on cell viability and function. Immunomagnetic isolation procedures using anti-TCR and anti-CD11b beads yielded distinct T lymphocyte or monocyte subpopulations as demonstrated by double-staining experiments (**Figure 1A**). Labeling of these populations separately with QD585-maurocalcine and QD655-maurocalcine was more efficient than labeling with QD alone (**Figure 1B-C**).

Flow cytometric viability assays did not reveal substantial differences in cell viability between populations incubated with QD-maurocalcine or unlabeled populations, for either cell type (**Figure 2A**). Furthermore, monocytes labeled with QD homed to LPS-stimulated bEnd.3 mouse endothelium at a comparable rate to monocytes loaded only with C-AM dye (**Figure 2B**).

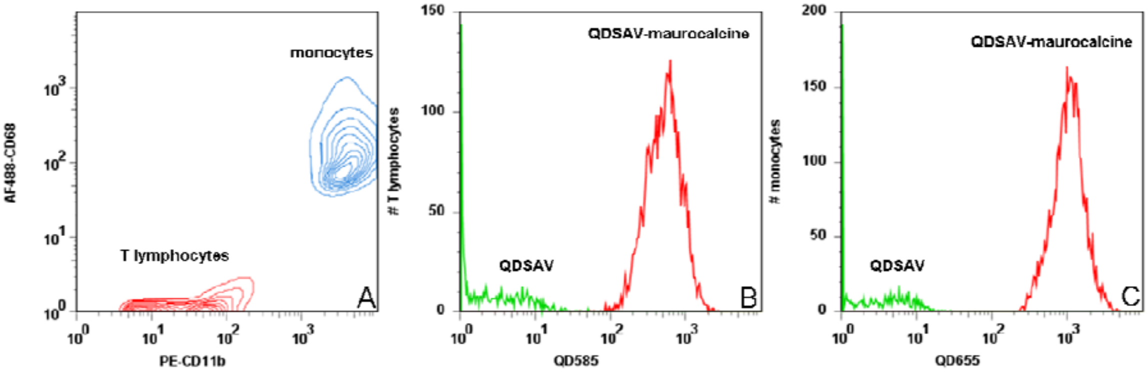

Figure 1. FACS analysis of CD11b and TCR-biotin immunomagnetically-purified leukocyte subsets (A), and QD-maurocalcine labeling of T lymphocytes with QD585 (B) and monocytes with QD655 (C). (A) Immunomagnetic purification yields two distinct populations, a CD11b$^+$/CD68$^+$ population, and a CD11b$^+$/CD68$^-$ population. T lymphocytes express low levels of CD11b and expression of CD68 is absent, whereas monocytes express both markers at relatively higher levels. (B-C) Both leukocyte subsets efficiently-internalize QD-maurocalcine (red) while excluding QD without peptide (green).

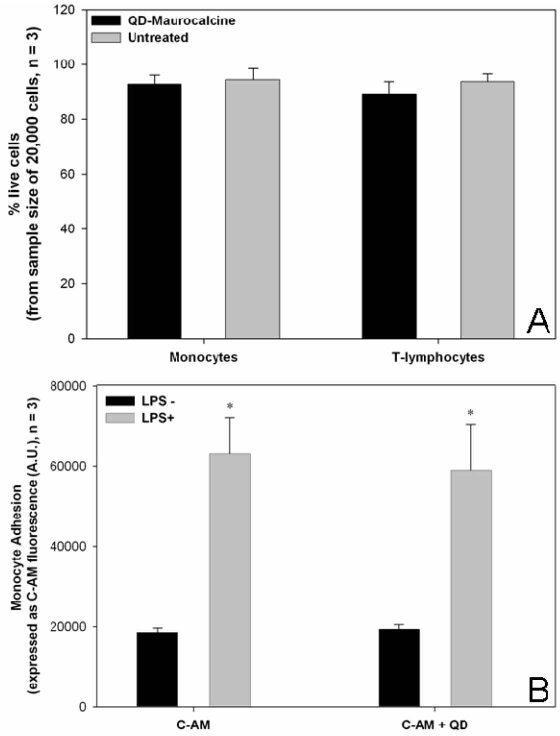

Figure 2. Cell viability analysis (A) and monocyte adhesion assay on bEnd.3 mouse endothelial monolayers *in vitro* (B). *- $P < 0.05$, n = 3.

Localization of QD-labeled leukocyte subsets in atherosclerotic lesions

QD-labeled monocytes were observed in atherosclerotic lesions as early as two days post-injection and as late as four weeks (latest time point observed) in ApoE -/- mice. **Figure 3** shows QD-labeled monocytes within aortic root lesions of 7 month (**Figure 3A-D**) and one year old (**Figure 3E-H**) ApoE -/- mice, and their colocalization with CD68-positive cells and the nuclear stain DAPI. In both mice, infused monocytes appeared to have infiltrated squamous endothelium to reside in deep regions of the lesion, where other, presumably pre-existing macrophages were present. However, the extent of accumulation of both resident and *ex vivo* reinfused monocytes/macrophages in early lesions was noticeably lower than the extent of accumulation in 1 yr. old ApoE -/- mouse lesions. Observations of lesions from mice of similar age were consistent with our finding that monocyte accumulation in lesions was proportional to the extent of lesion progression as determined by size and ORO staining. Lesions from mice not injected with QD-labeled cells or not labeled with CD68 did not exhibit appreciable autofluorescence.

QD-labeled T lymphocytes were observed in ApoE -/- mice aortic lesions as early as two days and as late as four weeks (latest timepoint tested) post-injection of cells. **Figure 4** shows fluorescence micrographs of lesions from the youngest animals (7 months) and the oldest animals (1 year) tested. A stark contrast in cellular accumulation between the two age groups was evident with both QD and immunofluorescence labeling methods. T lymphocytes appeared in regions of plaques either adjacent to resident macrophages or distinct from macrophages. QD585-labeled cells were detected in either

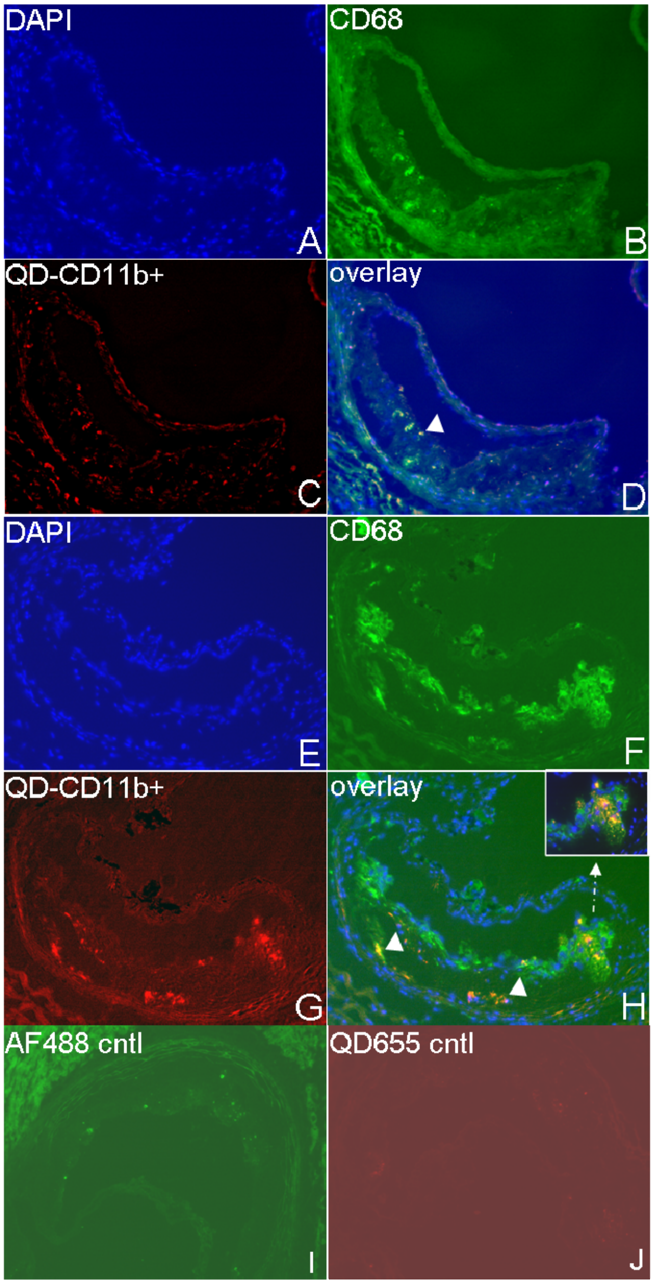

Figure 3. Representative fluorescence micrographs of QD-labeled monocyte accumulation in aortic root tissue lesion of 7 month old (A-D) and 12 month old (E-H) ApoE -/- mice, 5 days post-injection of 1 X 10^6 QD655-labeled monocytes. (D, H) Areas of colocalization between QD-labeled monocytes and Alexa Fluor 488-anti-CD68 are indicated with arrowheads (Magnification 50X). Inset in (H) shows magnified region (100X) showing increased colocalization of infused monocytes with resident macrophages.

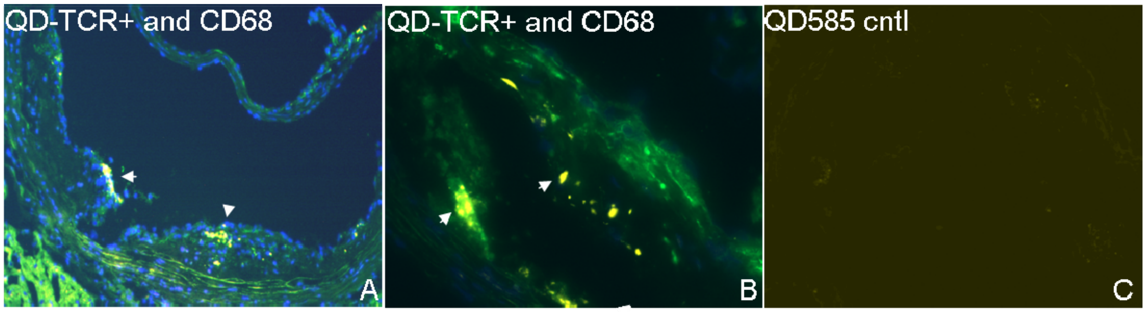

Figure 4. Fluorescence micrographs of QD-labeled T lymphocyte recruitment to aortic root lesions. (A) Arrowheads indicate regions of cellular infiltration (yellow). Magnification 50X. (B) Arrowheads indicate lymphocytes in regions colocalized with CD68 (green), or in distinct areas.

deep regions of lesions as small clusters (~5-8 cells) of lymphocytes in CD68-rich areas (**Figure 4A**), or areas of low CD68 expression near smooth muscle cells (**Figure 4B**).

The time allotted for QD-labeled leukocyte circulation post-injection did not affect relative levels of leukocyte accumulation in lesions, as 4 week post-injection timepoints featured similar accumulation of leukocytes as 2-5 day post-injection age-matched animals (not shown). Generally, QD was not observed to fade within the coverslipped specimen within a month following sample preparation, nor did extended circulation time of QD-labeled cells adversely affect photostability and photointensity of QD within lesions. Lesion autofluorescence in the QD585 channel was negligible.

Correlation of leukocyte accumulation with ORO staining by en face analysis

Macroscopic fluorescence imaging of *en face* preparations of mouse aortas revealed QD585 and QD655 accumulation in ORO-stained lipid regions throughout the aortic stem (**Figure 5**). No cells were observed in wild-type aortas, indicating that QD-labeled cells homed specifically to lesions. Furthermore, QD fluorescence was proportional to lesion surface area as determined by ORO-positive staining. The near infrared fluorescence spectra of ORO did not overlap with that of QD655 and QD585, due to the use of distinct bandpass emission filters and the serial nature of sample preparation, whereby QD images were acquired prior to ORO staining to allow for digital image background correction.

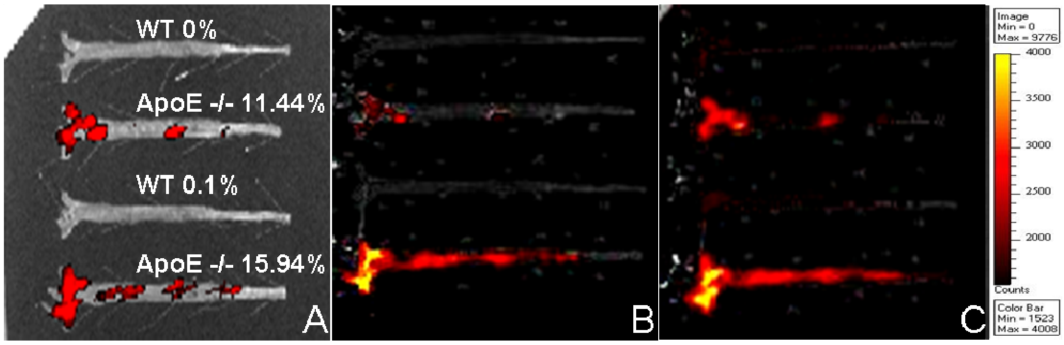

Figure 5. *Ex vivo* imaging of *en face* aorta preparations using macroscopic fluorescence imaging of ORO (A), QD585-T lymphocytes (B), and QD655-monocytes (C).

Discussion

QD are versatile reagents for imaging disease in preclinical models, due to the flexibility of ligands (nucleic acids, antibodies, peptides) they can accommodate, high photostability and emission intensity, and size-tunable emission wavelengths, and imaging of multiple QD within tissue requires only one excitation wavelength (32). QD have been loaded into (cytoplasm) or onto (cell surface) multiple cell types for imaging of dynamic processes *in vivo*, including tracking of cancer metastasis (33) and leukocyte-endothelial interactions during inflammatory vascular disease (23). The multispectral imaging capabilities enabled by QD make them attractive reagents for visualizing dynamic processes consisting of multiple cellular and biomolecular mediators *in vivo*.

In this work, we have adapted QD for monitoring atherogenesis in ApoE -/- mouse models *ex vivo*, with particular attention given to the potential utility of this approach for *in vivo* imaging of cellular accumulation within atheroma. Furthermore, leukocytes capable of homing to lesions, namely monocytes, which differentiate into macrophages within the lesion, can be genetically-engineered to induce regression of lesions (34). Therefore, a technique to monitor their biodistribution *in vivo* and *ex vivo* is particularly desirable. Flow cytometric analysis indicate that QD-maurocalcine bioconjugates were internalized efficiently within leukocyte subtypes (**Figures 1B-C**), with no significant effects on cell viability (**Figure 2A**) and homing to inflammatory endothelium (**Figure 2B**) observed. These *in vitro* studies collectively indicate that QD are at least on the short term suitable for studies of leukocyte function in vascular disease. Homing of both cell types to lesions were observed (**Figures 3-4**), with varying degrees of penetration and colocalization with resident macrophages. Therefore, QD may be a useful tool to study differential localization on a spatial or temporal scale for several cell types within the same tissue. The multiplexing capability afforded by the use of spectrally-distinct QD makes the simultaneous detection of multiple cell types a possibility, even with the use of conventional immuno-fluorescence markers, in this case Alexa Fluor 488 anti-CD68 and the nuclear stain DAPI, without spectral bleed-through. Although organic dyes were used in conjunction with QD-labeled cells in this application, QD-antibody conjugates could be substituted in order to multiplex immunofluorescence analysis as well.

Macroscopic imaging of QD within *en face* aorta preparations indicate both the specificity of QD-labeled leukocytes toward lesions, as well as the high signal to noise ratio of QD in tissue (**Figure 5B-C**). We selected QD configured for emission above green (< 540 nm) wavelengths for this study, due to the substantial amount of tissue autofluorescence within lesions in this range of the spectrum. The selection of yellow-red wavelengths provide for high signal to noise ratio imaging of atherosclerotic lesions without auto-fluorescence. QD are optimally-excited using ultraviolet to blue excitation wavelengths. Since ORO fluorescence is excited at ~650 nm, with peak emission in the range 670-700 nm (**Figure 5A**), macroscopic fluorescence imaging of ORO, QD585 (lymphocytes), and QD655 (monocytes) could be simultaneously performed in the same tissue, since the QD selected do not emit appreciable fluorescence when excited at 650 nm. Therefore, QD emission wavelengths can be selected for optimal multispecies imaging, and can also be integrated within conventional lesion analysis tools which use fluorescent dyes or immunohistochemical stains.

Several observations support the utility of QD for *in vivo* imaging applications involving vascular disease. The aorta is not directly accessible to optical imaging instrumentation, due to its deep location. However, given the high intensity and stability provided by QD in the aorta (**Figure 5**), we believe that optical imaging of atherosclerotic lesions *in vivo* is feasible. QD can be designed to emit in the near infrared emission windows for optimal *in vivo* imaging of tissues without the scattering and absorption limitations imposed by imaging of shorter wavelengths (35). Furthermore, although the UV-blue excitation light required to optimally excite QD would only have limited penetration in tissue due to scattering and absorption phenomena, two-photon excitation instruments have been designed for exciting QD optimally while at the same time overcoming these limitations (36). The prospect of using QD-antibody and QD-peptide bioconjugates for labeling cell surface biomarkers or the cytoplasm of specific subtypes of cells, combined with *in vivo* imaging instrumentation, should facilitate efforts toward the molecular profiling of atherosclerosis *in vivo* for developing diagnostic assays and disease-customized therapeutic interventions for clinical usage.

Conclusion

We have demonstrated a technique for monitoring the recruitment of leukocyte subsets to atherosclerotic lesions. The optical properties of QD can be harnessed to permit high signal to noise ratio imaging of multiple cell types without spectral overlap, and can also be used simultaneously with conventional immunofluorescence and immunohistochemical reagents used in the study of atherosclerosis. Given the implication of multiple cell types in the initiation and progression of atheroma, QD should be utilized to study these cell types within the same specimen in order to understand the interconnectedness of atherosclerotic mediators. Future efforts of this technique will include molecular profiling of atheroma *in vivo* including the monitoring of inflammatory biomarker expression in early and late stages of disease, and the assessment of therapeutic response *via* the tracking of genetically-engineered monocytes infused systemically in order to promote lesion regression *in vivo*.

Acknowledgements

This work was supported in part by National Institutes of Health grants T32EY07135 to Jeffrey Schall, PI (AJ), EY017522 (FRH), HL65405 (MFL), HL65709 and HL57986 (SF). Dr. Su was supported by the Diabetes Research and Training Center pilot and feasibility grant at Vanderbilt University (P60DK20593). We thank Elizabeth Dworska and Youmin Zhang for technical assistance.

References

(1) Libby, P., Ridker, P. M., and Maseri, A. (2002) Inflammation and atherosclerosis. *Circulation 105*, 1135-43.

(2) Swirski, F. K., Pittet, M. J., Kircher, M. F., Aikawa, E., Jaffer, F. A., Libby, P., and Weissleder, R. (2006) Monocyte accumulation in mouse atherogenesis is progressive and proportional to extent of disease. *Proc Natl Acad Sci U S A 103*, 10340-5.

(3) Libby, P., Geng, Y. J., Aikawa, M., Schoenbeck, U., Mach, F., Clinton, S. K., Sukhova, G. K., and Lee, R. T. (1996) Macrophages and atherosclerotic plaque stability. *Curr Opin Lipidol 7*, 330-5.

(4) Song, L., Leung, C., and Schindler, C. (2001) Lymphocytes are important in early atherosclerosis. *J Clin Invest 108*, 251-9.

(5) Yokota, T., and Hansson, G. K. (1995) Immunological mechanisms in atherosclerosis. *J Intern Med 238*, 479-89.

(6) Kruth, H. S., Huang, W., Ishii, I., and Zhang, W. Y. (2002) Macrophage foam cell formation with native low density lipoprotein. *J Biol Chem 277*, 34573-80.

(7) Davies, M. J., Richardson, P. D., Woolf, N., Katz, D. R., and Mann, J. (1993) Risk of thrombosis in human atherosclerotic plaques: role of extracellular lipid, macrophage, and smooth muscle cell content. *Br Heart J 69*, 377-81.

(8) Gupta, S., Pablo, A. M., Jiang, X., Wang, N., Tall, A. R., and Schindler, C. (1997) IFN-gamma potentiates atherosclerosis in ApoE knock-out mice. *J Clin Invest 99*, 2752-61.

(9) Mach, F., Schonbeck, U., Fabunmi, R. P., Murphy, C., Atkinson, E., Bonnefoy, J. Y., Graber, P., and Libby, P. (1999) T lymphocytes induce endothelial cell matrix metalloproteinase expression by a CD40L-dependent mechanism: implications for tubule formation. *Am J Pathol 154*, 229-38.

(10) Schonbeck, U., Mach, F., Sukhova, G. K., Atkinson, E., Levesque, E., Herman, M., Graber, P., Basset, P., and Libby, P. (1999) Expression of stromelysin-3 in atherosclerotic lesions: regulation via CD40-CD40 ligand signaling in vitro and in vivo. *J Exp Med 189*, 843-53.

(11) Paulsson, J., Dadfar, E., Held, C., Jacobson, S. H., and Lundahl, J. (2007) Activation of peripheral and in vivo transmigrated neutrophils in patients with stable coronary artery disease. *Atherosclerosis 192*, 328-34.

(12) Bobryshev, Y. V. (2005) Dendritic cells in atherosclerosis: current status of the problem and clinical relevance. *Eur Heart J 26*, 1700-4.

(13) Bobryshev, Y. V., and Lord, R. S. (2005) Co-accumulation of dendritic cells and natural killer T cells within rupture-prone regions in human atherosclerotic plaques. *J Histochem Cytochem 53*, 781-5.

(14) Cybulsky, M. I., Iiyama, K., Li, H., Zhu, S., Chen, M., Iiyama, M., Davis, V., Gutierrez-Ramos, J. C., Connelly, P. W., and Milstone, D. S. (2001) A major role for VCAM-1, but not ICAM-1, in early atherosclerosis. *J Clin Invest 107*, 1255-62.

(15) Cybulsky, M. I., Lichtman, A. H., Hajra, L., and Iiyama, K. (1999) Leukocyte adhesion molecules in atherogenesis. *Clin Chim Acta 286*, 207-18.

(16) Jaffer, F. A., Libby, P., and Weissleder, R. (2006) Molecular and cellular imaging of atherosclerosis: emerging applications. *J Am Coll Cardiol 47*, 1328-38.

(17) Jaffer, F. A., and Weissleder, R. (2004) Seeing within: molecular imaging of the cardiovascular system. *Circ Res 94*, 433-45.

(18) Amirbekian, V., Lipinski, M. J., Briley-Saebo, K. C., Amirbekian, S., Aguinaldo, J. G., Weinreb, D. B., Vucic, E., Frias, J. C., Hyafil, F., Mani, V., Fisher, E. A., and Fayad, Z. A. (2007) Detecting and assessing macrophages in vivo to evaluate atherosclerosis noninvasively using molecular MRI. *Proc Natl Acad Sci U S A 104*, 961-6.

(19) Lipinski, M. J., Amirbekian, V., Frias, J. C., Aguinaldo, J. G., Mani, V., Briley-Saebo, K. C., Fuster, V., Fallon, J. T., Fisher, E. A., and Fayad, Z. A. (2006) MRI to detect atherosclerosis with gadolinium-containing immunomicelles targeting the macrophage scavenger receptor. *Magn Reson Med 56*, 601-10.

(20) Nahrendorf, M., Jaffer, F. A., Kelly, K. A., Sosnovik, D. E., Aikawa, E., Libby, P., and Weissleder, R. (2006) Noninvasive vascular cell adhesion molecule-1 imaging identifies inflammatory activation of cells in atherosclerosis. *Circulation 114*, 1504-11.

(21) Tsourkas, A., Shinde-Patil, V. R., Kelly, K. A., Patel, P., Wolley, A., Allport, J. R., and Weissleder, R. (2005) In vivo imaging of activated endothelium using an anti-VCAM-1 magnetooptical probe. *Bioconjug Chem 16*, 576-81.

(22) Rudd, J. H., Warburton, E. A., Fryer, T. D., Jones, H. A., Clark, J. C., Antoun, N., Johnstrom, P., Davenport, A. P., Kirkpatrick, P. J., Arch, B. N., Pickard, J. D., and Weissberg, P. L. (2002) Imaging atherosclerotic plaque inflammation with [18F]-fluorodeoxyglucose positron emission tomography. *Circulation 105*, 2708-11.

(23) Jayagopal, A., Russ, P. K., and Haselton, F. R. (2007) Surface engineering of quantum dots for in vivo vascular imaging. *Bioconjug Chem 18*, 1424-33.

(24) Akerman, M. E., Chan, W. C. W., Laakkonen, P., Bhatia, S. N., and Ruoslahti, E. (2002) Nanocrystal targeting in vivo. *Proceedings of the National Academy of Sciences of the United States of America 99*, 12617-12621.

(25) Gao, X. H., Cui, Y. Y., Levenson, R. M., Chung, L. W. K., and Nie, S. M. (2004) In vivo cancer targeting and imaging with semiconductor quantum dots. *Nature Biotechnology 22*, 969-976.

(26) Esteve, E., Mabrouk, K., Dupuis, A., Smida-Rezgui, S., Altafaj, X., Grunwald, D., Platel, J. C., Andreotti, N., Marty, I., Sabatier, J. M., Ronjat, M., and De Waard, M. (2005) Transduction of the scorpion toxin maurocalcine into cells. Evidence that the toxin crosses the plasma membrane. *J Biol Chem 280*, 12833-9.

(27) Nakashima, Y., Plump, A. S., Raines, E. W., Breslow, J. L., and Ross, R. (1994) ApoE-deficient mice develop lesions of all phases of atherosclerosis throughout the arterial tree. *Arterioscler Thromb 14*, 133-40.

(28) Su, Y. R., Dove, D. E., Major, A. S., Hasty, A. H., Boone, B., Linton, M. F., and Fazio, S. (2005) Reduced ABCA1-mediated cholesterol efflux and accelerated atherosclerosis in apolipoprotein E-deficient mice lacking macrophage-derived ACAT1. *Circulation 111*, 2373-81.

(29) Fazio, S., Major, A. S., Swift, L. L., Gleaves, L. A., Accad, M., Linton, M. F., and Farese, R. V., Jr. (2001) Increased atherosclerosis in LDL receptor-null mice lacking ACAT1 in macrophages. *J Clin Invest 107*, 163-71.

(30) Taatjes, D. J., Wadsworth, M. P., Schneider, D. J., and Sobel, B. E. (2000) Improved quantitative characterization of atherosclerotic plaque composition with immunohistochemistry, confocal fluorescence microscopy, and computer-assisted image analysis. *Histochem Cell Biol 113*, 161-73.

(31) Wadsworth, M. P., Sobel, B. E., Schneider, D. J., Tra, W., van Hirtum, H., and Taatjes, D. J. (2006) Quantitative analysis of atherosclerotic lesion composition in mice. *Methods Mol Biol 319*, 137-52.

(32) Gao, X., Yang, L., Petros, J. A., Marshall, F. F., Simons, J. W., and Nie, S. (2005) In vivo molecular and cellular imaging with quantum dots. *Curr Opin Biotechnol 16*, 63-72.

(33) Voura, E. B., Jaiswal, J. K., Mattoussi, H., and Simon, S. M. (2004) Tracking metastatic tumor cell extravasation with quantum dot nanocrystals and fluorescence emission-scanning microscopy. *Nat Med 10*, 993-8.

(34) Su, Y. R., Ishiguro, H., Major, A. S., Dove, D. E., Zhang, W., Hasty, A. H., Babaev, V. R., Linton, M. F., and Fazio, S. (2003) Macrophage apolipoprotein A-I expression protects against atherosclerosis in ApoE-deficient mice and up-regulates ABC transporters. *Mol Ther 8*, 576-83.

(35) Graves, E. E., Weissleder, R., and Ntziachristos, V. (2004) Fluorescence molecular imaging of small animal tumor models. *Curr Mol Med 4*, 419-30.

(36) Larson, D. R., Zipfel, W. R., Williams, R. M., Clark, S. W., Bruchez, M. P., Wise, F. W., and Webb, W. W. (2003) Water-soluble quantum dots for multiphoton fluorescence imaging in vivo. *Science 300*, 1434-6.

CHAPTER V

FUNCTIONALIZED SOLID LIPID NANOPARTICLES FOR TRANSENDOTHELIAL DRUG DELIVERY

Ashwath Jayagopal
Eric M. Sussman
V. Prasad Shastri

Department of Biomedical Engineering
Vanderbilt University
Nashville, Tennessee

IEEE Trans Nanobioscience 7, 28-34. 2008.

Abstract

The objectives of this study were to synthesize and characterize functionalized solid lipid nanoparticles (fSLN), to investigate their interaction with endothelial cell monolayers, and to evaluate their transendothelial transport capabilities. fSLN bearing tetramethylrhodamine isothiocyanate-labeled bovine serum albumin (TRITC-BSA) and Coumarin 6 were prepared using a single-step phase inversion process that afforded concurrent surface modification with a variety of macromolecules such as polystyrene sulfonate (PSS), poly-L-lysine (PLL), heparin (Hep), polyacrylic acid (PAA), polyvinyl alcohol (PVA), and polyethylene glycol (PEG). TRITC-BSA/Coumarin 6 encapsulated in fSLN with composite surface functionality (PSS-PLL and PSS-PLL-Hep) were also investigated. Size and surface charge of fSLN were analyzed using dynamic light scattering and transmission electron microscopy. Transport across bovine aortic endothelial cell (BAEC) monolayers was assessed spectrophotometrically using a transwell assay, and fSLN localization at the level of the cell and permeable support was analyzed using fluorescence microscopy. fSLN with tunable size and surface functionality were successfully produced, and had significant effects on cell localization and transport. Specifically, fSLN with PSS-PLL-Hep composite surface functionalization was capable of translocating 53.2 ± 8.7 ug of TRITC-BSA within 4 hours, with fSLN-PEG, fSLN-PAA and fSLN-PSS exhibiting near-complete apical, paracellular, and cytosolic localization, respectively. Coumarin 6 was released by fSLN as indicated by dye labeling of BAEC membranes. We have developed a rapid process for the production of fSLN bearing low and high molecular weight payloads of varying

physicochemical properties. These findings have implications for drug delivery and bioimaging applications, since due to tunable surface chemistry, fSLN internalization and/or translocation across intact endothelial cell monolayers is possible.

Introduction

Endothelial barrier function governs the transport of information such as macromolecules and solutes from the blood to the tissues. The pathways through which this transport may occur have been identified to be paracellular (between cells) or transcellular (through cells) (*1*). Endothelial cells maintain a tight barrier compartmentalizing blood and tissue through multi-protein junction complexes (*2*), and utilize various machinery such as caveolae (*3*) to shepherd desired materials across or between the cell. Most processes involving the transport of macromolecules, such as clathrin-dependent endocytosis, direct cargoes to intracellular compartments, such as endosomes and lysosomes, as opposed to exocytosis at the basolateral membrane, and thus are not considered processes for translocation of compounds across endothelial barriers (*4*). Some small molecules, due to their small size (<500 Da) and/or lipophilicity, are capable of translocation across endothelial barriers, including the tight blood-brain barrier (*5*). However, it has been a significant challenge in pharmaceutical research to deliver imaging agents or therapeutics of varying physicochemical characteristics (e.g. high molecular weight, hydrophilic) across endothelial barriers with the same efficiency.

We have developed a strategy for the single-step encapsulation and surface functionalization of solid lipid nanoparticles (fSLN), based on a combined adaptation of the solvent-injection process by Schubert et al. (*6*) and a previously-described process in our laboratory for the development of functionalized polymeric nanoparticles (*7*). In our process, low and high molecular weight compounds of varying hydrophilicity and charge are entrapped within a coco-glyceride based, solid lipid matrix, with concurrent modification of the fSLN surface through incorporation of functional moieties in the aqueous phase. In this study, we investigated whether synthesizing fSLN with tunable surface functionalities of varying hydrophilic-lipophilic balance (i.e. negative, positive, bioactive) could impart endothelial barrier translocation properties. We demonstrate that fSLN can be engineered to achieve various cell interactions, and to transport compounds normally not capable of transcytosis across endothelial monolayers.

Materials and Methods

Materials

Softisan 100 was a gift from Sasol GmbH. Coumarin 6 (laser grade) was from Acros Organics. 3 µm pore size permeable cell culture supports (Transwell®) were from Corning. TRITC-BSA (1 mol TRITC/mol BSA), paraformaldehyde, Dulbecco's minimal essential medium (DMEM), fetal bovine serum (FBS), 1-methyl-2-pyrrolidone (NMP, anhydrous), dimethylformamide (DMF, ACS Grade), tetrahydrofuran (THF, ACS Grade), acetone (anhydrous), poly (styrene-4 sodium sulfonate) (MW = 70,000, (PSS)), poly (acrylic acid) (MW = 10000, (PAA)), poly (L-lysine hydrochloride) (MW = 22,100, (PLL)), poly (vinyl alcohol) (MW = 13,000, (PVA)), porcine heparin sodium salt (MW = 4000-6000, (Hep)), and hydroxyl-terminated poly (ethylene glycol) (MW = 10,000, (PEG)) were from Sigma. Float-a-Lyzer dialysis membranes (cellulose ester, 100K MWCO) were from Spectrum Laboratories. VECTASHIELD aqueous mounting medium for fluorescence microscopy was from Vector Labs. BAEC were a gift of Dr. Keith Gooch, and were used at passages 3-4. BAEC were cultured in DMEM containing 10% FBS and 1% penicillin/streptomycin/fungizone prior to transport experiments. BAEC cultures were free of fibroblast contamination.

Methods

Synthesis of Functionalized Solid Lipid Nanoparticles

fSLN bearing various surface functionalities were prepared using a modified phase inversion process (**Table 1**). 0.1% (w/v) Softisan 100 and 0.01% (w/v) Coumarin 6 were dissolved in a 1 mL organic phase consisting of the solvent pairs DMF/Acetone, THF/Acetone, or NMP/Acetone. Solvent ratios were adjusted stoichiometrically to achieve solvent compositions of varying solvent polarity-polarizability indices (SPP) as measured by Catalan (**Equation 1**) (*8, 9*). To this 1 mL of an aqueous phase consisting of 0.1% (w/v) TRITC-BSA and 0.001% (w/v) of one of the surface functionalization moieties (e.g. PSS, PLL) was added to yield the fSLN. Residual solvents and freely soluble functionalization moiety were removed by dialysis against 1 L double distilled deionized water (ddH$_2$O, Millipore) in Float-a-Lyzer dialysis membranes for four hours, with three complete changes of ddH$_2$O. Further modification of fSLN with composite functional surfaces, to synthesize fSLN-PSS-PLL, fSLN-PSS-PLL-Hep and fSLN-PLL-

Hep were prepared by electrostatic layer-by-layer (LBL) assembly (*10*). Specifically, fSLN-PSS, following dialysis, were incubated with 1% (w/v) PLL in ddH_2O under constant stirring for 5 minutes, and then dialyzed in a similar manner as described above. fSLN bearing composite surface functionality was then achieved by incubating SLN-PSS-PLL or SLN-PLL in 1% (w/v) Hep in ddH_2O under constant stirring for 5 minutes, followed by 100K MWCO dialysis to generate fSLN bearing PSS-PLL-Hep and PLL-Hep, respectively.

Table 1. Specific fSLN formulations prepared and their general properties.

- Charge	**+ Charge**	**Neutral**	**Bioactive**	**Multifunctional**
Poly (acrylic acid) (**PAA**)	Poly (L-lysine) (**PLL**)	Poly (ethylene glycol) (**PEG**)	Heparin (**Hep**)	**PSS-PLL**
Poly (styrene-4-sodium sulfonate) (**PSS**)		Poly (vinyl alcohol) (**PVA**)		**PLL-Hep**
				PSS-PLL-Hep

$$SPP = SPP_A \cdot V_A + SPP_B \cdot (1 - V_A) \tag{1}$$

Equation 1. Solvent Polarity-Polarizability Index Calculation for binary solvent systems, where V_x = volume of compound X, SPP_Y = SPP index value for solvent Y, as determined by Catalan (*8*).

fSLN Size and Zeta Potential Characterization

The size distribution and zeta potential (ζ) of the fSLN suspensions were determined in triplicate using a Beckman-Coulter DELSA 440SX Zetasizer. Additionally, ζ was mapped as a function of pH to determine the isoelectric point (*11*) of the fSLN surface. Briefly, 200 µL of SLN suspension was suspended in a total of 2 mL ddH_2O adjusted to the desired pH with 2 N HCl or 2 N NaOH as needed prior to ζ measurement. Size distribution was monitored for several months post-fSLN synthesis to ascertain the effect of storage (4°C) on size.

Low-Voltage Transmission Electron Microscopy (LVTEM)

fSLN-PSS were imaged using LVEM5 (DeLong Instruments). fSLN were air-dried onto 3 mm grids and then imaged at 5kV under 10^{-5} mbar vacuum. The image was captured using an attached CCD camera (Proscan 1300 x 1030 pixels) and processed using a ProDIA Image Processing Software.

In vitro Transendothelial Transport Studies

P_3 or P_4 BAEC were plated onto polycarbonate inserts at a nominal density of 50,000 cells/cm^2 and the inserts were assembled in wells of a 12-well tissue culture microplate. BAEC incubated at in a humidified incubator at 37°C and 5% CO_2, until confluent (2-3 days).

Prior to *in vitro* transport studies, the receiver compartments of the 12-well plates were filled with 400 µl Ringers' solution supplemented with 10% FBS and the monolayers were bathed with 200 µl Ringers' solution supplemented with 10% FBS. Next, 200 µL of the fSLN suspension in Ringers' was added to the upper compartment, and the cells were incubated for 4 hours at 37°C. Ringers' supplemented with 10% FBS containing 0.1% TRITC-BSA served as controls in order to verify integrity of the monolayer during the transport studies. We initially verified that exposure to Ringers for 4 hours did not affect BAEC monolayer integrity as assessed by the absence of visible discontinuities in the cell monolayer in micrographs. Experiments were performed in triplicate. SLN produced using the NMP/Acetone binary solvent system was selected for transport studies due to their size reproducibility even under slight variations in SPP.

In selected wells, 1 mg/mL Texas Red-Dextran (MW = 10 kDa, neutral, Invitrogen) was incubated with BAEC monolayers seeded on Transwell inserts for 1 hr. in Ringers'/FBS, then rinsed 3 times with PBS and fixed. In addition, Texas Red-dextran was incubated with BAEC 1 hour following BAEC incubation with fSLN-PSS-PLL-Hep, in order to assess effects on the paracellular permeability of the BAEC monolayer. In these cases, the receiver compartment was replaced with fresh Ringers'/FBS solution to remove interfering fluorescence from fSLN. Permeability coefficients were calculated based on dextran concentrations as previously-described (*12*).

Following incubation, the media covering the cells was removed carefully using micropipette and rinsed three times with Ringers followed by fixation with 4% paraformaldehyde for 10 minutes. The Transwell inserts were removed and mounted on a glass slide using VECTASHIELD/DAPI. The 12-well microplates were then analyzed in a Biotek Synergy HT microplate fluorescence spectrophotometer configured for TRITC, Coumarin 6, and Texas Red-specific channels to measure SLN translocation across the BAEC monolayer. For formulations indicating high translocation via microplate spectrophotometry (more than 15% fluorescence intensity above BAEC not incubated with fSLN), the concentration of TRITC-BSA in the receiver compartment solution was determined *via* fluorescence spectrophotometry. The solution was exposed to 40ºC temperature to melt solid lipid, and filtered through an Amicon-4 spin column centrifugation device with 10K MWCO in order to concentrate TRITC-BSA and remove free lipid. Concentration was measured using a Nanodrop ND-3300 fluorescence spectrophotometer calibrated by a TRITC-BSA standard curve in Ringers'/10% FBS solution prepared by the same heating/concentration preparation steps. Texas Red-Dextran in the receiver compartment was measured by fluorescence spectrophotometry using a standard curve.

Visualization of fSLN in BAEC Monolayers

The mounted Transwell supports were imaged using a Nikon TE2000U inverted fluorescence microscope equipped with a motorized computer-controlled z-focus device (Ludl, Inc.) using TRITC and FITC filters for TRITC BSA and Coumarin 6 respectively. Using Image Pro Plus 5.1 in conjunction with ScopePro 5.0 (Media Cybernetics), 2-D slices of BAEC in each channel were acquired by sequentially exposing a field of view under TRITC and FITC filters to generate a co-registered image showing fSLN and Coumarin 6 localization in the same frame. The z-stacks were deblurred using a constrained, iterative algorithm (Inverse Filter, Sharpstack 5.2.2) calibrated to imaging objective settings (Plan Apo 40X oil immersion), and combined to construct cross-sections that restrict out-of-focus haze from slices not within the X-Y plane of interest. Cross sections were generated from high-resolution TIFFs using Andor iQ 1.5 image analysis software (Andor Bioimaging).

For evaluation of fSLN-PSS localization within BAEC in culture, cells were seeded to confluency in 6-well microplates and imaged *via* fluorescence microscopy using phase contrast and TRITC settings.

Cytotoxicity of BAEC exposed to fSLN

BAEC seeded to confluency on 6-well microplates were incubated with fSLN-PSS or fSLN-PSS-PLL-Hep suspensions for four hours in Ringers'/FBS. Cells were rinsed three times and detached with 0.25% trypsin, and resuspended into ice-cold PBS/EDTA pH = 7.4. Cells were then incubated with LIVE/DEAD single color fixable (green) viability kit (Invitrogen) according to manufacturer instructions, and assayed for viable/dead cells using a BD FACSCalibur flow cytometer equipped with 488 nm laser. The dead cell proportion, showing a log-scale enhancement in green (FL1) fluorescence, was quantified using FlowJo 7.2.2 (TreeStar software) in order to express %viability of BAEC populations as compared to Ringers'/FBS exposure alone. A minimum of 20,000 cells were assayed per sample.

Results

Size and Surface Charge Characterization

In our process, by varying the SPP of the organic phase, fSLN diameter was tunable. The organic phase was composed of acetone and a highly polar secondary phase (NMP, THF, or DMF). Increasing the polarity of this phase (higher SPP) resulted in a reduction in fSLN mean diameter (**Figure 1**). While the THF-Acetone system offered fSLN over a much wider range than the other systems investigated, the NMP-

Acetone system afforded the particles with highest size reproducibility with variance in SPP. This suggests that the range of NMP-Acetone volume fractions studied all have high miscibility with water, favoring rapid phase inversion and lipid packing, which subsequently promotes the formation of fSLN of smaller size. fSLN prepared by our process appeared to be fairly monodispersed as satellite populations above and below the size of the major population peak were wither minimal or absent.

All three solvent systems were capable of producing stable nanoparticles, as indicated by lack of coagulation/turbidity in solution over a month of storage, except for the case of fSLN-PLL, which noticeably coagulated in suspension within 24 hours post-synthesis. The spherical morphology of the fSLN was confirmed by low-voltage TEM (**Figure 2**). Following storage at 4°C for one month, fSLN-PSS (SPP = 93.44) exhibited a small change (4.54%, n = 3) in mean diameter as measured by dynamic light scattering.

The incorporation of the prescribed functional group in the aqueous phase onto the SLN surface was verified by measuring the pI_e of the fSLN surface. This was performed by mapping the ζ of the fSLN as function of pH. pI_e corresponded reasonably well with that for the pKa of the ionizable group in the functional moiety (**Figure 3**). Thus, entrapment of the functional moiety on the SLN surface was achieved at concentrations sufficient to impart its charge characteristics.

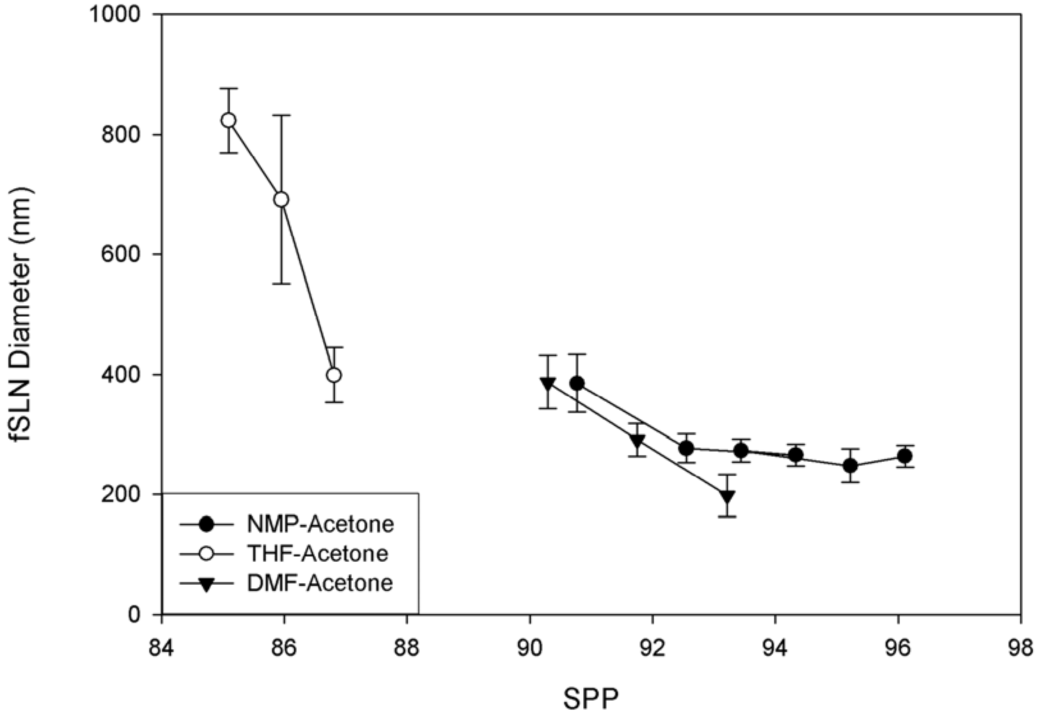

Figure 1. fSLN-PSS Diameter as a function of solvent polarity-polarizability index (SPP) for three different binary solvent systems of varying solvent composition (n=3). All solvent pairs consisted of Acetone and one of NMP, DMF, or THF. Diameter was not affected by the incorporation of other surface functionalities (data not shown). SLN diameter is expressed as a peak (>80%) value from size distribution analysis using multi-angle dynamic light scattering.

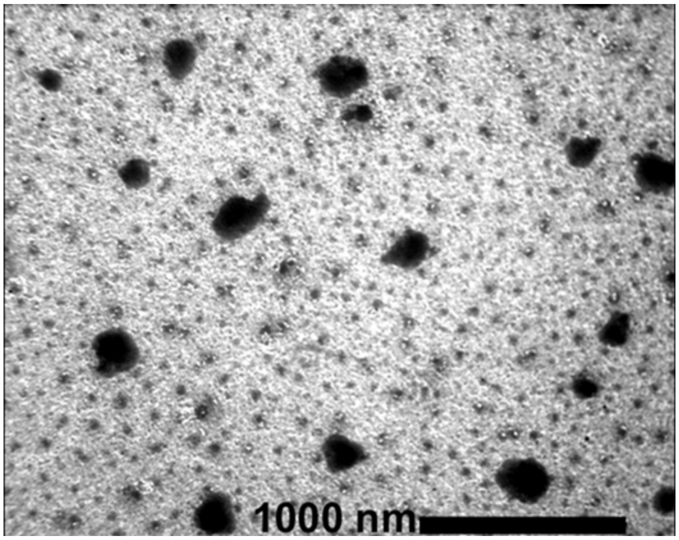

Figure 2. LVTEM of fSLN-PSS synthesized using the NMP/Acetone binary solvent system. Compacted nanoparticles (black regions) with spherical morphology are apparent. Air-drying artifacts distort nanoparticle size measured by dynamic light scattering.

Surface Charge Characterization of Composite fSLN

The impartation of composite layered surface functionalities (PSS-PLL, PSS-PLL-Hep, PLL-Hep) was verified by measuring the ζ, of fSLN at physiological pH (7.4), which for fSLN-PSS-PLL and fSLN-PSS-PLL-Hep was 8.72 ± 3.22 mV and 2.82 ± 1.71 mV, respectively. ζ for fSLN-PSS at pH = 7.4 was -42.40 ± 5.78 mV (**Figure 3**), collectively suggesting that fSLN-PSS-PLL-Hep surfaces are composed of both PLL and Hep.

In vitro Transendothelial Transport Studies

Of all formulations tested, fSLN bearing the composite layered functionality of PSS-PLL-Hep afforded the most translocation of BSA (fluorescence intensity corresponding to 53.2 ± 8.7 µg as determined by fluorescence spectrophotometry, **Figure 4**). The relative amount of TRITC-BSA translocated across BAEC in the PSS-PLL-Hep system was 22-fold greater than the second most efficient system, fSLN-PLL-Hep, and about 160-fold greater than TRITC-BSA/Ringers' control. Previous studies reported a baseline flux of < 0.05 pmol BSA/hr for intact BAEC monolayers, a rate three orders of magnitude lower than observed for the fSLN-PSS-PLL-Hep system in this study (*13*). fSLN-PEG and fSLN-PVA systems did not transport detectable levels of TRITC-BSA in the receiver compartment. Furthermore, Coumarin 6 was not detected in the receiver compartments for any formulation tested.

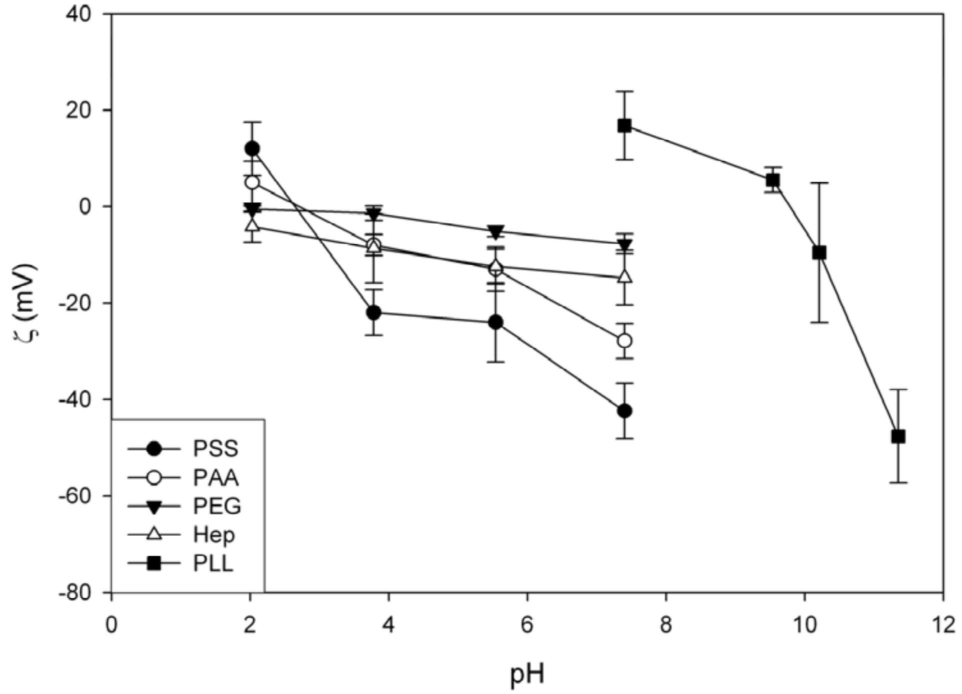

Figure 3. Zeta potential (ζ) as a function of pH for various functionalized SLN (n = 3, reported as mean ± S.D.). The isoelectric point (*11*) of the sample (point at which ζ = 0 mV) corresponds closely with the pKa of the surface functionality's ionizable group (PSS = sulfonic acid (pKa = 2.1), PAA = acrylic acid (pKa = 4), PLL = amine (10.5), Hep = uronic acid (3.13), PEG = hydroxyl (5))

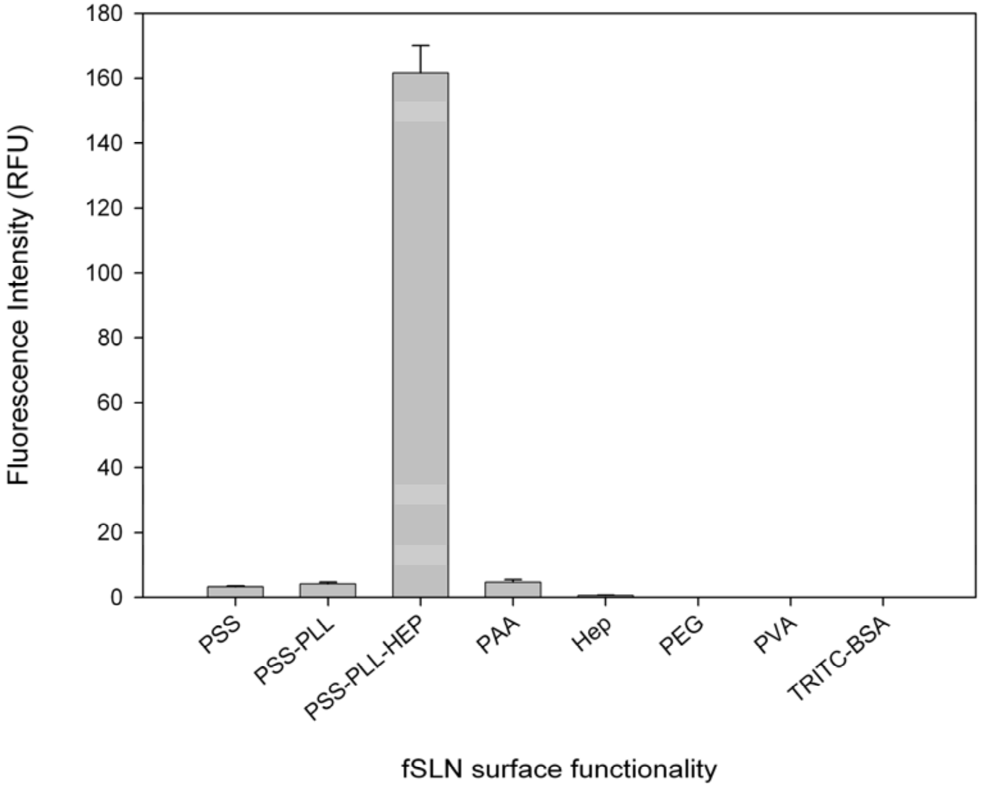

Figure 4. Fluorescence spectrophotometry of fSLN/TRITC-BSA transport across BAEC monolayers for a variety of surface functionalities (n = 3, reported as mean ± S.D.). Fluorescence intensity of fSLN-PSS-PLL-HEP-associated receiver compartment was measured to correspond to 53.2 ± 8.7 μg of TRITC-BSA. Other fSLN species were below thresholds of TRITC detection in receiver compartments.

Endothelial monolayer integrity following fSLN-PSS-PLL-Hep translocation was measured using a dextran permeability assay. Dextran is known to translocate BAEC monolayers *via* a paracellular route, and thus has been used to measure the integrity of endothelial barriers and their tight junctions (*14*). Prior to incubation with fSLN, permeability of Texas Red-dextran (MW = 10,000) across BAEC monolayers after 1 hr. was $9.1 \times 10^{-6} \pm 3.5 \times 10^{-7}$ cm/s. Following 4 hr. incubation with fSLN-PSS-PLL-Hep, the 1 hr. dextran permeability was $9.6 \times 10^{-6} \pm 4.3 \times 10^{-7}$ cm/s (n = 3). These data were similar, and also consistent with previous studies of dextran permeation across intact monolayers (*15*). Thus, endothelial integrity at this timepoint was not compromised with regard to the paracellular transport pathway. In addition, fSLN-PSS-PLL-Hep were detectable by fluorescence microscopy in the receiver compartment, indicating that fSLN can be transported across monolayers intact, while maintaining stability in serum (**Figure 5**).

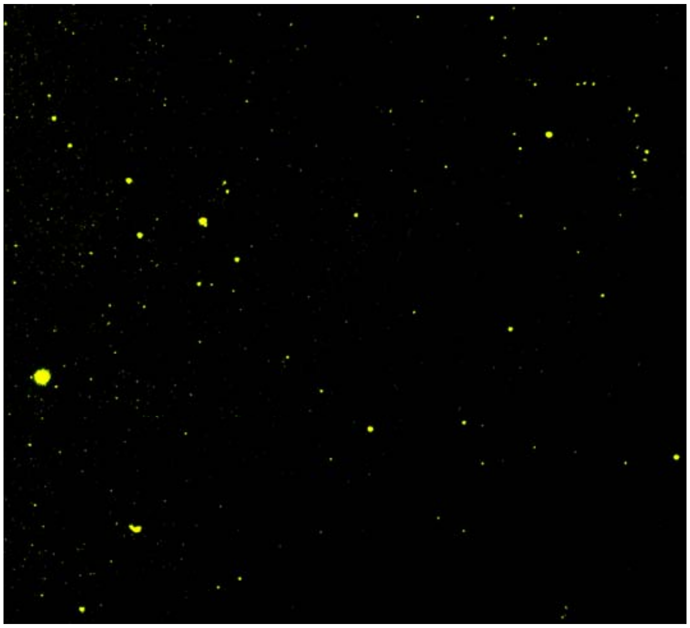

Figure 5. fSLN-PSS-PLL-Hep observed by fluorescence microscopy in receiver compartments following transendothelial transport assays.

Fluorescence Microscopy of BAEC Incubated with Functionalized SLN

Fixed BAEC monolayers were imaged using fluorescence microscopy to assess localization and extent of transport within monolayers. Representative fluorescence micrographs from the six most efficacious fSLN formulations are shown in **Figure 6**. Our data suggests that the chemical composition of the SLN surface dictates various aspects of fSLN interaction with BAEC monolayers including compartment of localization (intracellular versus apical cell surface), and transport pathway (paracellular versus transcellular).

Among the negatively charged fSLN, fSLN-PSS exhibited intracellular localization, with a diffuse cytoplasmic distribution, but without passage through endothelium (**Figure 6F**). To confirm this distribution, fSLN-PSS incubated with BAEC on tissue culture polystyrene were also imaged for greater clarity by fluorescence microscopy, and fSLN distribution within cell cytoplasm was similar (**Figure 7**). fSLN-Hep was internalized within BAEC, but appeared to be sequestered in the cytoplasm and not translocated, as indicated by a lack of fluorescence at the support membrane level (**Figure 6C**). fSLN-PAA particles, however appeared to primarily localize along cell-cell junctions (**Figure 6D**). These results suggest that impact of charge in cellular interaction in this system might be secondary to other considerations such physicochemical characteristics of the surface functional moiety.

Among the fSLN with composite surface functionality, fSLN-PLL-Hep (**Figure 6B**) was distributed primarily along paracellular regions and/or at the apical surface. Furthermore, no accumulation of these particles at the level of the Transwell membrane insert was observed, suggesting a lack of translocation. This is significantly different

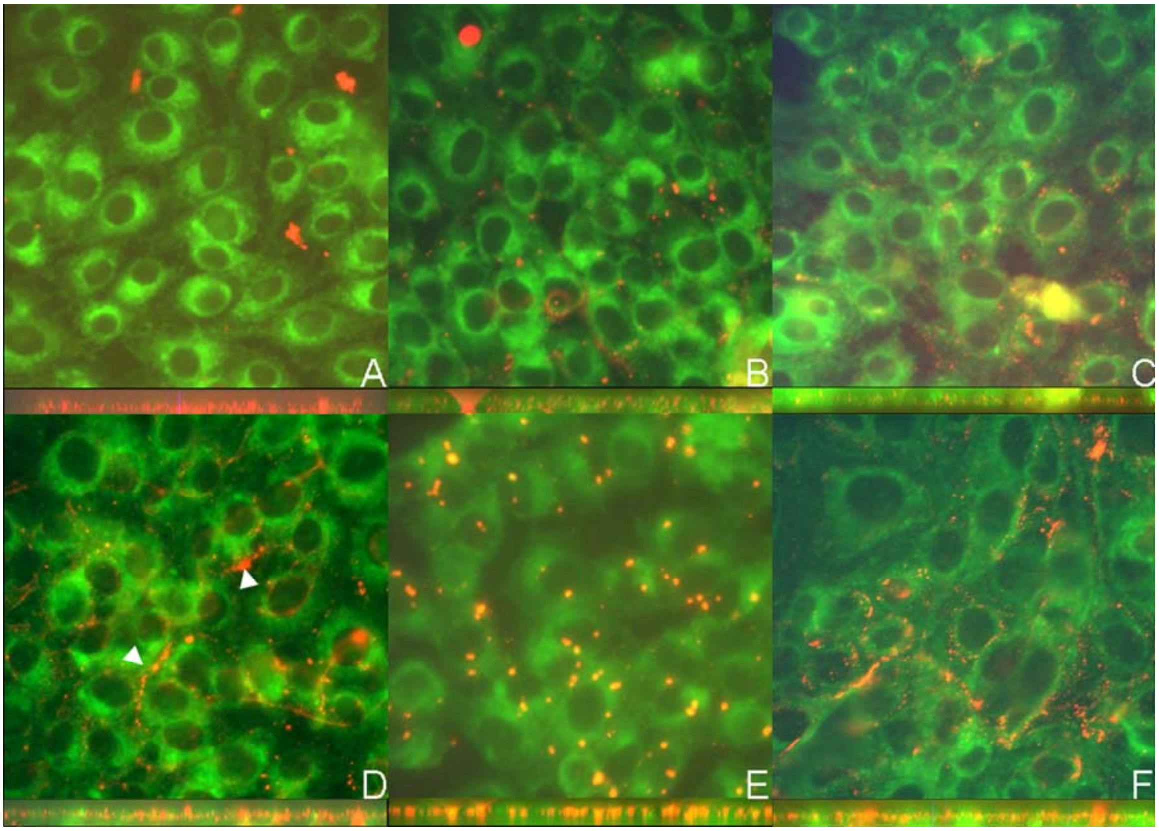

Figure 6. Fluorescence microscopy of permeable supports with fixed BAEC monolayers following *in vitro* SLN transendothelial transport studies. Each of the 6 display items consist of a 2-D view of the monolayer at the middle of the cell (*16*) and a cross-sectional view of the same monolayer processed via deblurring and reconstruction from a 3-D stack through the insert (bottom). TRITC-BSA is red, and Coumarin 6 is green; a mixture of the two is orange in color. Images are representative of experiments performed in triplicate. SLN formulations displayed are (A) fSLN-PSS-PLL-Hep, (B) fSLN-PLL-Hep, (C) fSLN-Hep, (D) fSLN-PAA (arrowheads show localization along cell borders), (E) fSLN-PEG, and (F) fSLN-PSS. (fSLN-PSS-PLL data not shown) (Magnification 400X)

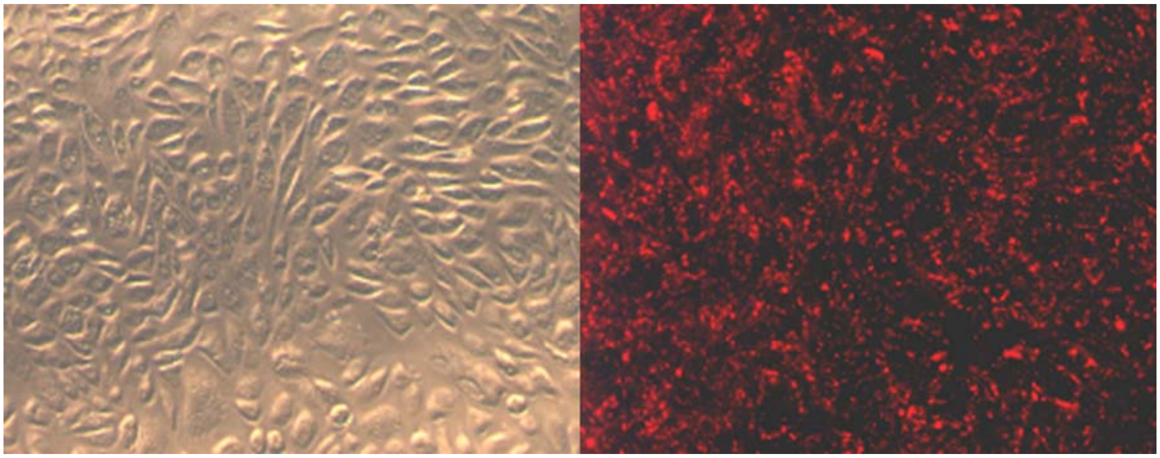

Figure 7. Fluorescence micrographs of BAEC incubated with fSLN-PSS. All cells in view are efficiently and diffusely labeled with TRITC-BSA containing nanoparticles (pseudocolored red). (Magnification 100X)

from the fSLN-Hep system, which also possesses a net negative surface charge, and once again alludes to fSLN-cell interactions that are more complex and driven by physicochemical considerations. Similarly, no appreciable translocation was observed in fSLN-PSS-PLL (data not shown), although its positively charged surface is more favorably disposed toward interacting with negatively charged cell surfaces. These observations are consistent with transendothelial transport studies (**Figure 4**). In contrast, fSLN-PSS-PLL-Hep (**Figure 6A**) was primarily localized to paracellular transport regions, also known as tight junctions, although in some cases larger SLN were restricted to the apical cell surface without entry. As shown in the cross-sectional image derived from 3-D image processing (**Figure 6A**), fSLN-PSS-PLL-Hep bearing TRITC-BSA were transported to the level of the permeable support (bottom layer of image). This level of monolayer permeation was not observed for any other species tested. In the transport studies this system yielded the highest fluorescence in the receiver compartment as well (**Figure 4**). No translocation was observed in the fSLN-PEG (**Figure 6E**) and fSLN-PVA system (fSLN-PVA data not shown). These fSLN remained primarily associated with the plasma membrane near the apical surface as highly compacted nanoparticle aggregates, with no detected populations at support boundaries. Since the samples were thoroughly washed prior to fixing, these interactions represent stable cell surface incorporation. In all inserts, it was observed that Coumarin 6 was partitioned effectively in the cell membrane. This could be due to either leakage of the small molecule through the fSLN, or additionally, partitioning of the dye within cell membranes upon initial fSLN contact with BAEC. Further investigation is necessary to determine the primary mechanism of small molecule release, as this study would be important for investigating fSLN as drug delivery formulations.

Cytotoxicity Analysis

The toxicity profile of fSLN was assessed using a membrane integrity dye in conjunction with flow cytometry, and was found to be similar to Ringers'/FBS exposure alone (**Figure 8**). These results, in conjunction with dextran permeability studies, demonstrate that fSLN constitute a biocompatible approach for the translocation of compounds across endothelium.

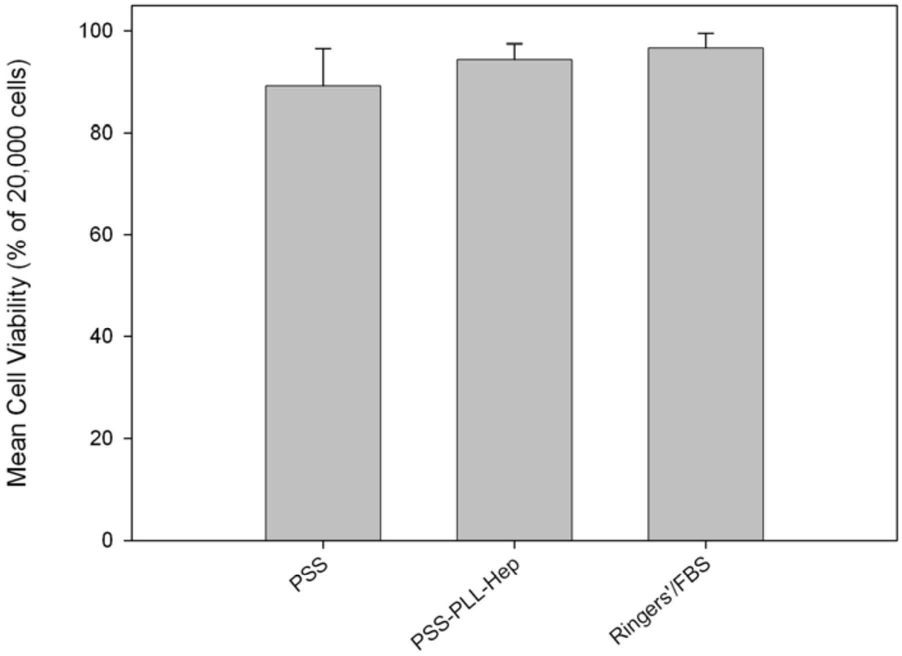

Figure 8. Flow cytometric toxicity analysis. BAEC were incubated with fSLN-PSS or fSLN-PSS-PLL-Hep for 4 hrs. in culture. Viability of fSLN-labeled cells was similar to BAEC incubated in Ringers'/FBS. Data reported as %viable (mean ± S.D., n = 3) BAEC from a sample of 20,000 assayed cells.

Discussion

The ability to deliver of therapeutics and imaging agents of diverse physicochemical properties across endothelial barriers has key implications in the diagnosis and treatment of high-impact diseases such as cancer, atherosclerosis, and diabetes. In general, current methods for traversing endothelium may not be suitable for high molecular weight compounds, or may expose the underlying tissue to the unrestricted influx of compounds as a result of prolonged barrier perturbation. In our approach, we have selected a solid lipid, the hydrogenated coco-glyceride Softisan 100, as a biocompatible starting material for the delivery of compounds across endothelial barriers, as it is a component of many topical formulations for the purpose of imparting enhanced spreading and permeation characteristics (*17, 18*).

The physicochemical characteristic of fSLN surfaces appears to be the dominant parameter in dictating their destination within or across endothelial cells. Among the various fSLN studied, fSLN bearing the composite surface derived from PSS, PLL and Hep afforded the most efficacious transport across BAEC monolayers. Since this efficiency of translocation was not observed for individual components of this formulation (i.e. fSLN-PSS, fSLN-PSS-PLL, fSLN-PLL-Hep), it is apparent that all three moieties are necessary to achieve high molecular weight payload translocation. A possible mechanism involving diminished cellular membrane interaction due to the presence of the negatively-charged PSS and some specific interactions with cell junctions through tight-junction proteins with affinity for heparin may be involved, with the PLL layer serving as a molecular bridge between the PSS and Hep regions on the fSLN surface. This mechanism seems reasonable based on the experimental observations and what is known about heparin. Heparin is a highly bioactive polysaccharide involved in critical endothelial cell functions. Heparin is present in many configurations which serve to elicit distinct responses from endothelial cells, which also have specific heparin-binding sites (*19-21*). Furthermore, heparin is involved in the transcytosis of biomolecules across endothelium (*16*). However, in our studies, fSLN-Hep, while appearing to be stable nanoparticles, were not capable of transcytosis. This observation is consistent with the proposed mechanism wherein the relatively hydrophobic, but negatively charged PSS has a role in favoring interaction with tight junctions. Further studies are warranted to ascertain if the ultrastructure of Hep are altered by the presence of strongly-charged polyelectrolytes in conjunction with a neutral solid lipid.

Some of the cell interaction characteristics of the fSLN warrant further attention. fSLN-PSS were observed to efficiently and homogenously penetrate cell membranes into cytoplasmic space. A lack of aggregation of the particles suggests that the cytoplasmic distribution may not entirely involve the endosomal pathway. As discussed earlier, PSS may inhibit solid lipid interactions with cell surface domains, in turn facilitating direct membrane fusion. fSLN-PAA was observed to possess a very high affinity for the cell-cell boundaries. However, this site-specific aggregation did not appear to facilitate transendothelial transport. Coating of fSLN with PEG resulted in localization of nanoparticles exclusively to cell surfaces. The exclusion volume created by the gyration of PEG tethers on the fSLN surface may prevent lipid-lipid interactions entirely. Our preliminary efforts to probe the effects of fSLN on endothelial barrier integrity and cytotoxicity suggest that lipid nanoparticles do not adversely effect cell viability or barrier properties, as indicated by flow cytometric and dextran permeability assays.

Our initial studies concerning the synthesis, characterization, and *in vitro* transendothelial transport properties of fSLN warrant their future investigation as versatile drug or bioimaging probe carriers for vascular disease. Our process provides for the rapid, single-step encapsulation of physicochemically-diverse compounds within stable solid lipid matrices, which can concurrently be engineered at their biological interface to exhibit novel properties, such as transcellular or intracellular penetration. We anticipate its further investigation as a multimodal delivery system for bioimaging, drug delivery, and/or gene therapy.

Acknowledgements

This work was supported by support from the Vanderbilt Institute of Chemical Biology (VICB) and the Vanderbilt Institute of Integrative Biosystems Research and Education (VIIBRE). AJ was supported by a graduate training grant fellowship from the Vanderbilt Vision Center (EY07135). The authors thank Prof. Frederick Haselton for helpful discussion.

References

(1) Mehta, D., and Malik, A. B. (2006) Signaling mechanisms regulating endothelial permeability. *Physiol Rev 86*, 279-367.

(2) Haselton, F. R., and Heimark, R. L. (1997) Role of cadherins 5 and 13 in the aortic endothelial barrier. *J Cell Physiol 171*, 243-51.

(3) Minshall, R. D., Sessa, W. C., Stan, R. V., Anderson, R. G., and Malik, A. B. (2003) Caveolin regulation of endothelial function. *Am J Physiol Lung Cell Mol Physiol 285*, L1179-83.

(4) Muro, S., Koval, M., and Muzykantov, V. (2004) Endothelial endocytic pathways: gates for vascular drug delivery. *Curr Vasc Pharmacol 2*, 281-99.

(5) Gonzalez-Mariscal, L., Nava, P., and Hernandez, S. (2005) Critical role of tight junctions in drug delivery across epithelial and endothelial cell layers. *J Membr Biol 207*, 55-68.

(6) Schubert, M. A., and Muller-Goymann, C. C. (2003) Solvent injection as a new approach for manufacturing lipid nanoparticles--evaluation of the method and process parameters. *Eur J Pharm Biopharm 55*, 125-31.

(7) Sussman, E. M., Clarke, M. B., Jr., and Shastri, V. P. (2007) Single-Step Process to Produce Surface-Functionalized Polymeric Nanoparticles. *Langmuir 23*, 12275-12279.

(8) Catalan, J., Lopez, V., and Perez, P. (1995) Solvent Dipolarity Polarizability (Spp) of Alcoholic Solvents. *Liebigs Annalen*, 793-795.

(9) Drago, R. S. (1992) A Unified Scale for Understanding and Predicting Nonspecific Solvent Polarity - a Dynamic Cavity Model. *Journal of the Chemical Society-Perkin Transactions 2*, 1827-1838.

(10) Decher, G. (1997) Fuzzy nanoassemblies: Toward layered polymeric multicomposites. *Science 277*, 1232-1237.

(11) Farmer, P. J., Bernier, S. G., Lepage, A., Guillemette, G., Regoli, D., and Sirois, P. (2001) Permeability of endothelial monolayers to albumin is increased by bradykinin and inhibited by prostaglandins. *Am J Physiol Lung Cell Mol Physiol 280*, L732-738.

(12) Moldobaeva, A., and Wagner, E. M. (2002) Heterogeneity of bronchial endothelial cell permeability. *Am J Physiol Lung Cell Mol Physiol 283*, L520-7.

(13) Chakravortty, D., Koide, N., Kato, Y., Sugiyama, T., Kawai, M., Fukada, M., Yoshida, T., and Yokochi, T. (2000) Cytoskeletal alterations in lipopolysaccharide-induced bovine vascular endothelial cell injury and its prevention by sodium arsenite. *Clin Diagn Lab Immunol 7*, 218-25.

(14) DeMaio, L., Antonetti, D. A., Scaduto, R. C., Jr., Gardner, T. W., and Tarbell, J. M. (2004) VEGF increases paracellular transport without altering the solvent-drag reflection coefficient. *Microvasc Res 68*, 295-302.

(15) DeMaio, L., Rouhanizadeh, M., Reddy, S., Sevanian, A., Hwang, J., and Hsiai, T. K. (2006) Oxidized phospholipids mediate occludin expression and phosphorylation in vascular endothelial cells. *Am J Physiol Heart Circ Physiol 290*, H674-83.

(16) Obunike, J. C., Lutz, E. P., Li, Z., Paka, L., Katopodis, T., Strickland, D. K., Kozarsky, K. F., Pillarisetti, S., and Goldberg, I. J. (2001) Transcytosis of lipoprotein lipase across cultured endothelial cells requires both heparan sulfate proteoglycans and the very low density lipoprotein receptor. *J Biol Chem 276*, 8934-41.

(17) Eros, I., Soosne-Csanyi, E., and Selmeczi, B. (1994) [Influence of viscosity on drug release from ointments, creams, gels and emulsions]. *Acta Pharm Hung 64*, 57-61.

(18) Souto, E. B., Muller, R. H., and Gohla, S. (2005) A novel approach based on lipid nanoparticles (SLN) for topical delivery of alpha-lipoic acid. *J Microencapsul 22*, 581-92.

(19) Khorana, A. A., Sahni, A., Altland, O. D., and Francis, C. W. (2001) Heparin inhibition of endothelial cell proliferation and angiogenesis is dependent on molecular weight. *Blood 98*, 49a-49a.

(20) Khorana, A. A., Sahni, A., Altland, O. D., and Francis, C. W. (2003) Heparin inhibition of endothelial cell proliferation and organization is dependent on molecular weight. *Arteriosclerosis Thrombosis and Vascular Biology 23*, 2110-2115.

(21) Patton, W. A., 2nd, Granzow, C. A., Getts, L. A., Thomas, S. C., Zotter, L. M., Gunzel, K. A., and Lowe-Krentz, L. J. (1995) Identification of a heparin-binding protein using monoclonal antibodies that block heparin binding to porcine aortic endothelial cells. *Biochem J 311 (Pt 2)*, 461-9.

CHAPTER VI

INTRACELLULAR DELIVERY OF MULTIMODAL SOLID LIPID NANOPARTICLES FOR BIOIMAGING AND DRUG DELIVERY

Ashwath Jayagopal
Richard D. Dortch
Eric M. Sussman
Frederick R. Haselton
Mark D. Does
V. Prasad Shastri

Department of Biomedical Engineering
Vanderbilt University
Nashville, Tennessee

Introduction

The efficient intracellular targeting of both clinical imaging and therapeutic agents poses a significant challenge in medicine and biology. Optimal systems for this purpose should feature biocompatibility, the capability to deliver physicochemically-diverse payloads such as nanoparticles or proteins, evasion of the endo-lysosomal pathway of internalization, and an amenability to surface functionalization for tuning of interfacial characteristics. Here we report on the application of multimodal functionalized solid lipid nanoparticles (fSLN) for efficient delivery into the cytosol with low toxicity. fSLN were capable of encapsulating various nanoparticulate and chemotherapeutic payloads. Delivery of fSLN into the cytosol was achieved after pre-incubation of endothelial cells and cell lines at 4°C, and without colocalization with endosomes. fSLN-labeled cells could be imaged, depending on the payload, by magnetic resonance imaging, fluorescence imaging, and/or light microscopy, and paclitaxel-loaded fSLN were capable of inducing cell cycle arrest. fSLN are a novel vehicle for the delivery of diverse payloads into cells without endosomal sequestration or chemical modification of the encapsulated payload itself.

Current approaches directed toward the goal of intracellular drug targeting and/or imaging include the use of cationic peptides (*1, 2*) or polymers (*3*), and nanoparticulate formulations such as ligand-conjugated liposomes (*4*), dendrimers (*5*) or cholesterol-based carriers (*6, 7*). Many of these strategies are limited by cytotoxicity at modest doses, reliance on endocytosis, adverse modification of the drug/imaging agent, and a decrease in delivery efficiency with increasing payload size. We therefore sought to develop a biocompatible delivery paradigm which would enable the rapid intracellular delivery of a diverse range of imaging agents and therapies without compromising their functions.

Highly-biocompatible solid lipids, or "hard fats," have been utilized extensively in dermatological and cosmetic applications for the ability to promote permeation and of topically-applied compounds (*8-10*). However, studies to elucidate the nature of their contact with cell membranes on the microscale have not been carried out with great detail. We hypothesized that some solid lipids may have intimate interactions with plasma membranes such that the translocation of co-formulated species, such as drugs or nanoparticles, is enabled. We conducted studies to determine whether solid lipids could be formulated into nanoscale pharmaceutical or contrast agent carriers. A discrete class of solid lipids, hydrogenated coco-glycerides, were identified by our laboratory which could be formulated into nanoparticles ranging from approximately 80-900 nm (*11*).

fSLN synthesis using these solid lipids is accomplished by the solvent-assisted formation of a microemulsion (*11, 12*). In this process, the lipid is dissolved within an organic solvent system of tunable polarity, such that the affinity of the solution for water is controllable. Upon the addition of an aqueous phase to the solvent mixture, the hydrophobic packing of the lipid upon exposure to water provides for instantaneous formation of a nanoscale particle, the size of which is determined by the polarity of the organic phase. Higher solvent polarity permits rapid phase inversion as water miscibility is higher, whereas lower solvent polarity extends the nanoparticle packing time, allowing for larger-sized nanoparticles to form. By adding hydrophobic species within the solvent phase and hydrophilic species within the aqueous phase, we have successfully encapsulated diverse species, such as albumin and the fluorescent dye Coumarin 6 (*11*). The high loading efficiency of our lipid entrapment process translates to high signal to noise ratios compared relative to individual, non-encapsulated species, and permits the delivery of higher concentrations of therapies or imaging agents in discrete packets. SLN can be engineered to bear multiple surface functionalities, permitting their usage as conventional nanoparticles for site-specific targeting by means of charge or biomolecule-assisted conjugation (*11*). Cationic, neutral, anionic, and bioactive interfaces have been constructed on fSLN surfaces *via* layer-by-layer assembly. The process of formulating SLN requires no surfactants or emulsifying agents, and all solvents are removed by extensive dialysis following SLN formulation. In past work, it was observed that negatively-charged fSLN bearing a polystyrene sulfonate (PSS) polymer surface, as opposed to other surfaces exhibiting cationic charges, exhibited interactions with bovine aortic endothelial cell (BAEC) membranes which facilitated internalization (*11*). In this report, we expand upon previous studies to widen the scope of constructs that can be encapsulated within fSLN for evaluation as a multimodal device, and to investigate the mechanism and dynamics of fSLN internalization within cells.

Methods

Synthesis and characterization of fSLN

fSLN were synthesized using a modified phase inversion technique as previously-described (*11*). In this process, a 500 μL aqueous phase is prepared consisting of hydrophilic moieties for encapsulation, along with the stabilizing polymer PSS (0.1%, MW = 70,000, Sigma), confers sufficient dispersion and water solubility upon resulting fSLN. This phase is combined with a 500 μL anhydrous organic phase consisting of N-methyl pyrrolidone:acetone = 70:20, with the remainder of volume consisting of hydrophobic encapsulants in DMSO. Hydrophilic encapsulants studied were 1 mg of 20 nm fluorescein isothiocyanate (FITC)-dextran-coated superparamagnetic iron oxide nanoparticles (SPIO, Micromod Partikletechnologie GmbH), and/or 1 μM 1.4 nm streptavidin-Alexa Fluor 594-conjugated gold colloids (Nanoprobes, Inc.). Hydrophobic species encapsulated included 1 μM quantum dot nanocrystals (Evident Technologies) dialyzed into DMSO, and/or 1 μM paclitaxel (Sigma) in DMSO. fSLN-QD-SPIO were produced by incorporating 1 mg and 1 μM doses of SPIO and QD, respectively, in the reaction mixture, in order to investigate multimodality. fSLN were concentrated as necessary using a Pall Nanosep spin column filtration device, MWCO = 10K using distilled water or PBS. Unencapsulated (free) SPIO or QD were phase-separated and removed by Pasteur pipette. Organic solvents or low molecular weight compounds (gold, paclitaxel) were removed by dialysis into double-distilled water or PBS using 25K regenerated cellulose dialysis columns for 2 hrs. followed by overnight dialysis in 100K MWCO columns (Spectrum Laboratories).

The fluorescence (intrinsic or dye-labeled) of all encapsulants enabled the determination of encapsulation efficiency by fluorescence spectrophotometry using a Nanodrop ND-3300 and fitting to standard curves of encapsulants. fSLN bearing no payload was processed under identical parameters and used as a control. Encapsulation efficiency was determined for fSLN-QD, fSLN-SPIO, fSLN-paclitaxel and fSLN-gold by determining the ratio of encapsulated species to total species originally present in the reaction mixture prior to phase inversion. Samples were analyzed in triplicate. fSLN were further characterized by dynamic light scattering analysis on a Beckman-Coulter DELSA 440SX particle zetasizer, and by fluorescence microscopy using a Nikon TE2000U inverted fluorescence microscope equipped with dye and QD-matched excitation and bandpass emission filters. Transmission electron microscopy (TEM) was performed on a Phillips CM-12 at 80 keV. fSLN were pipetted 1:1 with a solution of pure ethanol on Formvar grids and dried. Staining with 5% phosphotungstic acid was performed to stain solid lipid in negative relief.

Flow cytometry and fluorescence microscopy

Bovine aortic endothelial cells were cultured at passages 4-6 in DMEM with 10% FBS and 1% pencillin-streptomycin at 37°C, 5% CO_2. The human cervix carcinoma cell line, HeLa (American Tissue Type Culture Collection # CCL-2), and a mammary carcinoma line, 4T1 (gift of Dr. Jack Virostko, Vanderbilt Institute of Imaging Science), were cultured in the same medium and under the same conditions.

HeLa cells were cultured in 6-well microplates or 4-well chambered slides (Lab-Tek II, Nalge Nunc) to 80% confluency. For flow cytometric analysis of fSLN-QD uptake, cells were incubated with the fSLN equivalent of 100 nM QD emitting at 580 nm for 30 min at 37°C. To block endocytosis, cells were pre-incubated at 45 min. at 4°C and then incubated with fSLN-QD at the same temperature for 30 min. Following incubation cells were rinsed three times in HBSS, pH = 7.4. These incubation steps were also repeated with Qtracker QD-loading reagent (Invitrogen) according to manufacturer's instructions. Cells were detached with 0.25% trypsin-EDTA, which also served to remove surface-bound fSLN. Cells were pelleted at 400 X g, 5 min., and rinsed once and resuspended in HBSS for flow cytometry. Cells were analyzed on a LSR II flow cytometer (BD Biosciences) equipped with a UV laser and a 585/42 nm bandpass emission filter to detect QD. Unlabeled cells were used as a control. This experiment was performed in triplicate.

For cell cycle analysis, HeLa were incubated with 10 nM fSLN-paclitaxel, drug alone (in DMSO), or empty fSLN for 24 hrs. Cells were then rinsed thrice in HBSS, trypsinized, and fixed with ice-cold 70% ethanol for 2 hrs. at -20°C. The cells were rinsed in HBSS and pelleted. The pellet was resuspended in 1 mL of 50 μg/mL propidium iodide and 50 μL of 10 μg/mL RNAse A (Sigma) for 12 hr. at 4°C and analyzed on a FACSCalibur flow cytometer (BD Biosciences). Data was analyzed using FlowJo 7.2 (Treestar Software). For cell cycle analysis, the distribution of cell cycle for each population was determined using the Watson pragmatic fitting module incorporated in the software. 10,000 cells of each population were analyzed. To determine cell viability, cells were stained with the LIVE/DEAD single color fixable green kit (Invitrogen) and analyzed according to manufacturer instructions.

For fluorescence microscopy, HeLa were incubated with 10 nM fSLN-QD were fixed in 4% paraformaldehyde in PBS, quenched with 100 mM glycine in PBS, and coverslipped using Cytoseal 60 (Richard-Allan Scientific). Samples were imaged using a Nikon TE2000U inverted fluorescence microscope. For imaging of fSLN bearing Alexa Fluor 594-conjugated gold colloids, cells were incubated with 100 nM fSLN-gold or gold colloids alone as a control for 30 min. at 37°C. Cells were rinsed thrice in HBSS, and imaged using the same procedure.

For qualitative light microscopic analysis of fSLN-QD-SPIO uptake in HeLa cells, cells on chambered slides were incubated with the fSLN equivalent of 0.25 mg SPIO nanoparticles for 60 min at 37°C. 0.25 mg dextran-coated SPIO was incubated for 60 min. for comparison with fSLN-SPIO and 24 hrs. as a positive control. Cells were then rinsed and fixed. Samples were stained using Perls' Prussian Blue stain according to manufacturer instructions (Sigma). Cells incubated with fSLN-gold or fSLN-gold-SPIO (using dosage for fSLN-gold) were stained with the gold colloid detection reagent GoldEnhance for qualitative light microscopic analysis (following the Prussian Blue stain in multimodal samples).

Magneto-optical fSLN imaging

For magnetic resonance imaging, four samples containing a pellet of 1 X 10^5 cells (in Eppendorf tubes) were placed in a custom-built holder and aligned so that the pellet (400 X g, 5 min.) of each sample was in approximately the same plane. Samples were then imaged at bore temperature (20 ˚C) using a 7.0-T, 16-cm bore Varian Inova spectrometer (Varian Inc., Palo Alto, CA). A 63-mm inner diameter quadrature volume coil (Doty Scientific, Columbia, SC) was used for RF transmission and reception.

For each set, a single 2-mm slice just above the pellet was chosen from T_2-weighted scout images for subsequent imaging. T_2 measurements were then made using a single-slice, multiple spin-echo sequence (*13*) with an echo spacing (ΔTE) = 7 ms, repetition time (TR) = 2 s, number of echoes (NE) = 16, field of view = 40 × 40 mm^2, acquisition matrix = 64 × 64, in-plane resolution = 625 × 625 μm^2, acquisition bandwidth = 51.8 kHz, and number of averages (NEX) = 2. Spoiler gradients were placed about each $90_x180_y90_x$ broadband composite refocusing pulse (*14*) in an alternating and descending fashion (*13*) in order to remove signal from unwanted coherence pathways. The spoiler gradients were calculated so as to cause a minimum phase dispersion of $\pi/2$ across one slice thickness, which was found to be sufficiently large to remove stimulated echo artifacts within the decay curve.

T_1 measurements were made in the same slice using the multiple flip angle approach (*15*), in which a total of four gradient echo images were acquired using excitation flip angles (θ) of 5, 10, 20, or 40°. Additional imaging parameters included TE = 2.6 ms, repetition time (TR) = 50 ms, prescan dummy scans = 100 (to ensure steady-state was reached prior to acquisition), field of view = 40 × 40 mm^2, acquisition matrix = 64 × 64, in-plane resolution = 625 × 625 μm^2, acquisition bandwidth = 50 kHz, and number of averages (NEX) = 8.

The multiple-spin echo data, $M_\perp(\mathrm{TE})$, were used to generate T_2 maps by fitting data from each voxel to

$$M_\perp(\mathrm{TE}) = M_0\,\mathrm{e}^{-\mathrm{TE}/T_2} \tag{1}$$

where M_0 represents the equilibrium magnetization and TE the echo times used during acquisition. The multiple flip angle data, $M_\perp(\theta)$, were used to generate T_1 maps by fitting data from each voxel to

$$M_\perp(\theta) = M_0\,\frac{(1-e^{-\mathrm{TR}/T_1})\sin\theta}{1-e^{-\mathrm{TR}/T_1}\cos\theta} \tag{2}$$

where TR and θ represent the repetition time and excitation flip angles used during acquisition, respectively. All fitting was performed using the nonlinear Levenberg-Marquardt optimization algorithm (*16*).

Following magnetic resonance imaging, cell pellets and a gradient of fSLN-QD-SPIO suspensions were imaged using an IVIS 200 fluorescence imaging system (Caliper Life Sciences) with filters appropriate for QD, using background subtraction to remove autofluorescence. Empty fSLN incubated with cells were used as a control.

Results and Discussion

fSLN-PSS were capable of encapsulating quantum dot nanocrystals (2.4 nm, **Figure 1**), gold colloids (1.4 nm), iron oxide nanoparticles (SPIO, 20 nm), and/or the anticancer drug paclitaxel (**Table 1**). The encapsulation of hydrophobic compounds was relatively more efficient. The mean size of fSLN-QD as determined by dynamic light scattering analysis was 111 ± 8.6 nm for >65% of the distribution of particles. The remaining distribution of nanoparticles post fSLN synthesis was typically a lipid aggregate easily removed by 0.8/0.2 μm series syringe filtration. Using the same process parameters, less than 10% differences in hydrodynamic radius between fSLN bearing varying cargoes, including multimodal nanoparticles (QD-SPIO), were observed by dynamic light scattering analysis. These observations suggest that the hydrophobic lipid packing which occurs upon phase inversion produces similarly-sized nanoparticles, regardless of the encapsulated species.

Table 1. Encapsulation Efficiencies for fSLN formulations

fSLN formulation	**Encapsulation Efficiency (%, n = 3)**
fSLN-QD	40.23 ± 7.18
fSLN-Gold	46.34 ± 8.57
fSLN-Paclitaxel	65.73 ± 7.41
fSLN-SPIO	22.11 ± 3.37

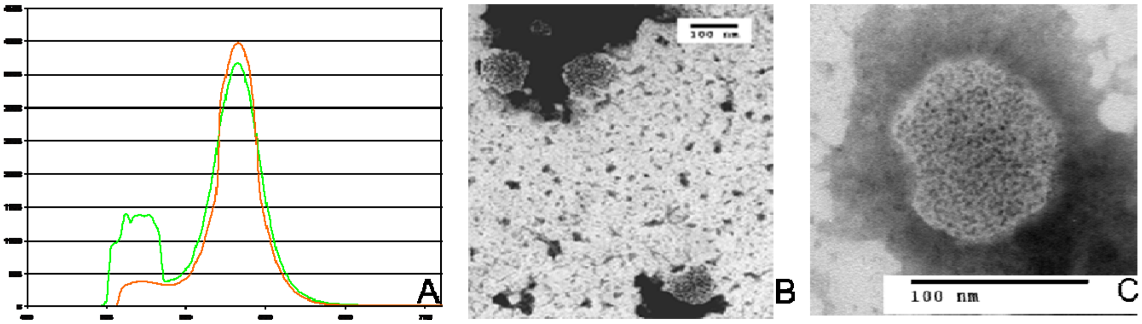

Figure 1. Fluorescence spectroscopy and transmission electron microscopy of fSLN. (A) fSLN-QD-PSS (orange) can be surface functionalized with PLL (green, FITC-labeled) without alteration in QD fluorescence emission profiles. (B-C) Low magnification (66000X) and high magnification (176000X) TEM of fSLN-QD-PSS.

Within a 30 min. incubation period, fSLN internalized within HeLa cell membranes as determined by flow cytometric analysis (**Figure 2A**). Internalization of fSLN was only slightly reduced at 4°C cell pre-incubation rather than blocked, suggesting that fSLN can enter cytoplasmic space without complete dependence on active transport. The slight reduction in internalization could be due to decreased plasma membrane fluidity, which would reduce lipid-lipid interactions between the nanoparticle and cell membrane. In contrast, the quantum dot endosomal-loading agent, Qtracker, which translocates nanocrystals across membranes *via* cationic oligoarginine peptides (*17*), did not internalize within cells appreciably at 4°C (**Figure 2A**). Co-incubation of cells with Qtracker and fSLN bearing 580 nm-emitting quantum dots revealed distinct localization within the cytoplasm (**Figure 2B**). These data collectively reveal that fSLN may be capable of membrane translocation to the cytosol without inclusion and sequestration in endosomal compartments, making subcellular targeting possible. Our approach achieves nanoparticulate internalization within cells without cationicity, which may complex electrostatically with negatively-charged cell surface proteins within the cell and possibly alter their function or availability within the cell. Viability of HeLa treated with fSLN-QD for 2 hrs. was 88 ± 3 %, comparable to untreated cells (92 ± 2 %) and empty fSLN-treated cells (90 ± 5 %).

fSLN successfully delivered gold colloids within HeLa cells as determined by light and fluorescence microscopy (**Figure 2C**). Colloids exhibited a diffuse cytoplasmic and cell membrane localization when delivered by fSLN, but did not translocate cell membranes efficiently without lipids (**Figure 2D**). fSLN may therefore be a useful carrier for gold colloids in photothermal ablation applications (*18, 19*), or as a computed tomography x-ray (*20*) or electron microscopic contrast agent (*21*).

SPIO were also effectively delivered into HeLa cells within 1 hr post-incubation (**Figure 2E**). However, when dextran-coated SPIO were incubated with HeLa cells for the same interval, little internalization was indicated by Prussian Blue staining (**Figure 2F**). Thus, fSLN enable rapid translocation of compounds incapable of penetrating cell membranes alone.

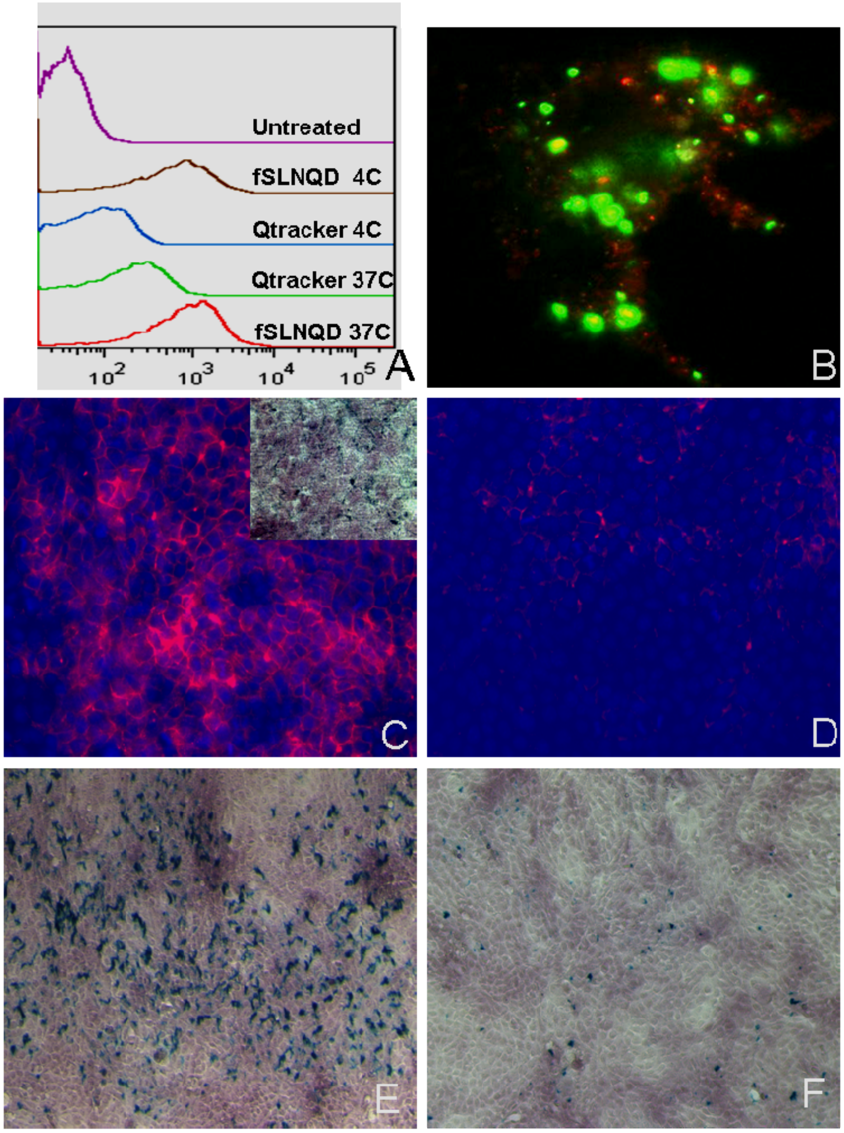

Figure 2. Flow cytometric, fluorescence, and light microscopic characterization of multimodal fSLN internalization in HeLa cells. (A) fSLN translocation into HeLa is largely energy-independent. (B) 200X magnification of distinct localization of fSLN-QD580 (red) and endosome-marking Qtracker cationic peptide-based conjugates, which aggregate in the endosomes (green). (C-D) Alexa Fluor 594-labeled gold colloid internalization in DAPI-labeled HeLa. (C) fSLN-gold, (D) gold colloids alone at equivalent concentration. Inset (C) Goldenhance light microscopic enhancement of gold colloids in HeLa cells (charcoal regions). Magnification 50X. (E-F) Prussian blue staining of fSLN-SPIO (E) and SPIO given at equivalent dose and incubation time (60 min.) in HeLa cells, counterstained with nuclear fast red. Magnification 50X.

fSLN efficiently delivered SLN-paclitaxel into HeLa cells for induction of cell cycle arrest in G2 phase (**Table 2**), comparable to free drug. Nanoparticles bearing dye-labeled paclitaxel were visible in the cytosol within 30 min. of incubation (**Figure 3**). 24 hrs. post-incubation, a marked increase in the percentage of cycling cells in the G2 phase was observed, consistent with literature reporting the timecourse of paclitaxel-induced mitotic arrest (*22*). Therefore, fSLN can potentially be utilized as a drug delivery vehicle in conjunction with imaging agents to visualize uptake and/or biodistribution. Future studies are warranted to investigate relative drug formulation efficacy when combined with nanoparticles.

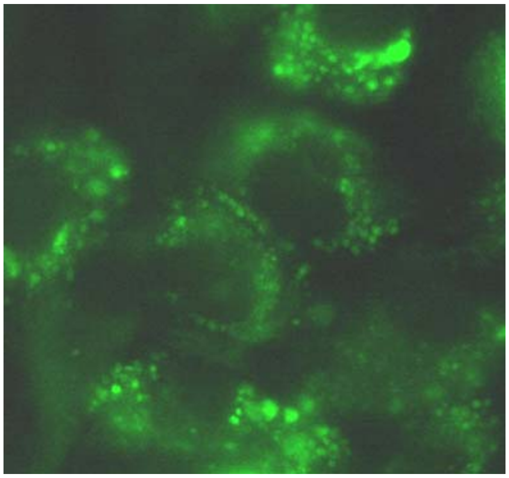

Figure 3. Fluorescence micrograph (magnification 100X) of HeLa stained with Oregon Green 488-loaded fSLN.

Table 2. Efficacy of 10 nM fSLN-paclitaxel compared to drug alone in arresting G2/M phase in HeLa cells following 24 hr. incubation

Sample	**%G1**	**%G2**
Untreated	37.08	23.52
fSLN	35.07	22.12
fSLN-paclitaxel	21.88	49.57
Paclitaxel	17.99	45.61

The multimodality of fSLN was specifically-investigated by translocating quantum dots and iron oxide nanoparticles within the same fSLN vehicle across 4T1 mammary carcinoma cells. This tumor cell line was selected due to its highly-metastatic potential. Imaging modalities to track tumor cell extravasation and metastasis with the aid of contrast agents are therefore a likely application for fSLN targeting. Within the same cell pellet following rinsing and trypsinization steps to detach cell surface-bound proteins which might adsorb fSLN nonspecifically, both magnetic resonance contrast, in the form of shortening of T2 relaxation, as well as optical contrast *via* QD fluorescence, was achieved (**Table 3-4**, **Figure 4**). Loading of fSLN-SPIO-QD was achieved within one hour, whereas to achieve the same T2-weighted contrast using conventional, dextran-coated SPIO, a 24 hr. overnight loading period was required (**Table 4**). Incubation of dextran-coated SPIO with 4T1 cells for 1 hr. without fSLN did not result in significant uptake, similar to HeLa cells. Negative enhancement of T2-weighted images was proportional to fSLN-SPIO-QD loading concentration, but fSLN-QD did not affect T2 relaxation as compared to unlabeled cells (**Table 4**). QD fluorescence in fSLN-SPIO-QD was reduced compared to fSLN-QD but remained detectable by optical imaging (**Figure 4A**), suggesting that a balance between magnetic resonance contrast and optical contrast can be achieved by judicious selection of starting concentrations of each reagent in fSLN synthesis. fSLN should therefore be considered as a useful device for the safe, rapid loading of multimodal nanostructures into cells.

Table 3. Relaxation measurements acquired (mean ± SD) for determination of relaxivity. Amount corresponds to mg of SPIO in each cell pellet.

fSLN-QD-SPIO (mg)	0.031	0.095	0.117	0.247
T_1 (ms)	1287.3 ± 78.2	1008.5 ± 98.9	816.1 ± 43.1	747.0 ± 43.7
T_2 (ms)	67.8 ± 2.9	43.1 ± 5.1	37.4 ± 8.8	26.0 ± 6.5

Table 4. Relaxation measurements acquired for 4T1 cell pellets

Sample	Untreated	SPIO 24 hr.	fSLN-QD-SPIO	fSLN-QD
T_1 (ms)	2108.9 ± 90.3	1223.9 ± 72.1	806.4 ± 121.9	2393.9 ± 83.1
T_2 (ms)	127.1 ± 1.9	78.4 ± 8.0	65.7 ± 16.0	117.9 ± 4.0

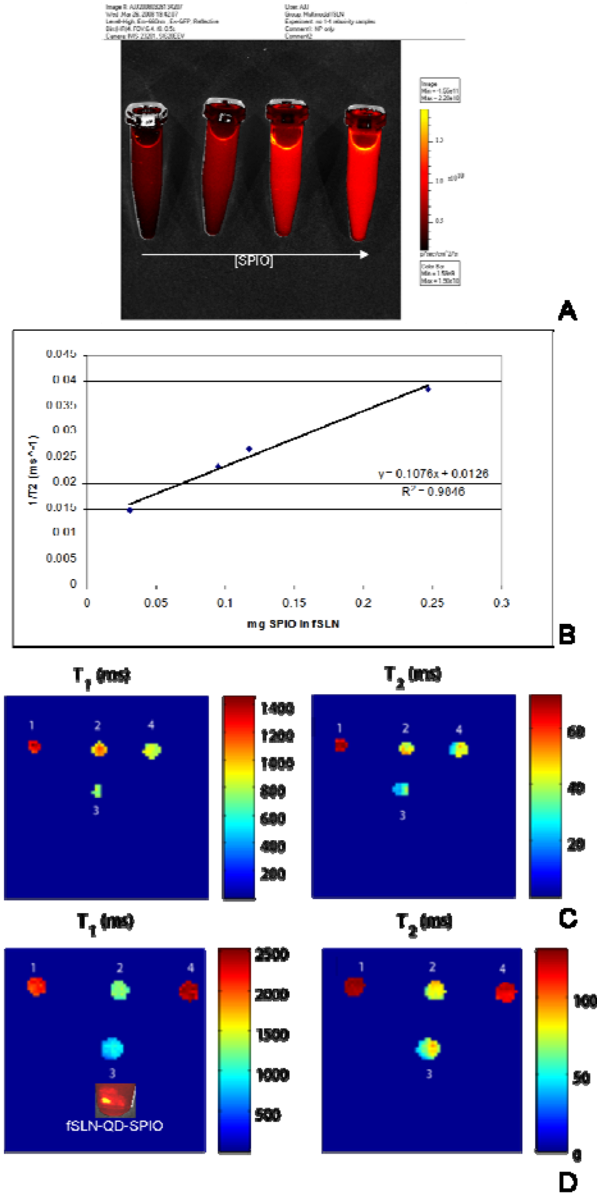

Figure 4. Multimodal imaging of 4T1 using fSLN-SPIO-QD. (A) SPIO do not significantly quench QD emission and fluorescence is proportional to fSLN concentration. (B) T2 shortening in 4T1 cell pellets is a function of fSLN-SPIO-QD concentration. (C) T1 and T2 maps of fSLN-QD-SPIO in 4T1 cell pellets corresponding to Table 3. (D) T1 and T2 maps of fSLN-QD-SPIO, SPIO (24 hr. incubation), untreated, and fSLN-QD-treated 4T1 cell pellets corresponding to Table 4.

Multimodality and high loading volume are unique features of fSLN. The incorporation of diverse imaging agents and therapeutics within a single, targeted package should expand the scope of clinical approaches. For example, lower-resolution but noninvasive imaging modalities such as MRI could be combined with optical imaging for guidance in tissue biopsies and histological immunofluorescence analysis. Furthermore, the encapsulation of many nanoparticles within one functional nanoscale carrier should enable signal to noise amplification strategies for detection of proteins for *in vitro* diagnostics using flow cytometry, or *in vivo* imaging using optical imaging, as example applications whereby detection of biomolecules in low abundance is critical to diagnosis. Furthermore, the entrapment of high concentrations of cytotoxic drugs within nanoscale packets should result in enhanced therapeutic efficacy if the carrier can be appropriately site-directed.

Current strategies for translocating compounds of varying physicochemical properties (e.g. hydrophilicity, molecular weight, charge) across membranes have largely been limited to the use of cationic transfection reagents such as polymers or peptides. In this work we demonstrate for the first time that an anionically-charged, biocompatible nanoparticle composed of a solid lipid matrix is capable of rapidly delivering various imaging agents and therapeutics into cells. Negatively-charged compounds are typically incapable of penetrating plasma membranes without dependence on receptor-mediated or other types of endocytosis, making our findings a novel result and expanding the range of currently-limited techniques for delivering compounds to subcellular destinations. Given the wide range of encapsulants tested in this work, it is likely that other therapeutics and contrast agents are also compatible with the encapsulation process, including Gadolinium chelates and radiotracers. We hypothesize that the negative charge of fSLN afforded by PSS surface entrapment electrostatically-perturbs interactions of the nanoparticle with cell surface proteins, thereby favoring lipid-lipid interactions. The negative charge of fSLN, besides its potential role in promoting energy-independent nanoparticle translocation, may also be favorable for preserving cell viability and function as a result of reducing the likelihood of cytoplasmic protein adsorption to the fSLN surface. However, charge alone may not be responsible for the membrane translocation capabilities of fSLN, as PAA-coated fSLN did not translocate across membranes but rather were localizaed among cell borders (*11*). Our process additionally features size-tunability and amenability to surface functionalization of targeting ligands, making fSLN a versatile candidate for a wide range of pharmaceutics and imaging agents.

References

(1) Morris, M. C., Depollier, J., Mery, J., Heitz, F., and Divita, G. (2001) A peptide carrier for the delivery of biologically active proteins into mammalian cells. *Nat Biotechnol 19*, 1173-6.

(2) Zorko, M., and Langel, U. (2005) Cell-penetrating peptides: mechanism and kinetics of cargo delivery. *Adv Drug Deliv Rev 57*, 529-45.

(3) Duan, H., and Nie, S. (2007) Cell-penetrating quantum dots based on multivalent and endosome-disrupting surface coatings. *J Am Chem Soc 129*, 3333-8.

(4) Guo, X., and Szoka, F. C., Jr. (2003) Chemical approaches to triggerable lipid vesicles for drug and gene delivery. *Acc Chem Res 36*, 335-41.

(5) Huang, K., Voss, B., Kumar, D., Hamm, H. E., and Harth, E. (2007) Dendritic molecular transporters provide control of delivery to intracellular compartments. *Bioconjug Chem 18*, 403-9.

(6) Hasegawa, U., Nomura, S. M., Kaul, S. C., Hirano, T., and Akiyoshi, K. (2005) Nanogel-quantum dot hybrid nanoparticles for live cell imaging. *Biochem Biophys Res Commun 331*, 917-21.

(7) Ayame, H., Morimoto, N., and Akiyoshi, K. (2008) Self-Assembled Cationic Nanogels for Intracellular Protein Delivery. *Bioconjug Chem*.

(8) Lai, F., Sinico, C., De Logu, A., Zaru, M., Muller, R. H., and Fadda, A. M. (2007) SLN as a topical delivery system for Artemisia arborescens essential oil: in vitro antiviral activity and skin permeation study. *Int J Nanomedicine 2*, 419-25.

(9) Muller, R. H., Petersen, R. D., Hommoss, A., and Pardeike, J. (2007) Nanostructured lipid carriers (NLC) in cosmetic dermal products. *Adv Drug Deliv Rev 59*, 522-30.

(10) Souto, E. B., and Muller, R. H. (2006) The use of SLN and NLC as topical particulate carriers for imidazole antifungal agents. *Pharmazie 61*, 431-7.

(11) Jayagopal, A., Sussman, E. M., and Shastri, V. P. (2008) Functionalized Solid Lipid Nanoparticles for Transendothelial Delivery. *IEEE Trans Nanobioscience 7*, 28-34.

(12) Sussman, E. M., Clarke, M. B., Jr., and Shastri, V. P. (2007) Single-step process to produce surface-functionalized polymeric nanoparticles. *Langmuir 23*, 12275-9.

(13) Poon, C. S., and Henkelman, R. M. (1992) Practical T2 quantitation for clinical applications. *J Magn Reson Imaging 2*, 541-53.

(14) Levitt MH, R. F. (1981) Compensation for pulse imperfections in NMR spin-echo experiments. *J Magn Reson Imaging 43*, 65-80.

(15) Gupta, R. (1981) A new look at the method of variable nutation angle for the measurement of spin-lattice relaxation times using FT NMR. *J Magn Reson Imaging 25*, 231-235.

(16) Moré, J. (1977) The Levenberg-Marquardt Algorithm: Implementation and Theory, in *Numerical Analysis* (Watson, G. A., Ed.) pp 105-116, Springer Verlag.

(17) Futaki, S., Suzuki, T., Ohashi, W., Yagami, T., Tanaka, S., Ueda, K., and Sugiura, Y. (2001) Arginine-rich peptides. An abundant source of membrane-permeable peptides having potential as carriers for intracellular protein delivery. *J Biol Chem 276*, 5836-40.

(18) Hirsch, L. R., Stafford, R. J., Bankson, J. A., Sershen, S. R., Rivera, B., Price, R. E., Hazle, J. D., Halas, N. J., and West, J. L. (2003) Nanoshell-mediated near-infrared thermal therapy of tumors under magnetic resonance guidance. *Proc Natl Acad Sci U S A 100*, 13549-54.

(19) Loo, C., Lowery, A., Halas, N., West, J., and Drezek, R. (2005) Immunotargeted nanoshells for integrated cancer imaging and therapy. *Nano Lett 5*, 709-11.

(20) Kim, D., Park, S., Lee, J. H., Jeong, Y. Y., and Jon, S. (2007) Antibiofouling polymer-coated gold nanoparticles as a contrast agent for in vivo X-ray computed tomography imaging. *J Am Chem Soc 129*, 7661-5.

(21) Inamura, M., Itakura, M., Okamoto, H., Hoka, S., Mizoguchi, A., Fukazawa, Y., Shigemoto, R., Yamamori, S., and Takahashi, M. (2006) Differential localization and regulation of stargazin-like protein, gamma-8 and stargazin in the plasma membrane of hippocampal and cortical neurons. *Neurosci Res 55*, 45-53.

(22) Sui, M., Dziadyk, J. M., Zhu, X., and Fan, W. (2004) Cell cycle-dependent antagonistic interactions between paclitaxel and gamma-radiation in combination therapy. *Clin Cancer Res 10*, 4848-57.

CHAPTER VII

CONCLUSIONS AND FUTURE WORK

This dissertation is composed of four manuscripts which define a framework for incorporating nanoscale surface engineering for enhanced functionality in bioimaging and drug delivery. The main functional advances in nanotechnology made possible by this work relate to enhanced targeting (cell surface and intracellular) capabilities, and the development of multifunctional devices. Chapters III and IV were concerned with the goal of improving nanoparticle imaging agent targeting for long-term *in vivo* imaging of disease. In chapter III, insight into the imaging of diabetes and ocular inflammation (uveitis) was provided using a noninvasive retinal imaging technique in conjunction with quantum dot-antibody conjugates (QD-Mab) that were engineered for high specificity and circulation lifetime. While only QD-Mab were the imaging agent in these studies, it is likely that most other imaging agents would benefit from the immune-shielding techniques used in this Aim, such as iron oxide nanoparticles, microbubbles, or gold nanoparticles for magnetic resonance, ultrasound, or x-ray contrast agents, respectively. Future work will be focused on molecular expression of various inflammatory molecules using this technique in diabetes and atherosclerosis. In addition, studies are currently underway to elucidate the role of Fc-blockade in reducing liver and splenic macrophage uptake of QD-Mab *in vitro* and *in vivo*. The implications of this study may be significant for the design of Mab-based therapeutics, many of which are currently in clinical usage. In chapter IV, QD were coated with a cell-penetrating peptide (CPP), to confer cytoplasmic loading capabilities upon QD, which themselves are not capable of crossing cell membranes. By retaining QD in subcellular space, labeled cells can interact with other cells or biomolecules without potential steric hindrance from QD-Mab conjugates, and QD cannot be shed from the membrane surface as part of normal membrane shuffling/recycling functions, for long-term imaging applications such as the imaging of cancer metastasis. Future work is directed toward the elucidation of mechanism of CPP internalization into cells, and whether internalization can occur independently of endocytic mechanisms. Should the CPP evade the endosomal pathway, subsequent work will be directed toward the targeting of QD-CPP toward subcellular destinations for bioimaging and targeted therapeutics.

Chapters V and VI explore features of functionalized solid lipid nanoparticles (fSLN) relevant for imaging and drug delivery as proposed in Aim 2. Surface engineering approaches for the impartation of multiple functionalities into one device, and for the conferring of targeting capabilities upon the device. In Chapter V, it was observed that fSLN could be tuned for the translocation of compounds such as proteins either across endothelial barriers or within endothelial cells by controlling surface information. Specifically, a composite surface, PSS-PLL-Heparin, when coated on fSLN by simple layer-by-layer assembly, facilitated transendothelial transport across endothelial barriers, whereas PEG blocked transport completely. Interestingly, the PSS coating facilitated intracellular transport, prompting the subsequent study of this fSLN formulation in Chapter VI. This chapter expands upon the potential of multimodal fSLN by describing the construction of various fSLN-PSS formulations, including multimodal fSLN bearing both QD and SPIO, and begins the elucidation of the fSLN-PSS intracellular transport mechanism. Future work relevant to Aim 2 is directed toward the *in vivo* investigation of fSLN-PSS-PLL-Heparin, in the context of transendothelial barrier delivery of imaging agents and therapeutics. Should this formulation be capable of blood-brain barrier translocation, this would be a significant result in the field of nanomedicine as this barrier complicates effective treatment. Furthermore, the studies of Chapter VI will be continued to generate statistically-robust data relating to fSLN internalization and the generation of magnetic resonance and optical contrast by these probes. In future work, alternative SPIO will be selected, as the commercially-available SPIO (Micromod GmbH) purchased for this study were degraded in the organic solvents used for encapsulating fSLN. Several methods for the synthesis of magnetite for solubility in both organic and aqueous phases have been reported, specifically those involving oleic acid as a surfactant. These SPIO will likely be evaluated in future applications due to enhanced solubility in both phases, which should translate toward higher encapsulation efficiencies. In order to evaluate fSLN as an effective drug carrier, extensive studies must be performed to determine therapeutic efficacy, encapsulation efficiency *via* HPLC, and evaluation of release profiles.

APPENDIX A

ANIMAL SUBJECTS

This appendix details the rat and mouse models used for studies in Aim 1, as well as relevant experimental details for each animal. All acquired video sequences have been archived on DVD and catalogued by date, corresponding to the dates of animal experimentation.

I. STZ-induced diabetic rat model and wild-type controls

All species are male, Long-Evans (Blue Spruce) rats from Harlan Sprague Dawley, Inc.

STZ treatment = 65 mg/kg intraperitoneally
QD-Mab injections included a QD565 isotype control Mab injection

Date	Age (Days)	STZ	Measurements
9/22/2004	111+	8/4/2004	Fluorescein/dextran angiography, acridine orange fluorography, PS/F quantitation
3/2/2005	111+	N	acridine orange fluorography
3/21/2005	111+	11/22/2004	QD-VCAM-1/ICAM-1/RP-1/PECAM-1
3/22/2005	111+	11/22/2004	QD-VCAM-1/ICAM-1/RP-1/PECAM-1
3/23/2005	111+	11/22/2004	QD-VCAM-1/ICAM-1/RP-1/PECAM-1
4/5/2005	111+	3/2/2005	QD-RP-1; nontargeted QD circulation kinetics
4/5/2005	111+	N	QD-VCAM-1/ICAM-1/RP-1/PECAM-1
4/14/2005	111+	11/23/2004	QD-CD45; flow cytometric analysis; leukostasis; rolling velocities
5/17/2005	111+	4/6/2005	QD-VCAM-1/ICAM-1/RP-1/PECAM-1
6/14/2005	111+	N	QD-VCAM-1/ICAM-1/RP-1/PECAM-1
7/6/2005	111+	6/21/2005	QD-VCAM-1/ICAM-1/RP-1/PECAM-1
7/13/2005	111+	6/21/2005	QD-VCAM-1/ICAM-1/RP-1/PECAM-1
8/1/2005	111+	N	QD-VCAM-1/ICAM-1/RP-1/PECAM-1
1/31/2006	111+	N	QD-VCAM-1/ICAM-1/RP-1/PECAM-1
2/28/2006	111+	N	QD-VCAM-1/ICAM-1/RP-1/PECAM-1
3/7/2006	111+	1/30/2006	QD-VCAM-1/ICAM-1/RP-1/PECAM-1
3/8/2006	111+	N	QD-VCAM-1/ICAM-1/RP-1/PECAM-1
3/29/2006	111+	1/30/2006	QD-VCAM-1/ICAM-1/RP-1/PECAM-1
4/14/2006	111+	1/30/2006	QD-VCAM-1/ICAM-1/PECAM-1
4/18/2006	111+	N	QD-VCAM-1/ICAM-1/RP-1/PECAM-1
10/4/2006	111+	N	FC BLOCKADE EXPERIMENT

II. Endotoxin-induced uveitis (EIU) rat model of ocular inflammation

LPS treatment = 200 ug LPS intraperitoneally
All species are male, Long-Evans (Blue Spruce) rats from Harlan Sprague Dawley, Inc.

Date	Age (Days)	LPS	Measurements
10/24/2006	111+	10/23/2006	QD-CD45/RP-1
10/24/2006	111+	10/23/2006	QD-CD45
10/24/2006	111+	N	QD-CD45
3/6/2007	91-100	3/6/2007	CD3, CD45, monocytes, dendritic cells
3/8/2007	91-100	3/6/2007	CD45, monocytes, dendritic cells
3/19/2007	91-100	N	CD45
4/30/2007	111+	N	CD45
5/1/2007	50-57	5/1/2007	CD45, RP-1, natural killer cells
5/3/2007	50-57	5/1/2007	RP-1, CD45, monocytes, natural killer cells

III. ApoE -/- mouse model of atherosclerosis

Path ID	Animal Type	Age (mos.)	Injections/Measurements
7885	Apo E -/-	7	QD/CD11b- 5 X 10^6 cells
7886	Apo E -/-	7	QD/CD11b- 5 X 10^6 cells
7887	Apo E -/-	7	QD/CD11b+ 300,000 cells
7931	Apo E -/-	12	QD/TCR+ and QD/CD11b+ 1 X 10^6 cells
7932	Apo E -/-	12	QD/CD11b+ 1 X 10^6 cells
7983	Apo E -/-	12	QD/CD11b+ 1 X 10^6 cells
7984	Apo E -/-	12	QD/CD11b+ 1 X 10^6 cells
8035	C57/BL6	12	QD/TCR+ and QD/CD11b+ 1 X 10^6 cells IVIS imaging
8036	Apo E -/-	12	QD/TCR+ and QD/CD11b+ 1 X 10^6 cells IVIS imaging
8037	C57/BL6	12	QD/TCR+ and QD/CD11b+ 1 X 10^6 cells IVIS imaging
8038	Apo E -/-	12	QD/TCR+ and QD/CD11b+ 1 X 10^6 cells IVIS imaging

APPENDIX B

IN VIVO IMAGING OF LEUKOCYTES IN ENDOTOXIN-INDUCED UVEITIS

Using the methods described in detail in Chapter III, quantum dots emitting at spectrally-distinct wavelengths were conjugated to antibodies against neutrophils (RP-1), dendritic cells, natural killer cells, and monocytes (mouse anti-rat, BD Biosciences). Endotoxin-induced uveitis was initiated by intraperitoneal injection of 200 µg of lipopolysaccharide in 50 and 90 day old Long-Evans male rats and imaged 24-48 hrs. post-injection. In addition, peripheral blood was drawn from a 90 day old wild-type rat for flow cytometric analysis. During *in vivo* imaging, RP-1 labeled neutrophils were identified in the retinal circulation as hyperfluorescent cells rolling along vessels, characteristic of EIU. Using spatial calibration based on the size of the rat optic disk, rolling velocities were determined for 10 neutrophils within 2 optic disc diameters and compared to literature values. The mean rolling velocity of QD-labeled neutrophils was 57.7 ± 7.3 µm/sec. This is somewhat close to the values of neutrophil rolling in EIU post-injection (24 hrs.) recorded by Miyamoto et *al. (1)*, which was 46.6 µm/sec. In future work, a greater sample size and wider range of animals will be employed to generate statistically-significant data. The *in vivo* findings suggest that QD-RP-1 can be used to quantify leukocyte rolling in vessels without significantly perturbing function.

As previously reported, RP-1 is upregulated on rat neutrophils in proportion to activation state. However, its role in inflammation has not been defined. QD-RP-1 was incubated at 100 nM doses to 1 X 10^6 Percoll density gradient-isolated neutrophils with or without 100 ng/mL LPS pre-treatment. As shown by FACS below (**Figure 1**), QD-RP-1 labeling was observed to be proportional to activation time. QD can therefore be harnessed as a biosensor to probe not just the presence or absence of a single cell type, but also cell function. *In vivo* imaging of QD-RP-1 labeled neutrophils at increasing intervals post-LPS injection were consistent with *in vitro* observations (**Figure 1**).

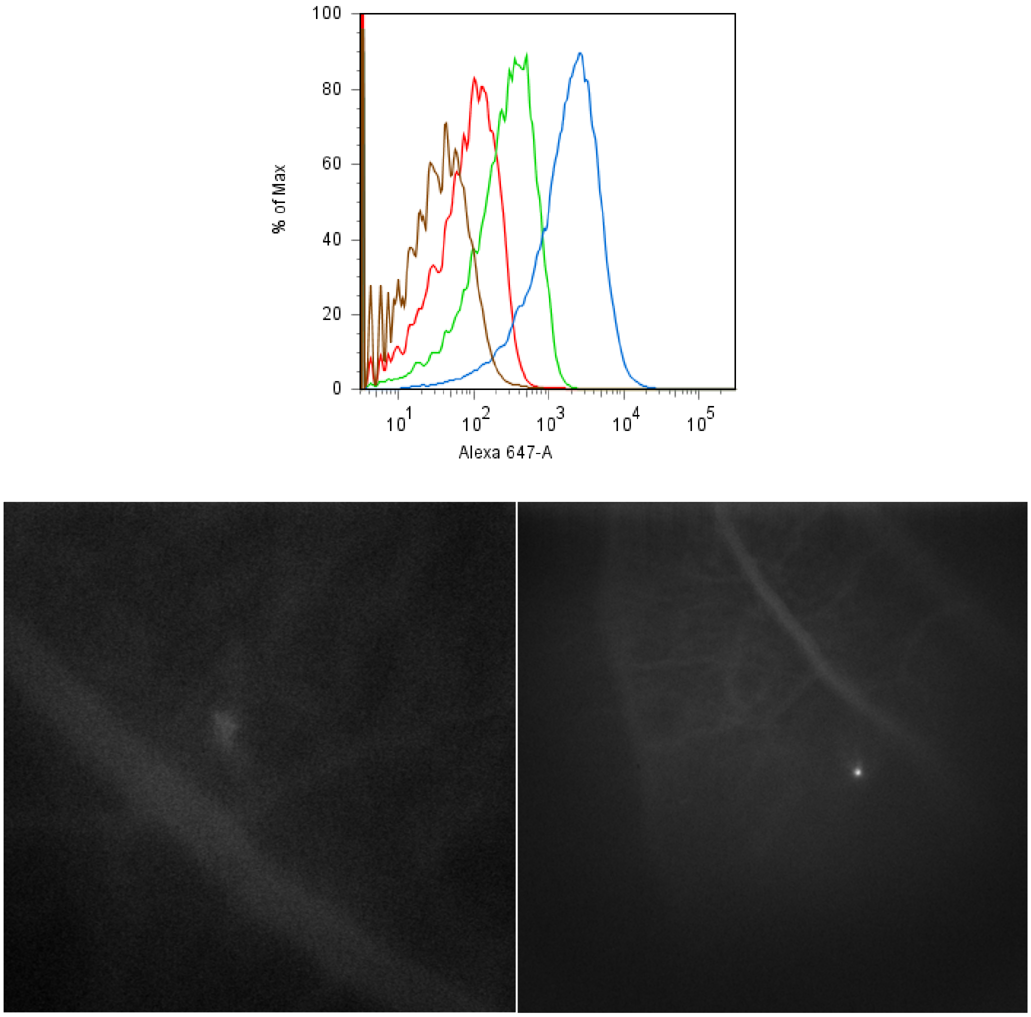

Figure 1. Top: QD655-RP-1 labeled neutrophils at 1 (red), 2 (green), and 3 (blue) hrs. post-LPS treatment. Brown – unlabeled cells. Fluorescence intensity was found to increase with increasing post-treatment times. Bottom: *In vivo* imaging of neutrophil 1 hr. (left) and 6 hrs. (right) post-LPS treatment. Greater intensity of labeled cells was qualitatively-apparent, particularly in slow-moving or stagnant neutrophils.

Using the *in vivo* imaging strategy outlined in Chapter III, other cell types were also imaged in EIU, including monocytes, dendritic cells, and natural killer cells. In 2 90-day old mice, it was observed that the 3-6 hr. post-injection timepoint featured a transient monocytic infiltrate, whereas 48 hrs. post-injection, dendritic cells appeared to be primarily recruited (**Figure 2**). These observations, while preliminary, underscore the need to characterize individual components of the immune response using multispectral imaging. Such observations may have a profound impact on the development of timely therapeutic interventions in inflammatory disease.

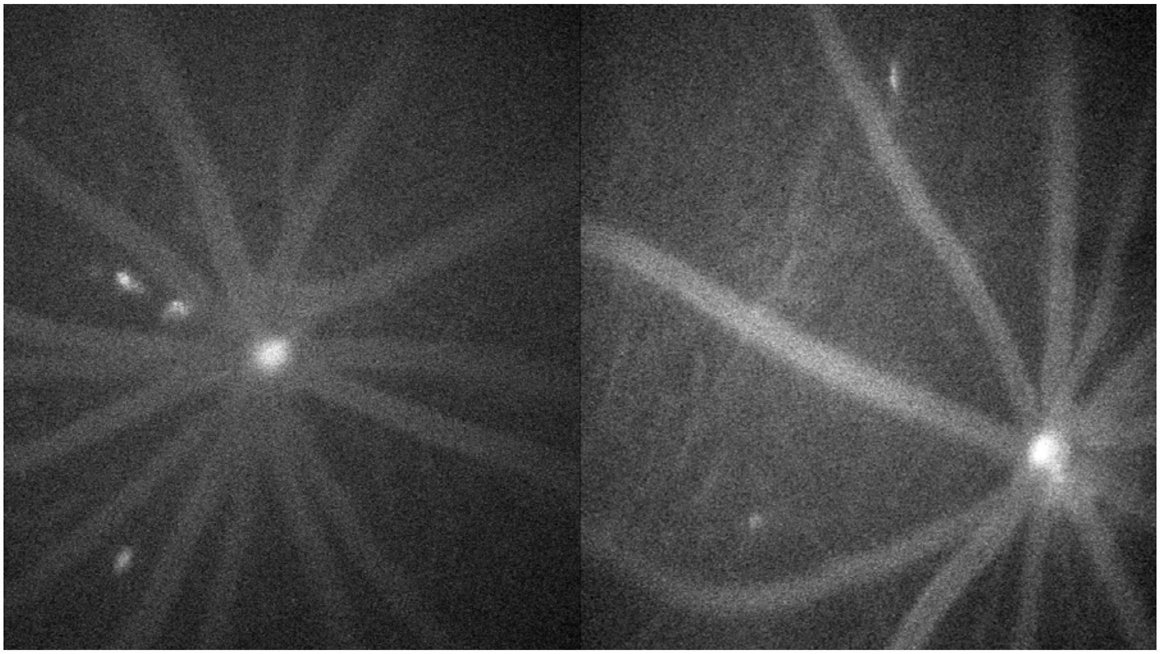

Figure 2. Left: Monocyte infiltrate at 3-6 hrs. post-LPS treatment in an EIU rat model. Right: Dendritic cell infiltrate 48 hrs. post-injection.

APPENDIX C

FUNCTIONALIZED POLYMERIC AND SOLID LIPID NANOPARTICLES FOR BIOMEDICAL APPLICATIONS

Ashwath Jayagopal[1]
Eric M. Sussman[1]
Frederick R. Haselton
V. Prasad Shastri

Department of Biomedical Engineering
Vanderbilt University
Nashville, TN
[1]These authors contributed equally to this manuscript

In: New Delivery Systems for Controlled Drug Release from Natural Polymers.

Eds. Nicholas Parris and Lin-Shu Liu, ACS Symposium Series, in press March 2008

Abstract

Solid Lipid Nanoparticles (SLN) bear significant potential as drug delivery systems and diagnostic probes. They constitute a promising alternative to polymeric and liposomal nanoparticulate formulations due to their efficient loading and stabilization of poorly soluble or instable compounds, high biocompatibility, and potential for scaling up production processes for pharmaceutical applications. To enhance the scope of their biomedical application, methods which enable simultaneous drug/probe entrapment and presentation of surface functionalities are desired. We have developed a process for the single-step formulation of functionalized polymeric nanoparticles with tunable size and narrow polydispersity (*1*). By incorporation of a polyelectrolyte or polymer within the aqueous phase, our process enables the surface engineering of diverse surface moieties upon a non-functionalized polymer backbone within a binary solvent system, via a phase inversion process. By substitution of a biocompatible coco-glyceride for the non-functionalized polymer in the organic phase, we have applied this strategy toward the formulation of surface functionalized SLN capable of entrapping physicochemically-diverse cargoes. We investigated the effect of process parameters on nanoparticle size, surface charge, and compound entrapment efficiency. Species to be encapsulated included fluorescent dyes, semiconducting nanocrystals, and paramagnetic nanoparticles. Surface moieties incorporated in the aqueous phase included PEG, amine groups and carboxyl groups for the bioconjugation of targeting ligands. Nanoparticles were characterized by laser light scattering, x-ray photoelectron spectroscopy (XPS), fluorescence spectrophotometry, electron microscopy, and fluorescence microscopy. Our studies demonstrate that the solvent composition can be varied to control nanoparticle hydrodynamic radius while maintaining a narrow polydispersity. Both hydrophilic and hydrophobic species can be efficiently entrapped within the lipid matrix to create targeted and stable high signal intensity diagnostic probes or concentrated drug carriers for biomedical applications. We anticipate the application of SLN toward magnetic resonance and fluorescence imaging, targeted chemotherapy, as well as the surface modification of biomaterials for tissue engineering strategies.

Introduction

Nanoparticulate delivery systems generally aim to safely and efficiently deliver therapeutic or diagnostic compounds to specific tissue sites, without degradation of the cargo that would limit its efficacy. Nanoparticles with solid lipid matrices, or solid lipid nanoparticles, (SLN) exhibit several key features which make them promising agents for the delivery of diagnostic probes or therapies *in vivo*. Among these are their capacity to entrap poorly water-soluble compounds, physical stability (remaining solid at physiologic temperatures and/or during storage), and biocompatibility (*2-4*). They are not limited by some of the challenges associated with current nanoparticulate drug delivery systems in research and clinical administration stages, including poly-lactide-co-glycolide nanoparticles (PLGA NP) and liposomes, which have been associated with acidic degradation of protein cargoes (*5*) and potentially low cargo loading and stability (*6*), respectively.

In order to expand the capabilities of SLN in medical imaging and drug delivery and to facilitate their clinical implementation, further work is warranted in the continued adaptation of laboratory-scale production processes for the pharmaceutical-scale, and the modifications of process parameters to control efficiency-critical properties of SLN, such as size and loading capacity. Furthermore, it is important that SLN be capable of bearing surface functionalities and/or functionally-diverse cargoes such as contrast agents and drugs, regardless of their physicochemical properties (e.g. hydrophilicity, size). Such a versatile carrier technology at the nanometer scale of biology would provide a template for the manufacture of a broad spectrum of drugs and imaging agents which work at the scale of biology.

We have developed a single-step process for the rapid synthesis of functionalized polymeric nanoparticles based on the polymers PLGA and poly-lactic acid (PLA) (*1*). The solvation core of this non-functionalized polymer backbone is specifically engineered such that addition of a polyelectrolyte or polymer-containing aqueous phase results in the instantaneous formation of a nanoparticle, the surface of which bears the aqueous moiety. We have adapted this process toward the surface engineering of SLN capable of entrapping various types of cargoes while at the same time bearing different surface functionalities. Our process obviates the need for surfactants, emulsifiers, and melting/cooling steps which are often involved in other nanoparticle synthesis methods. Tailoring of the solvent composition and presence of aqueous phase moieties in the process was found to have profound effects on the surface engineering and encapsulation features of the nanoparticulate system. We discuss the synthesis and characterization of polymeric and solid lipid NP and implications for biomedical applications such as drug delivery, imaging, and tissue engineering.

Materials and Methods

Materials

Poly (dl-lactide-co-glycolide) (PLGA, RG 503, MW=30,000) and poly (L-lactide) (PLA) MW = 70,000, inherent viscosity 1.20 dL/g in CHCl3) were purchased from Birmingham Polymers. PLGA and PLA were prepared for use by precipitation from methylene chloride (MeCl) in methanol. Tetrahydrofuran (THF), Toluene, MeCl, Acetone, and 1-Methyl-2-pyrrolidinone (NMP) were purchased from Sigma or Fisher Scientific in HPLC grades. HCl, NaOH, Fluorescein isothiocyanate-bovine serum albumin conjugate (FITC-BSA), Poly (styrene-4 sodium sulfonate) (PSS, MW = 70,000), poly (acrylic acid) (PAA, MW = 2000), poly (L-lysine hydrochloride) (PLL, MW=22,100), Fluorescein isothiocyanate PLL (FITC-PLL, avg. MW = 30,000) and poly (ethylene glycol) (PEG, MW=10,000) were purchased from Sigma. 4',6-diamidino-2-phenylindole (DAPI) in the form of

VECTASHIELD, an aqueous mixture of DAPI in a glycerol-containing suspension, was purchased from Vector Labs. Trypan Blue was purchased from Gibco. Softisan 100 was a gift from Sasol GmbH. Water soluble, 50nm silica magnetite nanoparticles were purchased from Micromod GmbH as a 10 mg/mL suspension in PBS. Cadmium Selenide-Zinc Sulfide (CdSe) semiconducting nanocrystals (EviDots) in toluene were purchased from Evident Technologies. 10K MWCO regenerated cellulose (RC) and 100K MWCO cellulose ester (CE) 6 mL capacity floating dialysis columns (Float-a-Lyzer) were purchased from Spectrum Laboratories and dialyzed overnight against 4L double distilled water (Millipore) to remove sodium azide preservative prior to use.

Methods

Polymeric Nanoparticle Synthesis

To prepare polymeric NP, an aqueous phase was added to an equal volume of PLGA or PLA polymer dissolved in a binary solvent system. THF:Acetone, MeCl:Acetone and MeCl:THF were selected as the binary solvent systems for polymeric NP synthesis. The volumetric ratio of the solvent pair was varied to investigate the effect of solvent polarity on nanoparticle formation. When surface functionalization was desired, the aqueous phase was supplemented with either a polyelectrolyte or a water-soluble polymer such as PEG, at a 0.5% concentration. Alternatively, the fluorescent dye DAPI was added to the aqueous phase at a 100 ug/mL concentration prior to phase inversion, after which the polymeric NP were dialyzed on 10K MWCO Float-a-Lyzers against double distilled water to remove non-entrapped dye.

Solid Lipid Nanoparticle Synthesis

To prepare SLN, Softisan 100 was dissolved in an anhydrous 80:20 mixture of NMP:Acetone as the binary solvent system at a concentration of 1%. To synthesize SLN bearing quantum dots (QD), 1 uL of a 1 mg/mL suspension of CdSe QD in toluene was added to the NMP/Acetone/Softisan mixture in a nitrogen-purged glove bag. An aqueous phase containing 1% PSS in ultrapure (100nm filtered) double-distilled water was prepared. To synthesize SLN bearing FITC-BSA/magnetite, the PSS-based aqueous phase was supplemented with 0.1% FITC-BSA and 100ug of paramagnetic, silica-capped iron oxide nanoparticles. The organic phase was rapidly infused into a scintillation vial containing the aqueous phase using a syringe accompanied by gentle shaking. Organic solvents were removed by dialysis against 4L ddH_2O in 10K MWCO RC Float-a-Lyzers in a low-speed stirring beaker for 2 hours. Next, excess polymer and FITC-BSA was removed by overnight dialysis against 4L ddH_2O in 100K MWCO CE Float-a-Lyzers with a complete change of dialysis buffer every 4 hours. For further surface functionalization of PLL, FITC-PLL was incubated at 4°C overnight with SLN-QD-PSS at a concentration of 1%, and dialysis against 4L ddH_2O using 100,000 MWCO CE Float-a-Lyzer was performed the following day to remove excess FITC-PLL.

Measurement of Polymeric and Solid Lipid Nanoparticle Hydrodynamic Radius and Zeta Potential

Polymeric NP were diluted by a factor of 15 in ddH_2O and adjusted to the desired pH for zetasizing analysis using either HCl and NaOH. Measurements of zeta potential and hydrodynamic radius were conducted in automatic mode on a Malvern Instruments Zetasizer 3000HS.

SLN were diluted by a factor of 50 in ddH_2O and adjusted to an acidic pH using HCl. Measurement of hydrodynamic radius and zeta potential was conducted using a Beckman-Coulter 440SX Zetasizer.

Fluorescence and Electron Microscopy of Polymeric and Solid Lipid Nanoparticles

Fluorescence microscopy of DAPI (VECTASHIELD)-loaded PLGA NP mounted in PBS, pH=7.4, was conducted on a Zeiss Axiophot equipped with bandpass excitation and emission filters specific for the dye. Digital photographs were acquired at optically- and digitally-enhanced 400X magnification and analyzed using Zeiss-supplied software. SLN-QD, SLN-QD with FITC-PLL surface functionalization, and SLN bearing FITC-BSA-iron oxide NP were mounted in borate buffer, pH = 8, and analyzed using a Nikon TE-2000U fluorescence microscope equipped with bandpass excitation and emission settings of 380/45ex, 585/40em for SLN-QD, and a standard FITC configuration to visualize dye-conjugated PLL on the SLN surface or entrapped FITC-BSA, at digitally and optically-enhanced magnification of up to 500X. For microscopy of FITC-BSA/iron oxide bearing SLN, the solution was supplemented with 0.5% Trypan Blue to quench non-encapsulated FITC-BSA fluorescence. A 1.5T static magnet was placed on the right edge of the microscope slide to induce coordinated movement of FITC-BSA/iron oxide SLN in response to the applied field. Images were analyzed using Image Pro Plus 5.1 software (Media Cybernetics).

SLN-QD were prepared for electron microscopy by mounting on Formvar grids with 50:50 EtOH:phosphotungstic acid solution to visualize solid lipid in negative relief using a Philips CM-12 electron microscope. Electron density of encapsulated QD enabled facile visualization.

X-ray Photoelectron Spectroscopy (XPS) of Polymeric NP

Polymeric NP were prepared for XPS surface analysis by dialysis of a 5 mL NP suspension against 500 mL 50% EtOH, flash freezing of NP in liquid nitrogen, followed by lyophilization for 48 hrs. The NP powder surface composition was analyzed using a Kratos Axis-Ultra X-ray photoelectron spectrometer equipped with a monochromatic Al Kα (1486eV) x-ray source, configured at at 315W (25mA). Data was collected using a pass-energy of 40eV with 0.05eV steps. Elemental composition was determined using CasaXPS software.

Fluorescence Spectrophotometry of Solid Lipid NP

SLN-QD-PSS and SLN-QD-PSS-FITC/PLL were diluted 10-fold in borate buffer, pH=8. 2 uL of each suspension was then analyzed on a Nanodrop ND-3300 spectrofluorimeter configured for UV LED excitation and automatic sensitivity adjustment, with fluorescence emission intensity analyzed in the visible spectrum.

Results and Discussion

Control of Polymeric Nanoparticle Size and Polydispersity

We hypothesized that judicious selection of an appropriate organic solvent composition for dissolution of the non-functionalized polymer (i.e., PLGA or PLA), by alteration of solvent polarity, would have significant effect on NP size by modulating the rate of polymer chain collapse into a nanoparticle upon the rapid addition of water. By varying both the choice of solvent pairs and the relative solvent volumetric ratios, the process yielded polymeric NP diameters ranging from 70-400nm, with narrow PDI. Representative results are shown in **Table 1**. It is likely that the primary determinant of NP size in our system is solvent composition. Specifically, a highly-polar solvent system with dissolved PLGA or PLA, upon addition of water, collapses rapidly into small NP, whereas a less polar solvent system would support slower polymer chain collapse upon interaction with water, to yield larger NP.

Table 1. Typical NP diameter and polydispersity index (PDI) measured for different combinations of polymer, polyelectrolyte (aqueous), and binary solvent systems.

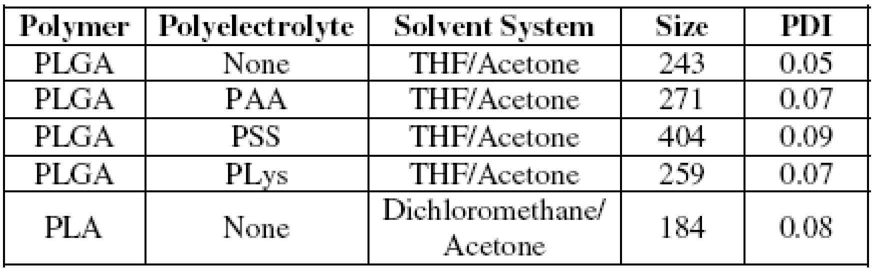

Polymer	**Polyelectrolyte**	**Solvent System**	**Size**	**PDI**
PLGA	None	THF/Acetone	243	0.05
PLGA	PAA	THF/Acetone	271	0.07
PLGA	PSS	THF/Acetone	404	0.09
PLGA	PLys	THF/Acetone	259	0.07
PLA	None	Dichloromethane/ Acetone	184	0.08

Surface Engineering of Polymeric Nanoparticles

The presence of a polyelectrolyte in the aqueous phase prior to organic-aqueous phase mixture provided a mechanism for spontaneous surface functionalization of the solidifying non-functionalized polymer core. We hypothesized that by utilizing polyelectrolytes for surface functionalization with high affinities for water, preferential accumulation of the surface moieties would occur at the NP-water interface following phase inversion. Zeta potential analysis of polymeric NP supports our hypothesis. **Figure 1** shows the surface charge variation as a function of pH for non-functionalized (PLGA) and functionalized (PLGA-PSS, PLGA-PLL) nanoparticles. As shown, the isoelectric point of the nanoparticulate formulation is associated closely with the pK_a of the ionizable group (PLGA = -COOH, PSS = SO_3H, PLL = NH_2).

XPS analysis also confirms our hypothesis, as polymeric NP surface compositions were abundant with the desired functionality (**Table 2**). It is important to note that PSS, despite its charge profile to PLGA, is effectively entrapped on the PLGA NP surface using our approach (66%). Additionally, the ability to functionalize NP surfaces with PLL enables the potential bioconjugation of ligands via amide linkages to the NP surface for *in vivo* targeting applications. Thus we are able to rapidly produce PLGA NP of defined size ranges and narrow PDI, with the added benefit of customizing NP surface information.

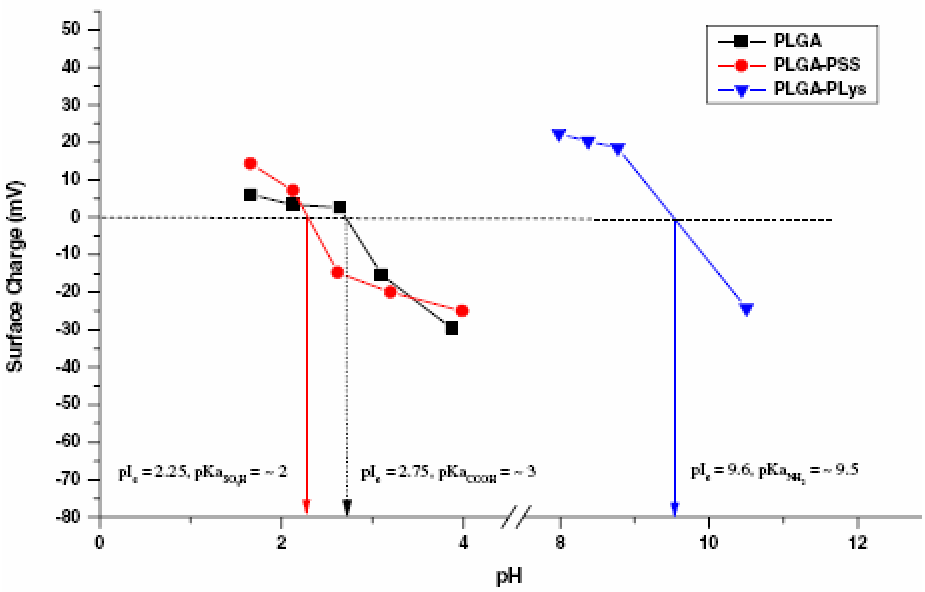

Figure 1. Zeta potential as a function of pH for non-functionalized and functionalized PLGA NP. Isoelectric points of NP correlate with the pKa of the PLGA or polyelectrolyte functional groups.

Table 2. Surface composition of PLGA NP as analyzed by XPS (C^1S).

	COOR	COO-C-OR	C-OR	C-H_x	Percentage of surface mass for functional moiety
PLGA	38.2	36.7	nd	25.1	
Std. Dev.	0.0	0.0	--	0.0	
PLGA-PLys	27.1	28.0	9.0	36.0	24%
Std Dev	3.1	3.2	1.6	4.7	9%
PLGA-PSS	12.1	12.5	nd	75.5	66%
Std Dev	1.6	1.6	--	3.2	4%

Encapsulation of Small Molecules by Polymeric NP

Our single-step process for the surface engineering of polymeric NP does not appear to preclude the encapsulation of compounds for drug delivery or imaging purposes. Fluorescence microscopy of DAPI-loaded PLGA-PSS NP reveals that the water-soluble dye is efficiently and homogenously entrapped within the NP core (**Figure 2**). In other work, we have entrapped other fluorescent dyes, proteins, and synthetic drugs within polymeric NP. Thus, our process appears to be a versatile approach for packaging structurally and functionally-diverse cargoes within well-defined (tight size range and PDI) and surface functionalized NP.

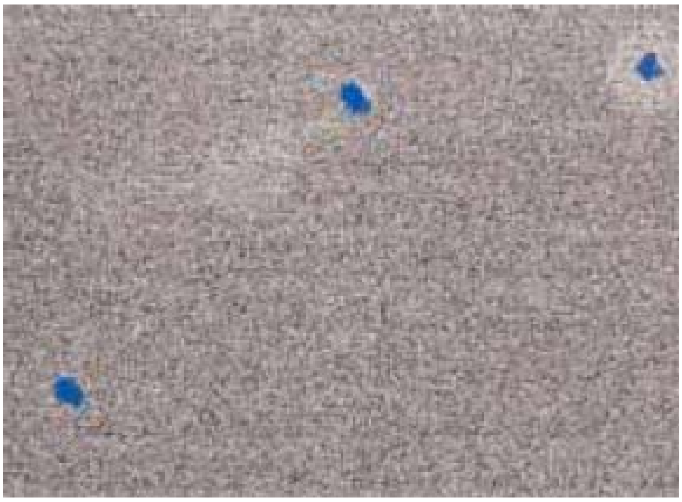

Figure 2. Fluorescence micrograph (400X) of DAPI-loaded PLGA NP.

Control of Solid Lipid Nanoparticle Size and Loading Efficiency

An adaptation of our procedure for synthesizing functionalized polymeric NP for the entrapment and targeted delivery of small therapeutic and diagnostic agents enabled us to develop a similar process for the rapid single-step production of functionalized SLN. After considerable investigation we found the binary solvent system NMP:Acetone to provide effective size control of SLN while also providing for excellent solubility of the coco-glyceride. High ratios of NMP:Acetone are associated with rapid lipid packing upon exposure to water, due to the high miscibility of NMP with water. Lower ratios result in slower lipid packing, resulting in larger SLN. Quantum dots, which without commercial modifications are highly hydrophobic, were selected as a candidate for encapsulation, as it has a high molecular weight and has emerged as a fluorescent probe with superior optical properties for bioimaging applications (*7*). By varying the volumetric ratio of NMP:Acetone from 40:60 to 80:20, SLN bearing quantum dots ranging from 75nm-790nm were synthesized. Furthermore, by varying the SLN diameter through solvent composition, we were able to concurrently modulate SLN loading efficiency of QD (**Figure 3**). Larger SLN diameters, or larger lipid matrix cores, allow for more incorporation of QD as they partition into the lipid phase upon exposure to water. The high loading capacity of 100nm SLN, for example (100-150 QD avg. per SLN (n=10) as determined by TEM), allows for the creation of nanoparticulate probes with significantly enhanced signal intensity compared to single nanoparticles (**Figure 3**). This feature could be useful in many biomedical applications, including the magnetic resonance (e.g., CLIO-NP) or fluorescence-based (e.g., QD) signal amplification of low levels of antigens on cell surfaces, or the delivery of large payloads of drug into cells.

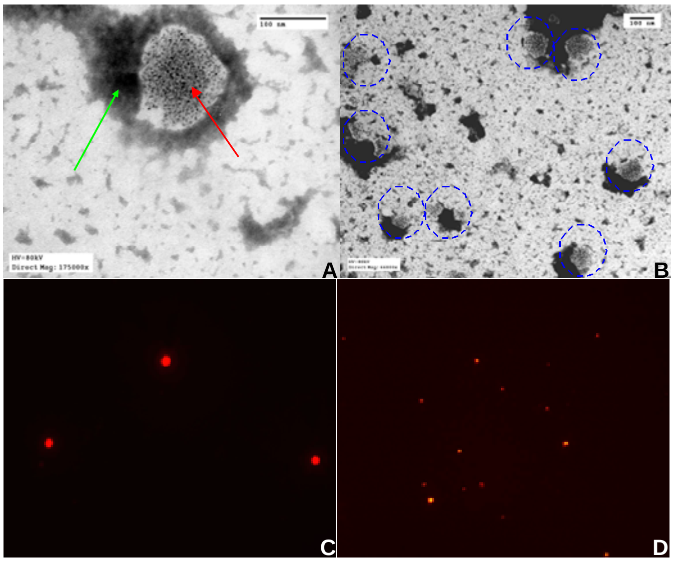

Figure 3. Transmission electron microscopy and fluorescence microscopy of SLN-QD. First row: A.) Transmission electron micrograph (175000X at 80keV, scale bar 100nm) showing 2.4nm 580nm-emitting CdSe/ZnS quantum dots (red arrow) within a lipid matrix (white background of QD) against phosphotungstic acid negative lipid stain (green arrow). B.) TEM (66000X at 80 keV) of same SLN-QD sample, showing dispersion and narrow size range of SLN-QD (outlined in blue). Second row: Fluorescence micrographs (40X) of large-diameter (C) and small-diameter (D) SLN-QD.

Surface Engineering of SLN

By incorporation of polyelectrolytes into the aqueous phase prior to the lipid-packing phase inversion step, we efficiently loaded the desired surface functionality upon the SLN surface in a manner analogous to that seen for polymeric NP. Functionalization of negative charges upon SLN (SLN-PSS) was confirmed by zeta potential analysis (**Figure 4**). As shown in **Figure 5**, fluorescence microscopy and spectrophotometry were indicative of efficient surface incorporation of dye-labeled PLL. PLL was readily functionalized upon SLN surfaces by layer-by-layer assembly. By first synthesizing SLN initially coated with the negatively-charged PSS, which effectively incorporates within the lipid while remaining preferentially at the NP-water interface (due to the sulfonic acid group), the positively-charged PLL can be layered electrostatically. Other surface functionalities presented on SLN surfaces to date include polyethylene glycol (PEG) for evasion of the mononuclear phagocyte system *in vivo (8)*, polyacrylic acid (PAA), which has been utilized to incorporate mucoadhesive properties (*9*), and streptavidin for biotin-based immunofluorescence applications (*10*). Thus, our process enables the encapsulation of functionally-diverse nanoparticles (i.e. dye, contrast agent, therapeutic) within solid lipid matrices capable of bearing different types of surface information.

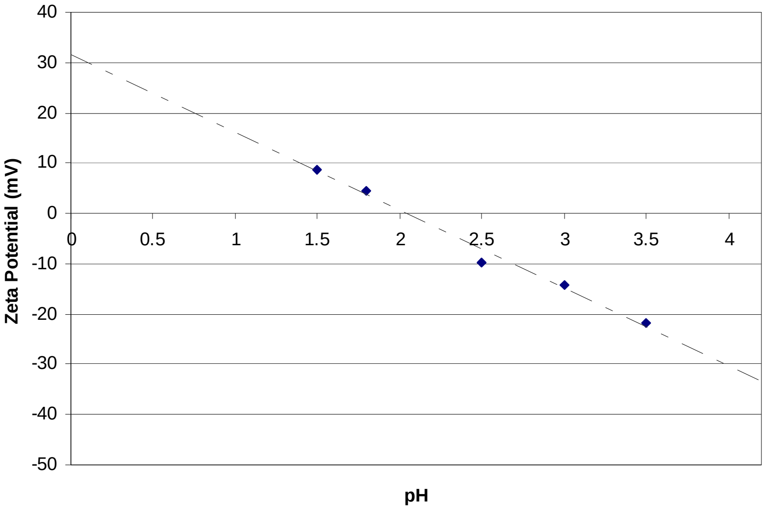

Figure 4. Zeta potential analysis of SLN-QD-PSS as a function of pH. The isoelectric point of the sample correlates with the pKa of the sulfonic acid group of PSS, thus indicating effective surface functionalization.

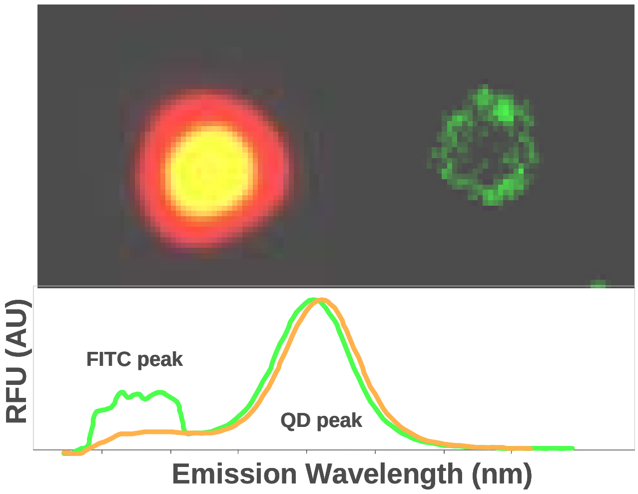

Figure 5. Top Row: Fluorescence microscopy of QD entrapped within PSS-FITC/PLL-functionalized SLN, in the QD 580 emission (left) and FITC emission channels (right). The core of the SLN exhibits high QD fluorescence due to effective entrapment of hydrophobic QD within the lipid matrix, whereas FITC-PLL is adsorbed upon previously incorporated PSS at the NP-water interface, thus providing an amine template for further bioconjugation. Bottom Row: Fluorescence spectrophotometry of QD-PSS (orange) and QD-PSS-FITC/PLL (green) SLN. Surface functionalization of PLL (initial FITC peak as indicated) does not significantly affect native QD fluorescence (580nm emission peak, as indicated). Mean diameter 550 nm.

Multimodal SLN for Biomedical Applications

In order to demonstrate the potential of SLN as multimodal carriers, we co-encapsulated 50nm silica-capped paramagnetic iron oxide NP and FITC-BSA within PSS-functionalized lipid matrices by incorporation of both species within the aqueous phase prior to phase inversion. FITC-BSA/iron oxide NP SLN coated with PSS were incubated in a solution containing 0.5% trypan blue and analyzed by fluorescence microscopy (**Figure 6**). Trypan Blue is an effective quenching agent for reducing extracellular FITC as part of phagocytosis assays (*11*). We therefore utilized trypan blue to quench unencapsulated FITC-BSA to confirm that only FITC-BSA within SLN was visualized. Upon application of a magnetic field using a static magnet (1.5 T), FITC-BSA nanoparticles shown in **Figure 6** were observed to move in response to magnet polar orientation. Fluorescent nanoparticles were highly sensitive to rapid changes in the external field while control nanoparticles consisting of FITC-BSA mixed with iron oxide NP in distilled water without lipid did not move in response to changes in magnetic fields. These data suggest that FITC-BSA was co-encapsulated with iron oxide NP, and that the native magnetization properties of the NP are not affected by encapsulation. We have in effect created a technique applicable to the development of magnetooptical probes which employ fluorophores (e.g. quantum dots or fluorescently-labeled proteins) and iron oxide nanoparticles, which would have applications for in vivo imaging using MRI and fluorescence imaging techniques such as multiphoton excitation microscopy. Further work is directed toward the co-encapsulation of QD and iron oxide NP to develop high-intensity magnetooptical probes for bioimaging applications, as well as drug-QD conjugates for pharmacokinetic/pharmacodynamic studies of chemotherapeutics.

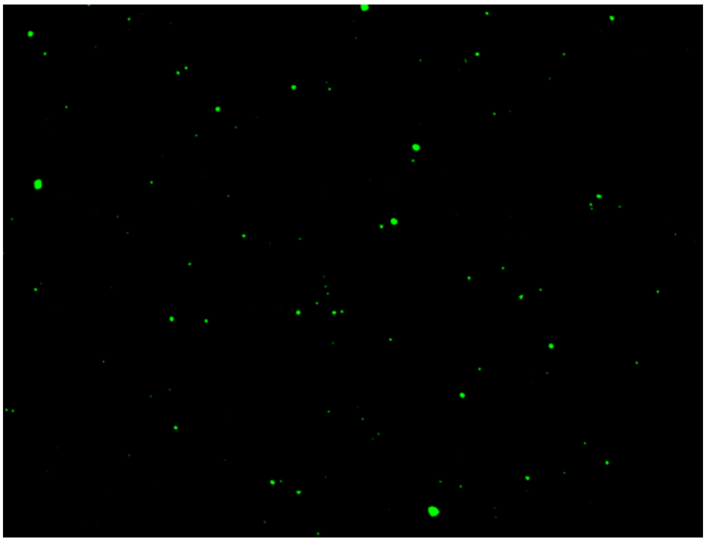

Figure 6. Fluorescence microscopy of SLN bearing FITC-BSA and iron oxide NP in a solution of 0.5% Trypan Blue. Encapsulated FITC-BSA not accessible to Trypan Blue in mounting medium is evident, and all SLN were observed to move toward the pole of an externally applied magnet, indicating successful co-encapsulation of FITC-BSA with iron oxide NP.

applications, as well as drug-QD conjugates for pharmacokinetic/pharmacodynamic studies of chemotherapeutics.

Conclusion

We have demonstrated a technique for the rapid synthesis of functionalized polymeric NP, and an analogous procedure for producing functionalized solid lipid nanoparticles. Our process provides for the simultaneous, efficient entrapment of compounds of varying physicochemical properties, so that combinative imaging and therapeutic strategies can be harnessed. Mechanical dispersion, the addition of emulsifying agents, or temperature-dependent steps are not required. The lipid utilized in SLN is derived from cosmetic formulations, and all solvents used in synthesis are removed, thus ensuring biocompatibility. Furthermore, the process can be easily scaled-up for the mass production of pharmaceuticals and SLN are highly-stable in storage. Future work is directed toward with the applications of multimodal SLN for the simultaneous utilization of multiple imaging modalities as well as combined drug delivery/gene therapy approaches.

Acknowledgements

This work was supported in part by the Vanderbilt University Discovery Grant Program (VPS), and a Vanderbilt Vision Research Center Training Grant (AJ).

References

(1) Sussman, E. M., Clarke, M. B., Jr., and Shastri, V. P. (2007) Single-step process to produce surface-functionalized polymeric nanoparticles. *Langmuir 23*, 12275-9.

(2) Muller, R. H., and Keck, C. M. (2004) Challenges and solutions for the delivery of biotech drugs--a review of drug nanocrystal technology and lipid nanoparticles. *J Biotechnol 113*, 151-70.

(3) Uner, M., Wissing, S. A., Yener, G., and Muller, R. H. (2004) Influence of surfactants on the physical stability of solid lipid nanoparticle (SLN) formulations. *Pharmazie 59*, 331-2.

(4) Wissing, S. A., Kayser, O., and Muller, R. H. (2004) Solid lipid nanoparticles for parenteral drug delivery. *Adv Drug Deliv Rev 56*, 1257-72.

(5) Estey, T., Kang, J., Schwendeman, S. P., and Carpenter, J. F. (2006) BSA degradation under acidic conditions: a model for protein instability during release from PLGA delivery systems. *J Pharm Sci 95*, 1626-39.

(6) Mohammed, A. R., Weston, N., Coombes, A. G., Fitzgerald, M., and Perrie, Y. (2004) Liposome formulation of poorly water soluble drugs: optimisation of drug loading and ESEM analysis of stability. *Int J Pharm 285*, 23-34.

(7) Stroh, M., Zimmer, J. P., Duda, D. G., Levchenko, T. S., Cohen, K. S., Brown, E. B., Scadden, D. T., Torchilin, V. P., Bawendi, M. G., Fukumura, D., and Jain, R. K. (2005) Quantum dots spectrally distinguish multiple species within the tumor milieu in vivo. *Nat Med 11*, 678-82.

(8) Woodle, M. C., and Lasic, D. D. (1992) Sterically stabilized liposomes. *Biochim Biophys Acta 1113*, 171-99.

(9) Guggi, D., Marschutz, M. K., and Bernkop-Schnurch, A. (2004) Matrix tablets based on thiolated poly(acrylic acid): pH-dependent variation in disintegration and mucoadhesion. *Int J Pharm 274*, 97-105.

(10) Diamandis, E. P., and Christopoulos, T. K. (1991) The biotin-(strept)avidin system: principles and applications in biotechnology. *Clin Chem 37*, 625-36.

(11) Finnemann, S. C., Bonilha, V. L., Marmorstein, A. D., and Rodriguez-Boulan, E. (1997) Phagocytosis of rod outer segments by retinal pigment epithelial cells requires alpha(v)beta5 integrin for binding but not for internalization. *Proc Natl Acad Sci U S A 94*, 12932-7.

APPENDIX D

LIGHT-GUIDED SURFACE ENGINEERING FOR BIOMEDICAL APPLICATIONS

Ashwath Jayagopal
Gregory P. Stone
Frederick R. Haselton

Department of Biomedical Engineering
Vanderbilt University
Nashville, Tennessee

Bioconjugate Chemistry 19, 792-6. 2008

Abstract

Free radical species generated through fluorescence photobleaching have been reported to effectively couple a water-soluble species to surfaces containing electron-rich sites (*1*). In this report, we expand upon this strategy to control the patterned attachment of antibodies and peptides to surfaces for biosensing and tissue engineering applications. In the first application, we compare hydrophobic attachment and photobleaching methods to immobilize FITC-labeled anti-M13K07 bacteriophage antibody to the SiO_2 layer of a differential capacitive biosensor and to the polyester filament of a feedback-controlled filament array. On both surfaces, antibody attachment and function were superior to previously employed hydrophobic attachment. Furthermore, a laser scanning confocal microscope could be used for automated, software-guided photoattachment chemistry. In a second application, the cell adhesion peptide RGDS was site-specifically photocoupled to glass coated with fluorescein-conjugated polyethylene glycol. RGDS attachment and bioactivity were characterized by a fibroblast adhesion assay. Cell adhesion was limited to sites of RGDS photocoupling. These examples illustrate that fluorophore-based photopatterning can be achieved by both solution-phase fluorophores or surface adhered fluorophores. The coupling preserves the bioactivity of the patterned species, is amenable to a variety of surfaces, and is readily accessible to laboratories with fluorescence imaging equipment. The flexibility offered by visible light patterning will likely have many useful applications in bioscreening and tissue engineering where the controlled placement of biomolecules and cells is critical, and should be considered as an alternative to chemical coupling methods.

Introduction

Strategies for the directed patterning of biomolecules at specific sites on diverse material surfaces are highly desired for multiplexed, array-based screening paradigms (*2*) as well as technologies such as tissue engineering, which rely on micro- or nanoscale cell-protein interactions (*3*). Recently, a fluorophore-based immobilization technique was described for the high-resolution, site-specific patterning of proteins such as enzymes within microfluidic channels (*1, 4*). This method utilizes photobleaching, a singlet oxygen-dependent immobilization mechanism, to couple dye-labeled proteins to glass and polydimethylsiloxane (PDMS) surfaces. Visible light patterning has two main advantages over other biomolecular patterning strategies. Non-damaging wavelengths, such as those used in aryl azide and benzophenone chemistries (*5, 6*), are avoided. Secondly, the reaction can be rapidly carried out in aqueous, neutral buffers preserving protein functionality.

In order to facilitate the implementation of photoattachment chemistry in the development biomolecular and/or cellular arrays, further studies are necessary to expand upon the scope of materials which can be surface engineered using this process, namely polymer surfaces. Also, efforts to facilitate photopatterning, such as implementation with laser scanning confocal microscopes and software-driven, automated bleach parameters, are relatively unexplored. In addition, a reverse-coupling technique would be desirable. In this case, instead of labeling the soluble protein with a dye, the target surface is conjugated to a fluorophore. This has several advantages. Dye-labeling of proteins is not required, and in this scenario, one photoactivable surface could be employed for the patterning of multiple biomolecules.

In this study, we explored the utility of visible light-guided surface engineering for site-specific antibody immobilization on a differential capacitance-based viral biosensor (*7*) as well as a polyester filament-based fluorescence detection platform (*8-10*). We then extended this photopatterning technique to couple the cell adhesion peptide RGDS (*11*) to a surface layer of polyethylene glycol-fluorescein (PEG-FITC) with the intent of developing a substrate for site-specific biomolecular and cellular patterning. This latter example also features low nonspecific adsorption, a limitation not addressed in previous visible-light photopatterning techniques (*4*). In these initial studies, we observed that a variety of surfaces are amenable to photopatterning, and that the simplicity of these techniques makes automated surface patterning readily accessible to biological laboratories with access to a laser scanning confocal microscope. This method may have broad applicability in the field of biosensors which rely on an *a priori* pattern of binding partners as well as tissue engineering applications which rely on spatial control of cells in their construction. Photocoupling can also be used to functionalize nanoparticles and other bioconjugates bearing amine or PEG-FITC moieties.

Experimental Procedures

Antibodies were photocoupled onto silicon dioxide and polyester surfaces for sandwich immunoassays. In the third portion of this report, peptides were photoimmobilized on PEG-FITC coated capture substrates in order to modulate cell attachment.

Photopatterning of capture antibody on capacitive M13K07 sensor

A previously-characterized, capacitive sensor for the detection of M13K07 bacteriophage (*7*) was prepared for use under dry argon at 25ºC with three rinses of anhydrous acetone (Sigma, St. Louis, MO). The surface was then immersed in a 4% solution of 3-aminopropyltriethoxysilane (United Chemical Technologies, Bristol, PA) in anhydrous acetone for 10 minutes, followed by 5 minute immersions in anhydrous acetone and ultrapure water, and stored at 25ºC in a desiccator. Successful silanation of capacitor surfaces was verified by comparing the adsorption of fluorescein-conjugated bovine serum albumin (1 mg/mL in borate pH = 8.5) on treated and untreated chips. Immediately prior to use, the silicon dioxide surface was layered by micropipette with 100 μL of a 100 μg/mL FITC-anti-M13K07 monoclonal antibody ((mAb), 2.8 mol FITC/mol IgG) in 100 mM sodium bicarbonate buffer, pH = 8.5.

The FITC-labeled capture mAb (anti-M13K07 Ms $\mathrm{IgG_1}$, GE Healthcare) was immobilized onto the biosensor surface using an upright laser scanning confocal microscope (LSM 510, Carl Zeiss). The timed bleach function provided in the microscope manufacturer's software package, as used for fluorescence recovery after photobleaching (FRAP) studies (*12*), was used to control the laser intensity of the 488 nm line of a 30 mW Argon laser, as well as the number of scanning iterations. A 4X, 0.1 NA objective was used to scan the 200 μm^2 capacitor surface. Two capacitors were each bleached using different bleach iterations (50 vs. 10, using 100% laser intensity). Using the manufacturer's software, the laser was rastered in parallel with the plates of the capacitor, and the bleaching time was less than three minutes. The surface was rinsed three times with PBS, pH = 7.4 for 1 minute each. Next, the capacitors were coated with the same amount and concentration of FITC-mouse IgG_1 isotype control mAb (3 mol FITC/mol IgG), and bleached at 100% intensity for 50 iterations.

The functionality of the photoimmobilized surface was ascertained by sandwich immunoassay. The surface was rinsed with PBS, and exposed to a solution of 100 μL of M13K07 bacteriophage ($3.3 \text{ X } 10^{11}$ virions/mL) for 30 min at 25ºC. The surface was rinsed with PBS and incubated with 100 μL of Cy5-conjugated anti-M13K07 mAb (1.72 mol Cy5/mol IgG, 50 μg/mL in PBS) for 30 min at 25ºC. The chip was rinsed with PBS and imaged immediately on a Nikon TE2000U inverted fluorescence microscope equipped with a Cy5 fluorescence cube, an Exfo X-Cite 120 metal halide excitation light source, and a C7780 Hamamatsu cooled CCD camera. Mean fluorescence intensities were measured by analyzing ROIs defined along capacitor boundaries using Image Pro Plus 5.0 (Media Cybernetics), with data plotted using SigmaPlot 9.0 (SYSTAT).

Photopatterning of antibody on polyester filament-based M13K07 sensing array

We investigated the utility of photoattachment chemistry in the development of high-throughput biomolecular screening. A previously described polyester monofilament-based system for viral detection based on hydrophobically-immobilized capture mAb for multiplexed sandwich immunoassays (*9*) was adapted for the detection of M13K07 bacteriophage, a test virus, based on *photopatterned* capture mAb. All procedures were carried out at 25°C. A 120 μm polyester monofilament (Sulky Corp.)

was wrapped around a PhastGel sample applicator (GE Healthcare) and inlaid within the concave teeth as previously described (*9*). The filament/comb apparatus was rinsed in successive washes of 70% ethanol, 10% HCl, Milli-Q water, and dried overnight prior to use. 0.75 µL of solution containing 100 µg/mL of anti-M13K07 mAb or mouse IgG_1 isotype control mAb in 100 mM borate buffer, pH = 8.5 was pipetted on each loading tooth for either timed passive incubations or photobleaching sessions. The distance between neighboring teeth is 0.5 cm. For photobleaching, the comb was inverted and suspended within a humidified 60 mm petri dish upon the Nikon TE2000U microscope stage. For photobleaching, the X-Cite 120 metal halide light source was used in conjunction with a FITC cube and 4X objective at full lamp intensity (1.4 W from microscope emission port, as determined by the manufacturer) for specific durations. Bleaching was monitored by measuring filament mean fluorescence using Image Pro Plus 5.0.

To test the functionality of the passively-adsorbed and photopatterned surfaces, combs were was rinsed three times in PBS, immersed in a multichannel pipette basin containing 3.3 X 10^{11} virions/mL M13K07 in PBS for 30 min, and rinsed three times with PBS. The combs were subsequently immersed in a basin containing 50 µg/mL Cy5-anti-M13K07 mAb for 30 min and rinsed in PBS.

Filaments were immediately fastened to a standard, pre-cleaned microscope slide with tape, and the fluorescence measured using a Genepix 4000B microarray scanner (Axon Instruments) equipped with a 635 nm laser line as previously-described (*9*). Mean fluorescence intensity of ROIs defined along discrete filament spots was measured by Image Pro Plus on grayscale 16-bit images, and plotted using SigmaPlot.

*Photopatterning of poly-*D*-lysine coated glass substrate with PEG-RGDS*

Poly-D-lysine-coated 35 mm glass-bottom dishes with no. 1 borosilicate coverglass (MatTek Corp.) were coated with a heterobifunctional PEG spacer (MW = 3400) containing an N-hydroxysuccinimide ester (NHS) amine-reactive group and a fluorescein isothiocyanate moiety (NHS-PEG-FITC, Nektar Therapeutics) by incubating the surface with 0.2 mg of NHS-PEG-FITC in 100 mM borate buffer, pH = 8.5 for 1 hr. followed by three rinses in borate buffer. Unreacted amine groups were quenched by 20 min. incubation with 1 mg of sulfo-NHS-acetate (Pierce Chemical) in borate buffer. This acetylation reaction rendered the remaining amines unreactive. The glass dish was then incubated with with 100 μg/mL of the fibronectin-derived cell adhesion peptide RGDS (> 95% purity, Genscript Corp.) in borate buffer. Photobleaching of 1 mm rectangular areas delineated by taped foil photomasks was achieved using a 10X objective with the aforementioned inverted fluorescence microscope and light source for timed intervals, with mean fluorescence levels monitored to confirm photobleaching. Typically, the time necessary to reduce intensity levels 20% of initial fluorescence was less than 5 minutes. Photobleaching and RGDS passive adsorptions were followed by three rinses in borate. RGDS presence on the glass substrate was qualitatively assessed using fluorescamine.

Since RGDS has been demonstrated to promote fibroblast adhesion and spreading (DeLong et al. 2005), we evaluated the bioactivity of the coupled RGDS using a fibroblast adhesion assay. 3T3 fibroblasts (ATCC) were cultured to 70% confluency in DMEM containing 10% bovine calf serum under incubation at 37°C, 5% CO2. The cells were then seeded in each dish at a concentration of 1000 cells/mL and incubated overnight under the same culture conditions. The next day, dishes were rinsed three times with PBS, and fixed for 20 min. at 25°C in 4% paraformaldehyde in PBS. Dishes were incubated with 0.5% trypan blue prior to the fixation step to ascertain cell viability via dye exclusion. The dishes were then rinsed in PBS containing 100 mM glycine and imaged by phase-contrast.

Comparison of antibody chemical crosslinking and photoattachment on PEG-FITC and PEG-maleimide-coated glass substrates

Poly-D-lysine-coated MatTek dishes were coated with 0.2 mg of NHS-PEG-FITC or thiol-reactive NHS-PEG-Maleimide (NHS-PEG-MAL, MW = 3400, Nektar) and acetylated as described in *2.3*. To generate sulfhydryl groups for covalent coupling of mAb to NHS-PEG-MAL, 5 mg of anti-M13K07 mAb in 1 mL PBS-EDTA, pH = 7.4 was reacted with a 10-fold molar excess of 2-iminothiolane (Traut’s reagent, Sigma) for 30 min. at 25°C. Excess Traut’s reagent was removed by 3 centrifugation cycles of mAb/Traut’s reagent on an Amicon-4 Ultra 100K MWCO spin column filtration device (Millipore) using PBS-EDTA as the rinse and resuspension buffer. For chemical crosslinking, 200 μg of mAb in 200 μL PBS-EDTA was pipetted onto the PEG-MAL surface and was reacted overnight at 4°C. For photocrosslinking, 200 μg of purified mAb in a 200 μL solution of PBS-EDTA was pipetted on the PEG-FITC surface. The microwell of the dish was then photobleached using the X-Cite 120 light source (1.4 W) using a 2X objective for 10 min. Following both reactions, the dishes were rinsed 3X with PBS, saving the initial aspirate. Aspirate was collected from 20 MatTek dishes bearing either the PEG-FITC or PEG-MAL attachment linker. Protein concentration was determined using the Coomassie Plus assay (Pierce) according to manufacturer instructions.

Results and Discussion

Our studies suggest that photobleaching can be used to pattern proteins and peptides on SiO_2, polyester, and glass surfaces. Photopatterning of anti-M13K07 mAb to capacitor surfaces was site-specific, with an achieved spatial resolution below 10 μm (**Figure 1a-b**). No signal was detected due to photopatterned IgG_1 control mAb capture of virus, or nonspecific binding of the virus itself, as indicated by mean fluorescence output (**Figure 1c**). In addition, no secondary antibody fluorescence was detected beyond the capacitor regions of the chip, indicating that diffusion of the bleached fluorophore did not interfere significantly with site-specific coupling, and that nonspecific adsorption was not significant. Specifically, the average fluorescence from 10 different non-capacitor regions of the chip was 237 ± 67, which was similar to control capacitor values (**Figure 1c**).

The fluorescence signal from sandwich immunoassay generated from filament-coupled anti-M13K07 mAb using photoattachment chemistry was two to three-fold higher than signal generated by passively-adsorbed antibodies (**Figure 2**). The enhanced signal could be due to either a.) an initially-higher coupling efficiency using the photobleaching technique, and/or b.) greater preservation of bioactivity of photocoupled mAb. Although further studies would be required to differentiate between these two possibilities, we did observe that photocoupled antibodies appeared to be more tightly-coupled since successive washes of filament was associated with loss of passively-adsorbed antibodies but with low loss of photocoupled antibody (data not shown).

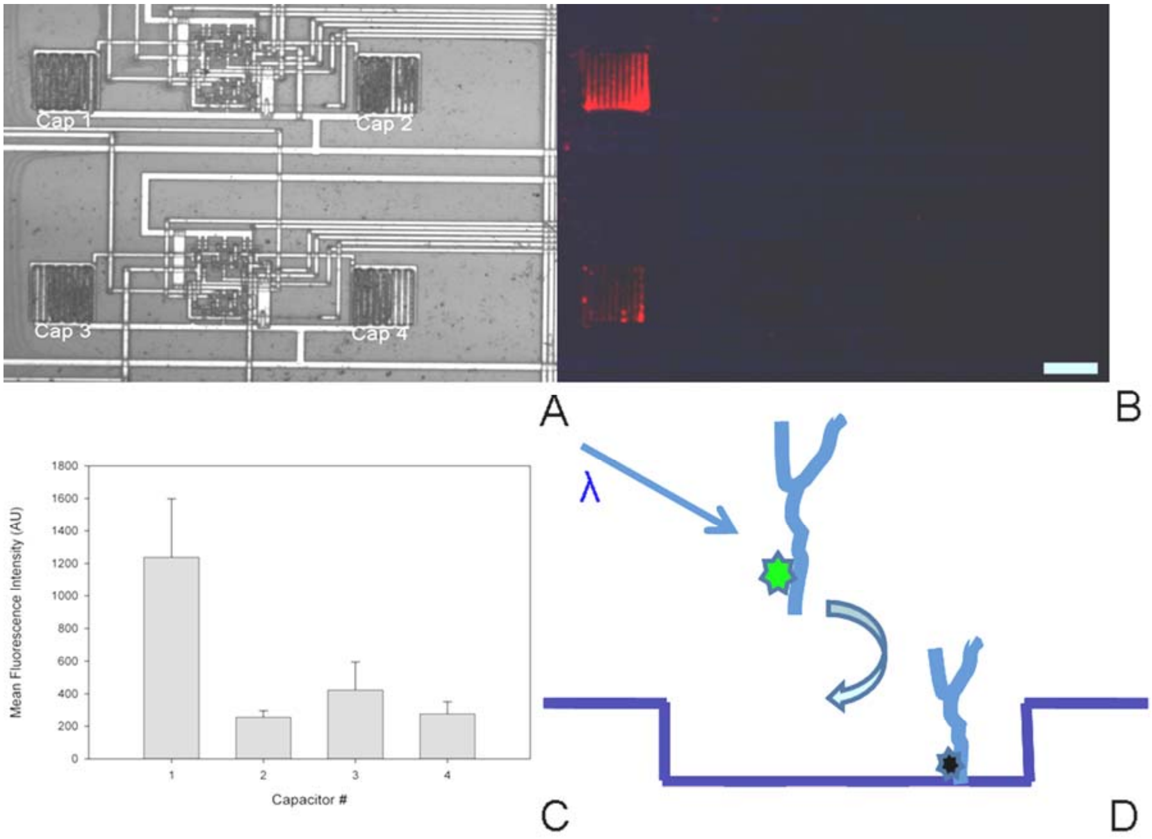

Figure 1. Light (A) and fluorescence (B) micrographs of a multiplexed capacitive biosensor photopatterned with anti-M13K07 monoclonal antibodies and isotype controls, with measured fluorescence intensities shown in (C). Parameters and reagents used for photoattachment using a confocal microscope: Cap 1: 30 mW, 50 bleach iterations, anti-M13K07 photopatterned, Cap 2: 30 mW, 50 bleach iterations, anti-Ms IgG photopatterned, Cap 3: 30 mW, 10 bleach iterations, anti-M13K07 photopatterned, Cap 4: No patterned antibody. (C) Fluorescence intensity measurements of Cy5-anti-M13K07-incubated sensors, reported as mean ± S.D., n = 3. Bar = 10 μm

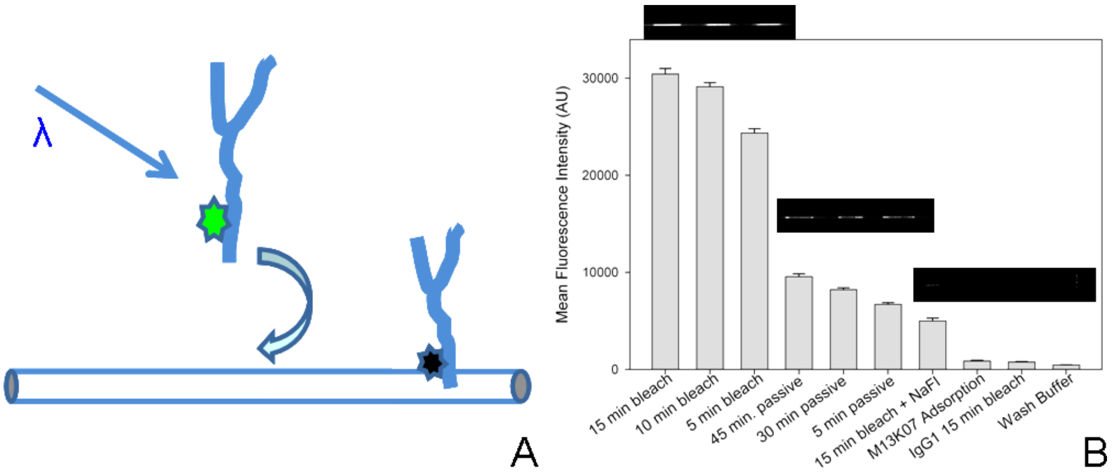

Figure 2. Schematic of a strategy for photocoupling of antibody to polyester filament (A) and resulting sandwich immunoassay Cy5-anti-M13K07 intensities (B). A representative filament is overlaid on the graph in (B).

Our studies also demonstrated that cell adhesion peptides can be site-specifically coupled on tissue culture substratum (**Figure 3**). Irradiated PEG-FITC regions (**Figure 3a**) promoted fibroblast attachment similar in density and morphology observed on the native poly-D-lysine-coated MatTek surface (**Figure 3e**). Non-irradiated PEG-FITC regions on the same were resistant to cell adhesion (**Figure 3b**). The lack of cell adhesion in nonirradiated regions was most likely due to the PEG-coating on the surface which blocks adsorption of RGDS (**Figure 3c**) as well as the fibroblasts themselves (**Figure 3f**). The PEGylation of the surface was found to be important for controlling cell attachment, as acetylation of the surface alone was not sufficient (**Figure 3d**). Complete photobleaching of the entire PEG-FITC surface (from 1 to 3 hours of continuous lamp illumination) did not result in cell attachment (**Figure 3g-h**). In a separate experiment, we demonstrated that attachment of 3T3 cells to PEG-RGDS was most likely due to specific peptide-integrin interactions, since competitive inhibition experiments (addition of 2 mM soluble RGDS peptide) reduced cell attachment by 82% (**Figure 4**).

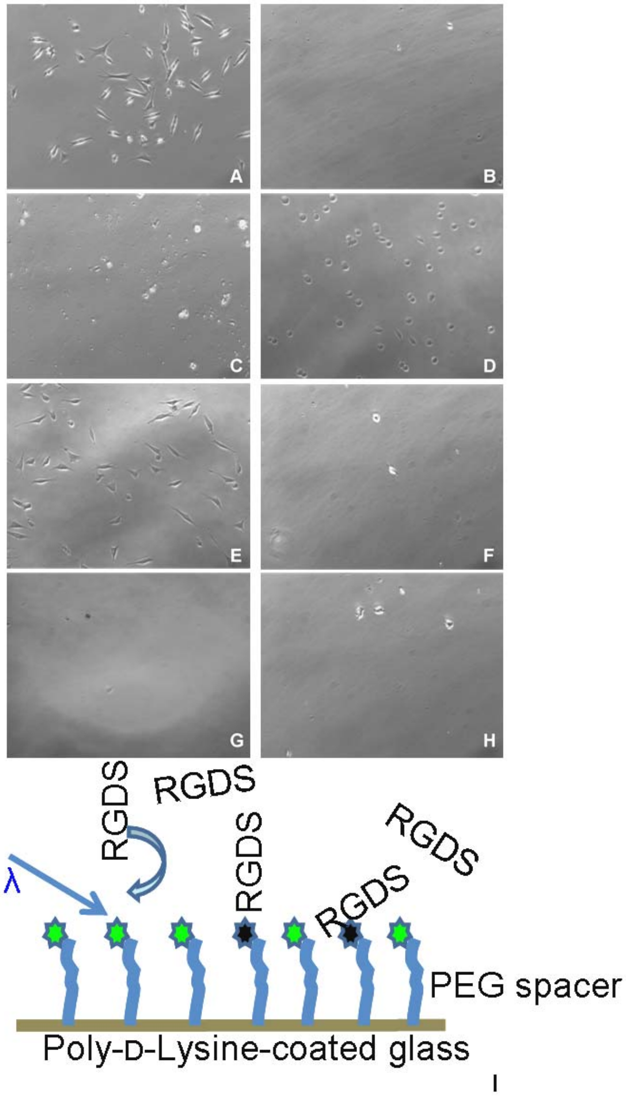

Figure 3. Representative micrographs of 3T3 fibroblast attachment on surface engineered poly-d-lysine MatTek dishes from 3 trials using PEG-FITC based photoattachment diagrammed in (I). Experimental conditions for each substrate: (A) PEG-FITC and acetylation, RGDS photopatterned; (B) Same as in (A), but in an area where RGDS was not photopatterned; (C) PEG-FITC and acetylation, RGDS passively adsorbed; (D) No PEG-FITC, acetylation, RGDS passively adsorbed (cells are rounded); (E) No PEG-FITC, no RGDS (native surface); (F) PEG-FITC, no acetylation, no RGDS; (G) PEG-FITC and acetylation, bleached 1 hr prior to cell adsorption, no RGDS; (H) PEG-FITC and acetylation, bleached 3 hrs. prior to cell adsorption, no RGDS. Cells in (A) and (E) showed similar viability of seeded cells as indicated by trypan blue exclusion (not shown). (50X magnification)

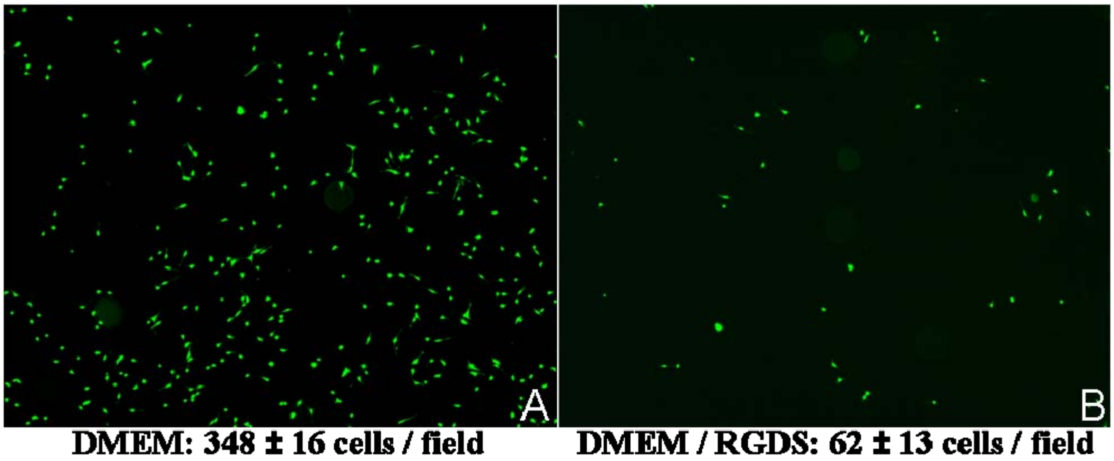

Figure 4. Competitive inhibition of 3T3 attachment to PEG-RGDS-coated MatTek glass bottom dishes. 3T3 cells at a concentration of 1000 cells/mL were incubated with 1 μM calcein-AM (Invitrogen) in serum-free DMEM for 20 min. at 37°C and seeded on PEG-RGDS-coated surfaces in the presence or absence of 2 mM soluble RGDS. Cells were incubated for 4 hrs. at 37°C, 5% CO_2, rinsed 3X with Hank's Balanced Salt Solution, and immediately imaged *via* fluorescence microscopy under FITC imaging settings to analyze attached cells. Viable cells as ascertained by calcein-AM fluorescence were counted in 10X fields (n = 4) using Image Pro Plus 5.1.Representative 10X fields show a.) 3T3 attachment onto PEG-RGDS-coated borosilicate glass, and b.) 3T3 attachment in the presence of 2 mM soluble RGDS. Shown on each panel is the mean ± S.D. of calcein-AM positive 3T3 cells counted within each 10X field, for each experimental condition.

The mAb coupling efficiency of photoattachment and chemical crosslinking was compared and found to be similar. The efficiency of photocoupling was measured to be 3.3 pmol / cm^2. Thiol-maleimide crosslinking, a technique which has long been utilized for efficient, facile conjugation of proteins to material surfaces (*13*), resulted in a higher mAb coupling efficiency (4.2 pmol / cm^2). Although the chemical crosslinking technique was capable of immobilizing a higher quantity of mAb, further optimization of experimental conditions may produce higher yields for visible light photoconjugation, such as buffer strength, reaction volume, PEG molecular weight, and reagent concentrations. Furthermore, photopatterning offers control over site specificity of coupling, which in itself may warrant its future implementation.

The light patterning properties of the confocal microscope facilitated the efficient photoattachment of antibodies on the biosensor surface. With a fixed laser intensity (full output), the number of bleach iterations within the FRAP software module controlled the coupling efficiency of FITC-mAb. Furthermore, the ROI can be readily defined within the software to pattern microscale regions. The patterning of antibodies upon groups of four capacitors was achieved within five minutes, and real-time fluorescence intensity measurements within the software confirmed successful photobleaching. The confocal microscope should facilitate the implementation of photoattachment methods in various laboratories in biological and biomedical sciences, where they are readily available. Since these laboratories often do not have access to cleanroom facilities needed for photolithography, photoattachment chemistry may constitute a viable alternative to the in-house development of custom molecular and cellular arrays as diagnostic or biological study tools.

In addition to extending techniques related to the coupling of dye-conjugated biomolecules on surfaces, we also hypothesized that biomaterial substrates could be engineered to bear the photoreactive groups, thus obviating the need for bioconjugating proteins, a step which can often compromise native function. Polyethylene glycol (PEG) has long been utilized for reducing protein adsorption to biomaterial surfaces, is biocompatible, and is amenable to the grafting of functional groups (*14*). NHS-PEG-FITC is a commercially-available heterobifunctional reagent used to detect PEGylation efficiency in bioconjugate chemistry, and combines the properties of PEG with the bioconjugation moiety NHS (amine-reactive) for immobilization on a variety of substrates, as well as a FITC dye, to enable detection of the PEGylated species *in vitro* or *ex vivo*. We observed that pipetting an RGDS peptide solution over the PEG-FITC-functionalized glass substrate, followed by photobleaching of the dye groups, resulted in site-specific immobilization of the adhesion peptide, as indicated by fibroblast binding exclusively on regions of irradiation (**Figure 3a**). Therefore, the use of this reagent in the development of biosensor arrays affords the resistance of the coating to nonspecific adsorption of proteins.

Dye photobleaching generally involves the energy transfer from the dye in the excited state to molecular oxygen in the ground state (*15-17*). As a result of photobleaching, singlet molecular oxygen is produced, leaving the fluorophore with an unpaired electron. While the process of visible light coupling of dye-conjugated species has not been completely elucidated, it is possible that the unpaired electron on the dye serves as a binding site to an electron-rich substrate. Our data provide further evidence that the photobleached fluorophore as the coupling moiety. When including 1 mg/mL sodium fluorescein (NaFl) as a free dye in the initial mAb coupling solution, we observed a decrease in fluorescence signal from the virus-associated Cy5 secondary antibody, indicating that the coupling technique was associated with fluorophore photobleaching (**Figure 2b**). In previous work, oxygen depletion in the coupling medium was associated with significantly-lower photoattachment efficiency (*1*), which is consistent with our report that photobleaching chemistry is essential for the coupling reaction. Provided that photobleaching events drive the coupling of biomolecules onto the surfaces tested in this work, it is important to take necessary precautions when carrying out individual reactions. Samples were only exposed to ambient lab light for durations < 5 min., to minimize premature photobleaching due to the photolability of fluorescein.

This work expands upon previous approaches to achieve photopatterning of biomolecules, through adapting a confocal microscope to perform automated patterning of microscale regions, and by expanding the scope of surfaces which are candidate substrates for this technique. Future work will focus on the controlled orientation/deposition of cells on adhesion peptide-patterned surfaces. Such a feature would be useful in the development of arrays which incorporate cells as biosensors, or in the synthesis of 3-D tissue constructs, in which hierarchical organization of cells and proteins elicit specific cell functions (*18*). Our technique features the microscale resolution necessary to construct such devices, and nanoscale resolution is potentially achievable with this technique, when used in conjunction with techniques to overcome diffraction barriers, such as stimulated emission depletion fluorescence microscopy (STED) (*19, 20*). While fluorescein was used as the coupling moiety in this work, it has been demonstrated that photottachment strategies can be extended toward the patterning of multiple dye-labeled species, such as Alexa Fluor-labeled proteins (*1*).

Conclusion

Our studies have extended the utility of visible light photoattachment chemistry in creating biomolecular and/or cellular arrays in well-defined microscale regions on diverse substrates. The method is rapid and can be easily controlled on a spatial and temporal scale. Furthermore, protein activity is retained, and the high-efficiency conjugation of proteins using light patterning may facilitate the development of high-sensitivity screening platforms. Additionally, we have shown that a photoreactive substrate can be the mediator for photocoupling, eliminating the need for bioconjugation of species prior to patterning. In forthcoming applications which utilize cells as biosensors, this technique may be useful for controlling cell orientation and spreading. This rapid, flexible technique is readily accessible and can be implemented in a number of biomedical applications.

Acknowledgements

This work was supported in part by the National Institutes of Health (EB003516 (FRH), T32EY07135 (Jeff Schall, PI) (AJ)) and the Vanderbilt University Discovery Grant program. Confocal microscope-assisted patterning experiments were performed in part through the use of the VUMC Cell Imaging Shared Resource. We thank Ray Mernaugh for helpful discussions.

References

(1) Holden, M. A., and Cremer, P. S. (2003) Light activated patterning of dye-labeled molecules on surfaces. *J Am Chem Soc 125*, 8074-5.

(2) Sumerel, J., Lewis, J., Doraiswamy, A., Deravi, L. F., Sewell, S. L., Gerdon, A. E., Wright, D. W., and Narayan, R. J. (2006) Piezoelectric ink jet processing of materials for medical and biological applications. *Biotechnol J 1*, 976-87.

(3) Stevens, M. M., and George, J. H. (2005) Exploring and engineering the cell surface interface. *Science 310*, 1135-8.

(4) Holden, M. A., Jung, S. Y., and Cremer, P. S. (2004) Patterning enzymes inside microfluidic channels via photoattachment chemistry. *Anal Chem 76*, 1838-43.

(5) Blawas, A. S., and Reichert, W. M. (1998) Protein patterning. *Biomaterials 19*, 595-609.

(6) Clemence, J. F., Ranieri, J. P., Aebischer, P., and Sigrist, H. (1995) Photoimmobilization of a bioactive laminin fragment and pattern-guided selective neuronal cell attachment. *Bioconjug Chem 6*, 411-7.

(7) Balasubramanian, A., Bhuva, B., Mernaugh, R., and Haselton, F. R. (2005) Si-based sensor for virus detection. *Ieee Sensors Journal 5*, 340-344.

(8) Stone, G. P., Lin, K. S., and Haselton, F. R. (2006) Adaptive virus detection using filament-coupled antibodies. *Journal of Biomedical Optics 11*, -.

(9) Stone, G. P., Mernaugh, R., and Haselton, F. R. (2005) Virus detection using filament-coupled antibodies. *Biotechnology and Bioengineering 91*, 699-706.

(10) Stone, G. P., Wetzel, J. D., Russ, P. K., Dermody, T. S., and Haselton, F. R. (2006) Autonomous reovirus strain classification using filament-coupled antibodies. *Annals of Biomedical Engineering 34*, 1778-1785.

(11) DeLong, S. A., Gobin, A. S., and West, J. L. (2005) Covalent immobilization of RGDS on hydrogel surfaces to direct cell alignment and migration. *J Control Release 109*, 139-48.

(12) Wu, Y. X., Masison, D. C., Eisenberg, E., and Greene, L. E. (2006) Application of photobleaching for measuring diffusion of prion proteins in cytosol of yeast cells. *Methods 39*, 43-49.

(13) Hermanson, G. T. (1996) *Bioconjugate techniques*, Academic Press, San Diego.

(14) Tessmar, J. K., and Gopferich, A. M. (2007) Customized PEG-derived copolymers for tissue-engineering applications. *Macromol Biosci 7*, 23-39.

(15) Gaigalas, A. K., Wang, L., Cole, K. D., and Humphries, E. (2004) Photodegradation of fluorescein in solutions containing n-propyl gallate. *Journal of Physical Chemistry A 108*, 4378-4384.

(16) Song, L., Hennink, E. J., Young, I. T., and Tanke, H. J. (1995) Photobleaching kinetics of fluorescein in quantitative fluorescence microscopy. *Biophys J 68*, 2588-600.

(17) Song, L., Varma, C. A., Verhoeven, J. W., and Tanke, H. J. (1996) Influence of the triplet excited state on the photobleaching kinetics of fluorescein in microscopy. *Biophys J 70*, 2959-68.

(18) Albrecht, D. R., Underhill, G. H., Mendelson, A., and Bhatia, S. N. (2007) Multiphase electropatterning of cells and biomaterials. *Lab Chip 7*, 702-9.

(19) Willig, K. I., Harke, B., Medda, R., and Hell, S. W. (2007) STED microscopy with continuous wave beams. *Nat Methods*.

(20) Willig, K. I., Kellner, R. R., Medda, R., Hein, B., Jakobs, S., and Hell, S. W. (2006) Nanoscale resolution in GFP-based microscopy. *Nat Methods 3*, 721-3.